MICROWAVE POWER IMAGING FOR ULTRA-WIDE BAND EARLY BREAST CANCER DETECTION

by

Wenyi Shao

A dissertation submitted to the faculty of
The University of North Carolina at Charlotte
in partial fulfillment of the requirements
for the degree of Doctor of Philosophy in
Electrical Engineering

Charlotte

2012

Approved by:

Dr. Ryan S. Adams

Dr. Thomas Weldon

Dr. David Binkley

Dr. Greg Gbur

ABSTRACT

WENYI SHAO. Microwave power imaging for ultra-wide band for
early breast cancer detection. (Under the direction of DR. RYAN S. ADAMS)

Due to the critical need for complementary or/and alternative modalities to current X-ray mammography for early-stage breast cancer detection, a 3D active microwave imaging system has been developed. This thesis presents a detailed method for rapid, high contrast microwave imaging for the purpose of breast survey. In the proposed imaging system, several transmitters polarized in different directions take turns sending out a low-power UWB pulse into the breast; backscattered signals are recorded by a synthetic aperture antenna array. These backscattered signals are passed through a beamformer, which spatially focuses the waveforms to image backscattered energy as a function of location in the breast. A simple Delay-and-Sum algorithm is applied to test the proposed multistatic multi-polarized detection scheme. The obtained 2-D and 3-D numerical results have demonstrated the feasibility and superiority of detecting small malignant breast tumors using our antenna strategy. An improved algorithm of microwave power imaging for detecting small breast tumors within an MRI-derived phantom is also introduced. Our imaging results demonstrate that a high-quality image can be reached without solving the inverse problem.

To set up an experimental system for future clinical investigation, we developed two Vivaldi antennas, which have a notable broad band property, good radiation pattern, and a suitable size for breast cancer detection. Finally, an antenna array which consists of eight proposed Vivaldi antennas is introduced. By conveniently moving up/down and rotating this antenna array, it can be used for the multistatic breast cancer imaging and qualified for our multi-polarized scan mode.

ACKNOWLEDGMENTS

It was quite a journey to purse the Ph. D., and I have too many people to thank. Not exaggerating, I would not have been able to complete this journey without their support over the past several years.

I must first express my gratitude towards my advisors, Professor Ryan S. Adams. He not only helped me keep growing technically and professionally, but his leadership, vision, and strategic thinking also set an example I hope to match someday.

I wish to thank those faculties and technical staff at UNCC for their consulting and assistance in technical areas: Thomas Weldon, David Binkley, Greg Gbur, and Pat Winter.

I would like to thank the graduate students I have worked with on different projects in UNCC Woodward Hall 143: Aaron Hatley, Tsz Kim Lai, and Joshua Shehan. They each helped make my time in the Ph.D. program more fun and interesting. I look forward to future collaboration with any of them.

Last but not least, millions of thanks to my family: my wife and my parents, who have been supporting every decision I made over the years.

TABLE OF CONTENTS

LIST OF TABLES

LIST OF FIGURES

CHAPTER 1: INTRODUCTION

1.1 Background and motivation

Breast cancer is the most common form of cancer among women. In 2005, an estimated 211,240 new cases of invasive breast cancer were diagnosed among women in the U.S., as well as an estimated 58,490 additional cases of in situ breast cancer [1]. In 2007, the estimated number of new breast cancer is markedly lower than the estimate for 2005 due to the use of new, more accurate estimation methods. However, thereafter the number has increased year by year. An estimated 230,480 new cases of invasive breast cancer will be diagnosed among women in 2011, as well as an estimated 57,650 additional cases of in situ breast cancer [2]. In addition, appromimately 40,000 women are expected to die from breast cancer each year since 2005. According to a new survey commissioned by the Society for Womens Health Research, breast cancer has been the disease American women fear the most [3].

Naturally, diagnosing breast cancer early can help women receive treatment early, so they have an increased chance of survival. Many techniques have been developed to use for breast cancer detection:

X-ray mammography is currently the leading method for detecting this type of cancer. Unfortunately, this method is fraught with problems such as high false negative rates [4] and high false positive rates [5]. Additionally, the ionizing nature of X-rays poses a considerable risk of causing the very cancer it attempts to detect. Moreover, there are minor problems such as: since X-ray mammography is a 2-D projection imaging technique, breast compression is required to create a uniform volume between the flat-source board and the flat-receiver board. This makes patients feel very uncomfortable.

Magnetic resonance imaging (MRI) is assumed to be the most accurate and ideal imaging approach. It was even believed by some experts that this technique had the potential to distinguish malignant tumor from the glandular tissues, which is much denser than any other healthy breast tissues. However, a recent report shows that MRI is too sensitive to detect early-stage breast cancer, which might lead to unnecessary surgery [6]. Moreover, an MRI scan is generally very expensive. Additionally, there are relatively few MRI centers, especially outside of major cities. These drawbacks make MRI less suitable for routine breast cancer screening.

Ultrasound is used to determine whether a lesion detected on a mammogram is a liquid cyst or a solid tumor, but is not able to provide additional information. Other imaging methods, including thermography and electrical impedance imaging, are not appropriate for early breast detection because of limitations in image quality and diagnosis accuracy. Therefore, a new safe, low-cost, reliable complement to the X-ray mammography with high image contrast and resolution for early breast cancer detection is neccessary. Microwave detection has the potential to satisfy this need.

However, several issues must be solved before microwave imaging is equipped for practical use. For instance, are the methods applied in RADAR imaging or ground penetrating imaging suitable for microwave medical examination? Is the current screening approach and strategy sufficient? Secondly, loss in tissues tends to increase with frequency, so generally the frequency is limited to approximately 10 GHz. This begs the question: how much bandwidth is enough to generate sufficient resolution for breast cancer detection, and what resolution can it reach with less than 10 GHz bandwidth?... This dissertation aims to answer questions like these, and contribute to the microwave medical breast cancer detection community.

1.2 Dielectric properties of breast tissues

The physical basis of microwave imaging for breast cancer detection is the dielectric-property contrast between normal and malignant tissue in the microwave spectrum. This section briefly reviews several published dielectric measurements on breast tissues at microwave-frequencies.

From 1984 to 1994, a few studies have been conducted on the dielectric properties of cancerous and healthy breast tissues at microwave frequencies. For instance, Chaudhary et al. [7] measured the dielectric properties of excised healthy and malignant breast tissue specimens from 3 MHz-3 GHz in 1984. 4 years later, Surowiec et al. [8] published the measurement of dielectric properties of infiltrating breast carcinoma and selected surrounding nonmalignant tissue in the range of 20 kHz-100 MHz. In 1994, Joines et al. [9] measured the dielectric properties of freshly excised tissues from several organs, including breasts, over the frequency range 50-900 MHz. These three studies have consistently shown that the dielectric constant and conductivity for cancerous breast tissue is three or more times greater than that of the host tissue. These studies are summarized in Fig. 1.1. These data suggest a contrast between malignant and healthy breast tissue of approximately 5:1 in dielectric constant and 10:1 in conductivity in the microwave frequency range. Fig. 1.1 also shows that the comparison of permittivity and conductivity between normal and malignant tissue continues over 3 GHz, based on the single-pole Debye equation.

Further extrapolation and results regarding dielectric properties of normal breast tissue and cancerous tissue were presented in 2007 bby Lazebnik and her colleagues [11] [14]. Rather than discuss “healthy“ breast tissue simply as in previous investigations, Lazebnik et al. measured composition of adipose, glandular and fibroconnective tissue at microwave frequency. It was found that both the dielectric constant and conductivity tend to decrease as the adipose content increases, and conversely as the percent glandular and/or fibroconnective tissue increases, both the dielectric constant

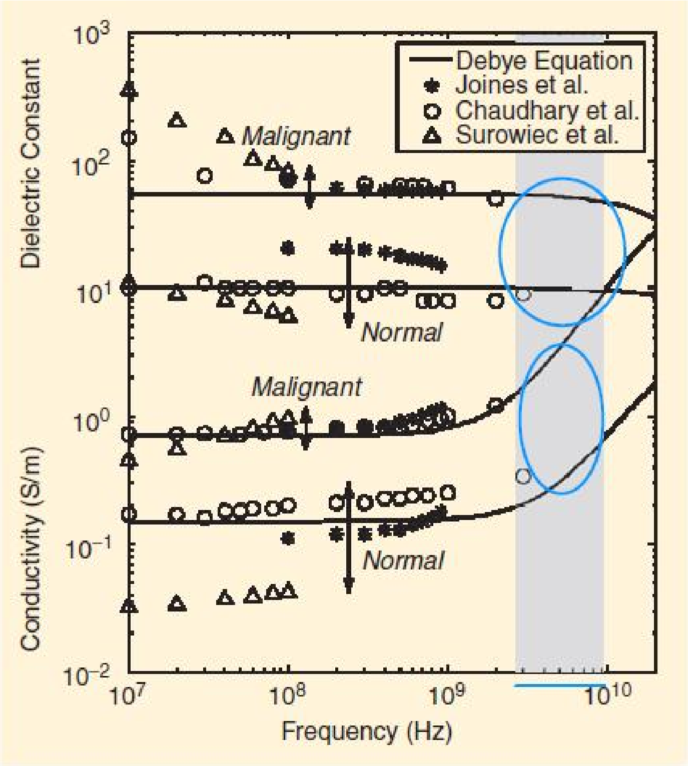

Figure 1.1: Single-pole Debye curve fits of measured baseline dielectric-properties data for normal and malignant breast tissue at radio and microwave frequencies [10].

and conductivity increase [11]. This trend is consistent over a wide frequency band from 0.5 GHz to 20 GHz.

The difference in dielectric properties arise essentially due to the large differences in water content of breast tissues (adipose, glandular and fibroconnective tissue). As the adipose content increases, the water content is reduced, corresponding to the reduced microwave dielectric properties. Fig. 1.2 shows how the dielectric properties change as the tissue composition of normal breast tissue changes. Note that when the adipose content nears zero, (i.e. the tissue is only composed of glandular and fibroconnective tissue), the dielectric constant and conductivity have reached the level of malignant tissue indicated in Fig. 1.1. However, there is still a large dielectric-property contrast between the normal adipose-dominated tissues and the malignant tissues in the breast. Reference [14] implies a nearly 10:1 contrast between malignant

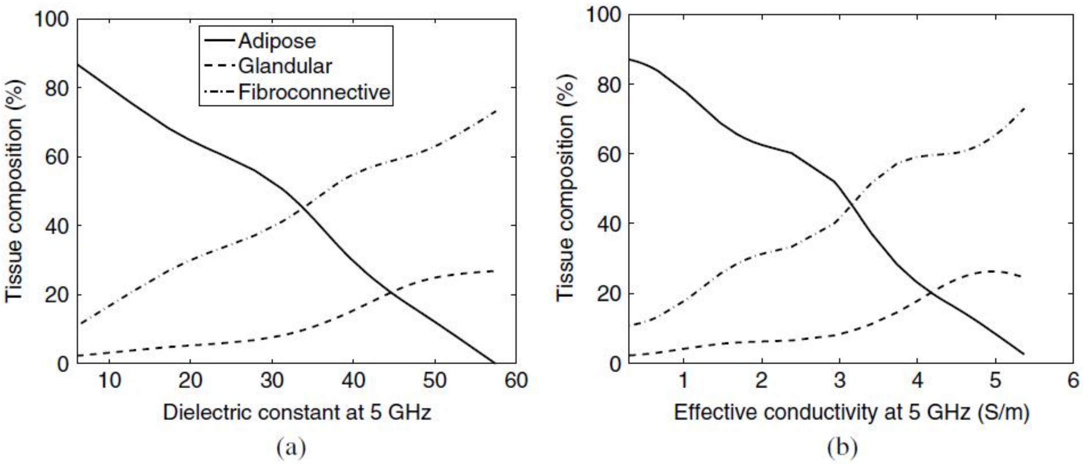

Figure 1.2: Percent tissue type as a function of dielectric constant for (a), and effective conductivity for (b) at 5GHz [14].

tissue and normal tissue that is almost entirely adipose. Although these data were measured at 5 GHz, similar trends were observed at 10 and 15GHz.

Therefore, the performance of "normal" breast tissue may be different due to its composition. Fig. 1.3 gives a better illustration of the change of dielectric properties over a wide frequency band. The curves are color coded based on the adipose content of each sample. In the order of highest to lowest adipose content, the colors are red, purple, blue, cyan and green. This implies that for those with low-adipose content, breasts are not very transparent to microwave. And it might be difficult to recognize malignant tumors in these dense breasts with microwave energy.

To solve this problem, one feasible solution is to classify the breasts according to their density, and treat each class differently. To design numerical breast phantoms with dispersion models that are suitable for computational electromagnetics simulations of micowave imaging and cancer detection, Lazebnik et. al. classified all of their specimens of breast tissue into 3 groups based on the percent adipose tissue in each sample. Group 1 contained all samples with $0-30\%$ adipose tissue (the high-water-content group); group 2 contained all samples with $31-84\%$ adipose tissue,

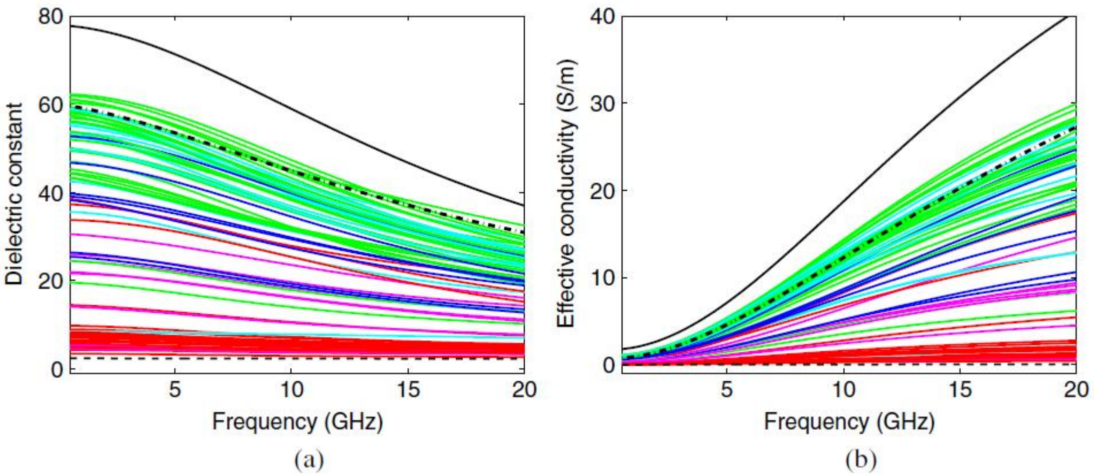

Figure 1.3: 85 normal data specimens for dielectric constant and conductivity over 20 GHz bandwidth. The solid black curve represents the dielectric properties of saline, the dashed black curve represents the dielectric properties of lipids, and the dash-dot black curve represents the dielectric properties of blood [14].

and group 3 contained all samples with $85 - 100\%$ adipose tissue (the low-water-content group). Median dielectric constant and conductivity dispersion curves were obtained for each group and finally concluded in Fig. 1.4. Solid lines in Fig. 1.4 (a) and (b) stand for three adiposed-defined normal tissue groups obtained from cancer surgeries. In the order of highest to lowest dielectric properties are group 1, group 2 and group 3. Dashed lines are median Cole-Cole curves [Appendix] [12] [13] for group 2 for nomal tissue samples obtained from reduction surgeries. Fig. 1.4 (c) and (d) are median Cole-Cole curves for the dielectric constant and conductivity respectively, of cancer samples with minimum malignant tissue content of 30%. Note that the curve of group 1 (from very dense breast) is close to that of the cancerous sample (as mentioned in [14], contrast between malignant and fibroconnective/glandular-dominated tissue is $\leqslant 10\%$). While group 2 and group 3 still have a significant comparative difference from cancerous tissue.

Thus, the dielectric property contrast at microwave frequencies appears to be more significant than the few-percent contrast exploited by X-rays, especially for

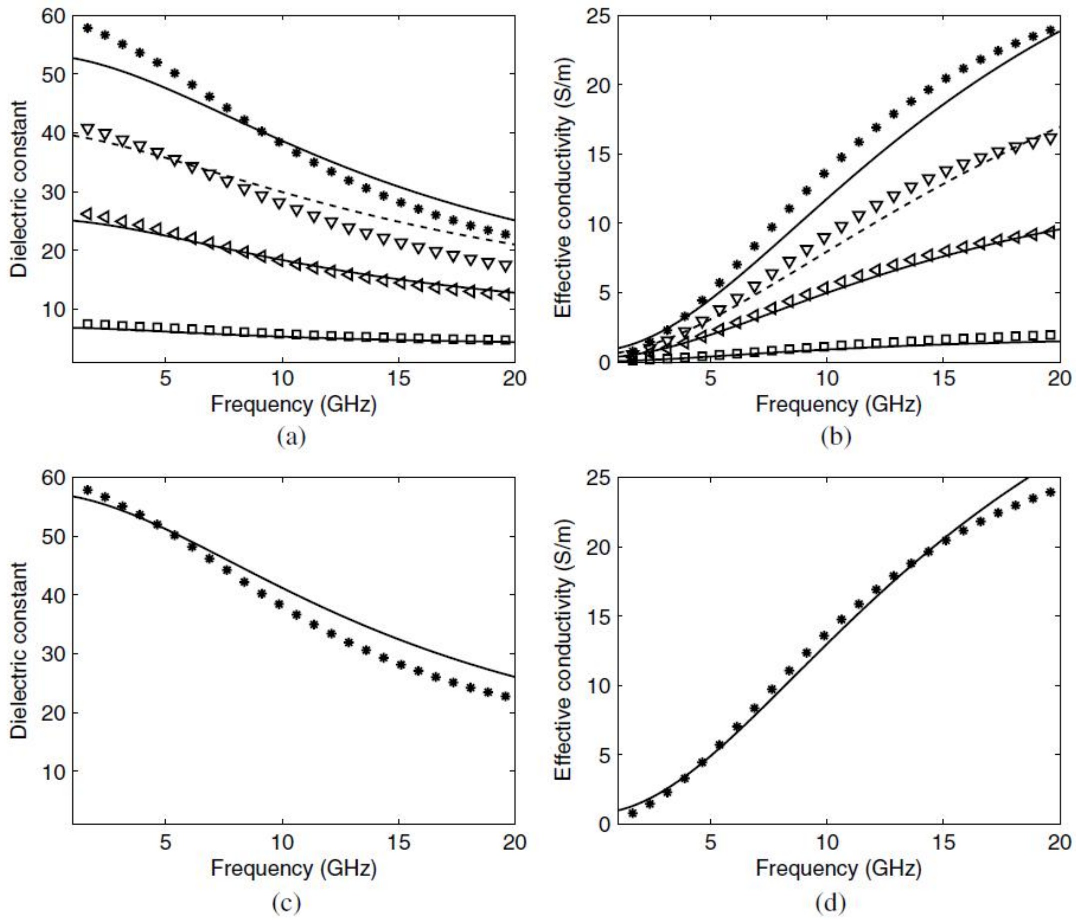

Figure 1.4: Comparison of median Cole-Cole curves for normal and malignant tissue. (a) and (b) are dielectric constant and conductivity, respectively, for 3 groups normal tissue (solid lines). (c) and (d) are dielectric constant and conductivity, respectively, of cancer samples. Symbols stand for measured dielectric properties for tissue-mimicking phantom materials (*, 10% oil; ▽, 30% oil; ◁, 50% oil; □, 80% oil) [15].

breasts that are not very dense (like group 2 and group 3 in Lazebnik's experiment). Actually, when assisted with contrast agents, microwave detection is even able to provide a good image for very dense breasts, in which the contrast agents modify the dieletric properties of malignant tissue to increase the dielectric contrast with fibroglandular tissue [16] [17].

1.3 Active microwave imaging for breast cancer detection

To date, two main types of active microwave breast imaging techniques have been proposed: hybrid microwave-induced acoustic imaging, and radar-based microwave imaging (non-hybrid). In the hybrid mode [19]− [25], microwave signals are transmitted into the breast to heat the tumor - due to the difference of water content, a tumor absorbs more heat than normal breast tissues - and ularasound transducers are used to detect pressure waves generated by the heated tumor.

In the non-hybrid method, the breast is first illuminated by a microwave signal, and the scattered microwave signals are processed to form an image of the cancerous region. Due to the difference in dielectric properties inroduced in Section 1.2, an inverse scattering method that constructs images by recovering the permittivity or conductivity profile of the breast is an intuitive approach to detect cancerous growth. Examples of such methods are diffraction tomographic (DT) algorithm [26], Born approximation (BA) [27], Born iterative method (BIM) [28] and distorted BIM (DBIM) [29]. These methods were originally developed for ground penetrating RADAR (GPR), but some of these, and other similar inverse methods, have been effectively applied in the area of breast cancer medical imaging [30]− [35]. However, these methods are generally time-consuming for processing 3-D images, especially when a relatively large number of iterations are involved to obtain an accurate image.

In 2001 and thereafter, Hagness et al proposed a simple, rapid but effective approach for the microwave detection of breast cancer [10] [36] [37]. This approach only focuses on reflections from scatterers but avoids estimating the dielectric properties of the entire area. The essence of this approach is Delay-And-Sum (DAS). As the illuminating signal is an ultra-wideband pulse, this translates to simply time shifting and summing signals. Fig. 1.5(a) shows the cylindrical model Hagness et al used for studying the DAS method. A cylinder, covered with a thin skin layer, was assummed

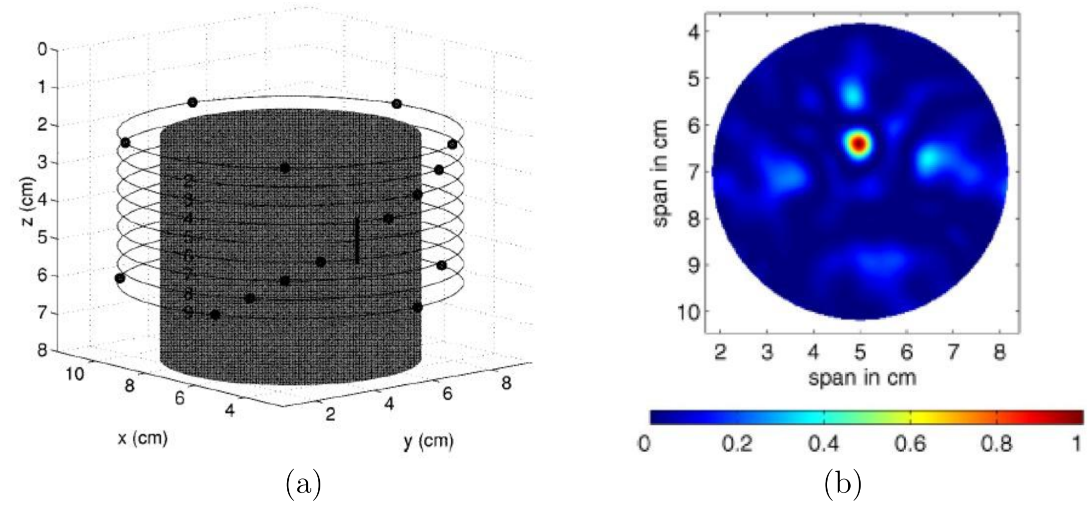

(a) (b)

Figure 1.5: (a) The cylindrical model and the monostatic antenna system to detect a buried malignant tumor; (b) the reconstructed image for (a) in the x-y plane where the tumor exists [37].

to contain healthy breast tissue ($\epsilon_r = 9, \sigma = 0.4S/m$, random variation up to ±10%) and a small malignant tumor ($\epsilon_r = 50, \sigma = 4S/m$). Antennas are settled in 9 rows and each acts as a transmitter and a receiver. Fig. 1.5(b) shows the reconstructed image in the x-y cross-plane in which the tumor exists. Although the breast model in [37] looks very simple today, it illustrated a new way in which microwave medical imaging can be accomplished easiliy, rapidly and efficiently. A more developed DAS method – improved-DAS (IDAS) [38], is an extension of DAS. It uses an additional weight factor that essentially represents the preprocessing and coherent radar operation, calculated at each focal point to improve image quality. The Delay-Multipy-and-Sum (DMAS) is another appoach in the DAS family, in which the time-shifted signals are multiplied in pair before summing [39]. DAS and its follow-up algorithms have shown to be very efficient approaches with acceptable image contrast and resolution.

Furthermore, many other beamforming approaches have been presented to localize the breast tumor. Typical examples are space-time beamforming [40]– [42], robust capon beamforming (RCB) [43], FDTD-based time reversal (FBTR) [44]– [46], generalized likelihood ratio test [47], adaptive [48] and multistatic adaptive microwave imaging (MAMI) [49] [50]. These methods have contributed to microwave breast cancer diagnosis research, and proved that the active microwave method is an effective complement to the current techniques for breast cancer detection.

To apply the approaches described above, researchers have designed a variety of antennas to excite and receive UWB probing signals. The trend of UWB antennas is to make them small, and able be moved/rotated conveniently throughout the scan. A review of UWB antennas for medical applications is made in Chapter 5.

1.4 Objects and outline

This dissertation proposes an improved scheme for UWB microwave imaging for small breast tumor detection. The primary goals of this research include:

- characterization of UWB signals propagating in the breast tissue and scattering from cancerous tissue employed by the finite-difference-time-domain (FDTD) method;

- development and evaluation of imaging algorithms for detecting early (small) breast tumors;

- design and measurement of an UWB antenna and antenna array;

- some conclusions and suggestions for the clinical experiment system setup.

In this dissertation, a multistatic antenna system is employed to detect a small tumor with diameter less than 1 cm in a simple breast model (Chapter 3) and an MRI-derived breast phantom (Chapter 4), respectively. The transmitter sends out a short-pulse signal into the breast and the backscatters are recorded by several receivers. The backscattered signals are then processed similar to a beamformer, to image the backscattered energy as a function of the locations in the breast. Chapter 2 introduces the behavior of programmed FDTD which simulates the process of detecting signal excitation, propagation, and backscattered signal collection. In Chapter 3, the DAS approach is applied to image a simple breast model through the data extracted from the FDTD simulation of Charpter 2. Chapter 4 proposes a new algorithm that is similar to DAS. Tested by imaging an MRI-derived breast phantom, this new algorithm is able to produce a better-quality image than any previous DAS-family approach, but keeps the advantage of DAS-family's efficiency. Chapter 5 presents a new UWB antenna and an antenna array for the breast cancer detection measurement. And the final conclusion is made in Chapter 6.

CHAPTER 2: FDTD-BASED SIMULATION OF A BREAST MODEL

The finite-difference time-domain (FDTD) formulation of electromagnetic simulation is a convenient tool for solving scattering problems. This method, first introduced by Yee in 1966 [51] and later developed by Taflove and others [52]- [55], is a direct solution of Maxwell's time-dependent curl equations. This scheme treats the irradiation of the scatterer as an initial value problem. In this chapter, discussion of the FDTD method will cover:

* finite difference equations;

* absorbing boundary conditions and stability;

* 2-D field FDTD example;

* 3-D field FDTD example.

Note that the contents discussed in this chapter is related to, and based on the topic of breast tissue/model applied in this dissertation .

2.1 Finite Difference Equations

In an isotropic medium, Maxwell's equations can be written

$$\bigtriangledown \times \mathbf{E} = -\mu \frac{\partial \mathbf{H}}{\partial t} \tag{2.1}$$

$$\bigtriangledown \times \mathbf{H} = \sigma \mathbf{E} + \epsilon \frac{\partial \mathbf{E}}{\partial t} \tag{2.2}$$

The vector Eqn (2.1) and (2.2) represent a six scalar equation series, which can be expressed in Cartesian coordinates as:

$$\frac{\partial H_x}{\partial t} = \frac{1}{\mu}\left(\frac{\partial E_y}{\partial z} - \frac{\partial E_z}{\partial y}\right) \tag{2.3}$$

$$\frac{\partial H_y}{\partial t} = \frac{1}{\mu}\left(\frac{\partial E_z}{\partial x} - \frac{\partial E_x}{\partial z}\right) \tag{2.4}$$

$$\frac{\partial H_z}{\partial t} = \frac{1}{\mu}\left(\frac{\partial E_x}{\partial y} - \frac{\partial E_y}{\partial x}\right) \tag{2.5}$$

$$\frac{\partial E_x}{\partial t} = \frac{1}{\epsilon}\left(\frac{\partial H_z}{\partial y} - \frac{\partial H_y}{\partial z} - \sigma E_x\right) \tag{2.6}$$

$$\frac{\partial E_y}{\partial t} = \frac{1}{\epsilon}\left(\frac{\partial H_x}{\partial z} - \frac{\partial H_z}{\partial x} - \sigma E_y\right) \tag{2.7}$$

$$\frac{\partial E_z}{\partial t} = \frac{1}{\epsilon}\left(\frac{\partial H_y}{\partial x} - \frac{\partial H_x}{\partial y} - \sigma E_z\right) \tag{2.8}$$

Following Yee's approach, these differential equations can be approximated with difference equations if one positions the components of **E** and **H** throughout a unit cell of the lattice as shown in Fig. 2.1.

We take Eqn. (2.6) as an example and write its equivalent difference equation:

$$\begin{aligned}
&\epsilon\frac{E_x^{n+1}(i+\frac{1}{2},j,k) - E_x^{n}(i+\frac{1}{2},j,k)}{\Delta t} \\
=&\frac{H_z^{n+1/2}(i+\frac{1}{2},j+\frac{1}{2},k) - H_z^{n+1/2}(i+\frac{1}{2},j-\frac{1}{2},k)}{\Delta y} \\
&- \frac{H_y^{n+1/2}(i+\frac{1}{2},j,k+\frac{1}{2}) - H_y^{n+1/2}(i+\frac{1}{2},j,k-\frac{1}{2})}{\Delta z} - \sigma E_x^{n+1/2}(i+\frac{1}{2},j,k))
\end{aligned} \tag{2.9}$$

where, $n+1/2$ represents the time instant $t = (n+1/2)\Delta t$. If the approximation

$$E_x^{n+1/2}(i+\frac{1}{2},j,k) = \frac{E_x^{n+1}(i+\frac{1}{2},j,k) + E_x^{n}(i+\frac{1}{2},j,k)}{2} \tag{2.10}$$

is made, Eqn. (2.9) can be rearranged as

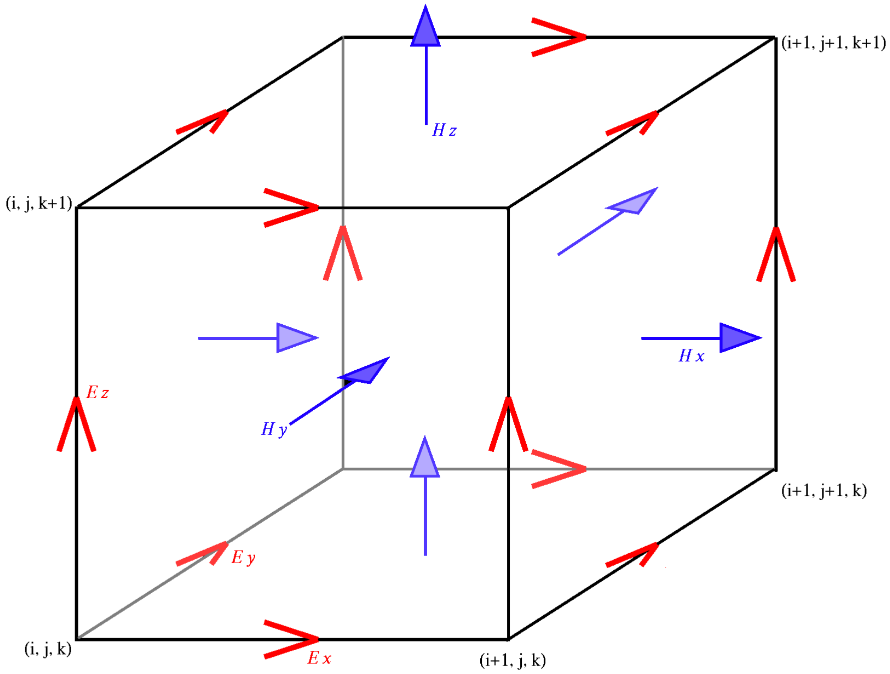

Figure 2.1: Yee cell in FDTD. [51]

$$
\begin{aligned}
&E_x^{n+1}(i+\frac{1}{2},j,k)\\
=&CA(m)\cdot E_x^{n}(i+\frac{1}{2},j,k)\\
&+CB(m)\cdot\left[\frac{H_x^{n+1/2}(i+\frac{1}{2},j+\frac{1}{2},k)-H_z^{n+1/2}(i+\frac{1}{2},j-\frac{1}{2},k)}{\Delta y}\right.\\
&\left.-\frac{H_y^{n+1/2}(i+\frac{1}{2},j,k+\frac{1}{2})-H_y^{n+1/2}(i+\frac{1}{2},j,k-\frac{1}{2})}{\Delta z}\right]
\end{aligned}
\tag{2.11}
$$

where

$$
CA(m)=\frac{\frac{\epsilon(m)}{\Delta t}-\frac{\sigma(m)}{2}}{\frac{\epsilon(m)}{\Delta t}+\frac{\sigma(m)}{2}}=\frac{1-\frac{\sigma(m)\Delta t}{2\epsilon(m)}}{1+\frac{\sigma(m)\Delta t}{2\epsilon(m)}}
\tag{2.12}
$$

$$
CB(m)=\frac{1}{\frac{\epsilon(m)}{\Delta t}+\frac{\sigma(m)}{2}}=\frac{\frac{\Delta t}{\epsilon(m)}}{1+\frac{\sigma(m)\Delta t}{2\epsilon(m)}}
\tag{2.13}
$$

where $m=(i+1/2,j+1/2,k+1/2)$, i.e. the center of the Yee cell. Similarly, the difference equations of Eqn. (2.7) and Eqn. (2.8) may be written as

$$\begin{aligned}
&E_y^{n+1}(i,j+\frac{1}{2},k)\\
=&CA(m)\cdot E_y^{n}(i,j+\frac{1}{2},k)\\
&+CB(m)\cdot\left[\frac{H_x^{n+1/2}(i,j+\frac{1}{2},k+\frac{1}{2})-H_x^{n+1/2}(i,j+\frac{1}{2},k-\frac{1}{2})}{\Delta z}\right.\\
&\left.-\frac{H_z^{n+1/2}(i+\frac{1}{2},j+\frac{1}{2},k)-H_z^{n+1/2}(i-\frac{1}{2},j+\frac{1}{2},k)}{\Delta x}\right]
\end{aligned} \tag{2.14}$$

and

$$\begin{aligned}
&E_z^{n+1}(i,j,k+\frac{1}{2})\\
=&CA(m)\cdot E_z^{n}(i,j,k+\frac{1}{2})\\
&+CB(m)\cdot\left[\frac{H_y^{n+1/2}(i+\frac{1}{2},j,k+\frac{1}{2})-H_y^{n+1/2}(i-\frac{1}{2},j,k+\frac{1}{2})}{\Delta x}\right.\\
&\left.-\frac{H_x^{n+1/2}(i,j+\frac{1}{2},k+\frac{1}{2})-H_x^{n+1/2}(i,j-\frac{1}{2},k+\frac{1}{2})}{\Delta y}\right]
\end{aligned} \tag{2.15}$$

Eqn.(2.11), (2.14), and (2.15) are computations of electric field in FDTD over time and space. Similarly, at any instant of $t = n\Delta t$, we can obtain the equations for H field computaion:

$$\begin{aligned}
&H_x^{n+1/2}(i,j+\frac{1}{2},k+\frac{1}{2})\\
=&CP(m)\cdot H_x^{n-1/2}(i,j+\frac{1}{2},k+\frac{1}{2})\\
&-CQ(m)\cdot\left[\frac{E_z^{n}(i,j+1,k+\frac{1}{2})-E_z^{n}(i,j,k+\frac{1}{2})}{\Delta y}\right.\\
&\left.-\frac{E_y^{n}(i,j+\frac{1}{2},k+1)-E_y^{n}(i,j+\frac{1}{2},k)}{\Delta z}\right]
\end{aligned} \tag{2.16}$$

$$\begin{aligned}&H_y^{n+1/2}(i+\frac{1}{2},j,k+\frac{1}{2})\\=&CP(m)\cdot H_y^{n-1/2}(i+\frac{1}{2},j,k+\frac{1}{2})\\&-CQ(m)\cdot\Bigg[\frac{E_x^n(i+\frac{1}{2},j,k+1)-E_x^n(i+\frac{1}{2},j,k)}{\Delta z}\\&-\frac{E_z^n(i+1,j,k+\frac{1}{2})-E_z^n(i,j,k+\frac{1}{2})}{\Delta x}\Bigg]\end{aligned}\tag{2.17}$$

$$\begin{aligned}&H_z^{n+1/2}(i+\frac{1}{2},j+\frac{1}{2},k)\\=&CP(m)\cdot H_z^{n-1/2}(i+\frac{1}{2},j+\frac{1}{2},k)\\&-CQ(m)\cdot\Bigg[\frac{E_y^n(i+1,j+\frac{1}{2},k)-E_y^n(i,j+\frac{1}{2},k)}{\Delta x}\\&-\frac{E_x^n(i+\frac{1}{2},j+1,k)-E_x^n(i+\frac{1}{2},j,k)}{\Delta y}\Bigg]\end{aligned}\tag{2.18}$$

where

$$CP(m)=\frac{\frac{\mu}{\Delta t}-\frac{\sigma_m(m)}{2}}{\frac{\mu(m)}{\Delta t}+\frac{\sigma_m(m)}{2}}\tag{2.19}$$

$$CQ(m)=\frac{1}{\frac{\mu(m)}{\Delta t}+\frac{\sigma_m(m)}{2}}\tag{2.20}$$

In our simulation, we assume that the magnetic conductivity, $\sigma_m = 0$ everywhere in the breast. And for high frequency, $\mu = \mu_0$, hence $CP(m)$ and $CQ(m)$ are simplified to

$$CP(m) = 1\tag{2.21}$$

$$CQ(m)=\frac{\Delta t}{\mu_0}\tag{2.22}$$

For convenience, we will use identical grid spacing in the x, y, and z directions, i.e. $\Delta x = \Delta y = \Delta z = \delta$. Hence, Eqn. (2.11) and Eqn.(2.14) − Eqn.(2.18) can be arranged:

$$\begin{aligned} E_x^{n+1}\left(i+\frac{1}{2},j,k\right) =& CA(m)\cdot E_x^{n}\left(i+\frac{1}{2},j,k\right) \\ &+ CB'(m)\left[H_z^{n+1/2}\left(i+\frac{1}{2},j+\frac{1}{2},k\right) - H_z^{n+1/2}\left(i+\frac{1}{2},j-\frac{1}{2},k\right)\right. \\ &\left. -H_y^{n+1/2}\left(i+\frac{1}{2},j,k+\frac{1}{2}\right) + H_y^{n+1/2}\left(i+\frac{1}{2},j,k-\frac{1}{2}\right)\right] \end{aligned} \tag{2.23}$$

$$\begin{aligned} E_y^{n+1}\left(i,j+\frac{1}{2},k\right) =& CA(m)\cdot E_y^{n}\left(i,j+\frac{1}{2},k\right) \\ &+ CB'(m)\left[H_x^{n+1/2}\left(i,j+\frac{1}{2},k+\frac{1}{2}\right) - H_x^{n+1/2}\left(i,j+\frac{1}{2},k-\frac{1}{2}\right)\right. \\ &\left. -H_z^{n+1/2}\left(i+\frac{1}{2},j+\frac{1}{2},k\right) + H_z^{n+1/2}\left(i-\frac{1}{2},j+\frac{1}{2},k\right)\right] \end{aligned} \tag{2.24}$$

$$\begin{aligned} E_z^{n+1}\left(i,j,k+\frac{1}{2}\right) =& CA(m)\cdot E_z^{n}\left(i,j,k+\frac{1}{2}\right) \\ &+ CB'(m)\left[H_y^{n+1/2}\left(i+\frac{1}{2},j,k+\frac{1}{2}\right) - H_y^{n+1/2}\left(i-\frac{1}{2},j,k+\frac{1}{2}\right)\right. \\ &\left. -H_x^{n+1/2}\left(i,j+\frac{1}{2},k+\frac{1}{2}\right) + H_x^{n+1/2}\left(i,j-\frac{1}{2},k+\frac{1}{2}\right)\right] \end{aligned} \tag{2.25}$$

$$\begin{aligned} H_x^{n+1/2}\left(i,j+\frac{1}{2},k+\frac{1}{2}\right) =& H_x^{n-1/2}\left(i,j+\frac{1}{2},k+\frac{1}{2}\right) \\ &+ CQ'(m)\cdot\left[E_y^{n}\left(i,j+\frac{1}{2},k+1\right) - E_y^{n}\left(i,j+\frac{1}{2},k\right)\right. \\ &\left. -E_z^{n}\left(i,j+1,k+\frac{1}{2}\right) + E_z^{n}\left(i,j,k+\frac{1}{2}\right)\right] \end{aligned} \tag{2.26}$$

$$\begin{aligned} H_y^{n+1/2}\left(i+\frac{1}{2},j,k+\frac{1}{2}\right) =& H_y^{n-1/2}\left(i+\frac{1}{2},j,k+\frac{1}{2}\right) \\ &+ CQ'(m)\cdot\left[E_z^{n}\left(i+1,j,k+\frac{1}{2}\right) - E_z^{n}\left(i,j,k+\frac{1}{2}\right)\right. \\ &\left. -E_x^{n}\left(i+\frac{1}{2},j,k+1\right) + E_x^{n}\left(i+\frac{1}{2},j,k\right)\right] \end{aligned} \tag{2.27}$$

$$\begin{aligned}H_z^{n+1/2}\left(i+\frac{1}{2},j+\frac{1}{2},k\right)=&H_z^{n-1/2}\left(i+\frac{1}{2},j+\frac{1}{2},k\right)\\&+CQ'(m)\cdot\left[E_x^n\left(i+\frac{1}{2},j+1,k\right)-E_x^n\left(i+\frac{1}{2},j,k\right)\right.\\&\left.-E_y^n\left(i+1,j+\frac{1}{2},k\right)+E_y^n\left(i,j+\frac{1}{2},k\right)\right]\end{aligned}\tag{2.28}$$

where

$$CQ'(m)=\frac{CQ(m)}{\delta}=\frac{\Delta t}{\mu_0\delta}\tag{2.29}$$

Hence, Eqn.(2.23) $-$ (2.28), and Eqn.(2.12), (2.13), and 2.29 are the final difference equations that will be applied in our FDTD simulation.

2.2 Absorbing boundary conditions and stability

An artificial termination is necessary to truncate the solution region electrically close to the radiating/scattering object but effectively simulate the solution to infinity. These termination conditions, known as absorbing boundary conditions (ABCs), are theoretically able to absorb incident and scattered fields. The accuracy of the ABC dictates the accuracy of the simulation. Reference [56] $-$ [65] have listed various types of ABCs, among which, the perfectly matched layer (PML) [60]$-$ [64] is probably the most accurate approach. However, the reason PML is not applied in our simulation is that PML generally consumes too much computation resources, such that a simulation with PML absorbing boundary usually takes an unreasonably long time. Considering the efficiency, we use Liao's ABCs [57] [58], instead.

Liao's absorbing boundary conditions are an efficient tool and have shown to yield excellent results using double-precision arithmetic when the angle of incidence is not too large [66]. We will apply Liao's ABCs in our simulation but before this, an evaluation will be made to understand the accuracy of this boundary condition.

Let $E(t,x_1)$ (electric field, or H if magnetic field) denote the wave incident on the boundary point x_1 at time t. Then, using Liao's boundary condition, we have

$$E(t + \Delta t, x_1) \approx \sum_{j=1}^{N} (-1)^{j+1} C_j^N \mathbf{T}_j \mathbf{E}_j \tag{2.30}$$

where C_j^N is the binomial coefficient and N is the order of the binomial coefficient. The vector $\mathbf{E}_j$ is defined as

$$\mathbf{E_j} = \begin{bmatrix} E_{1,j} \\ E_{2,j} \\ \cdots \\ E_{2j+1,j} \end{bmatrix} \tag{2.31}$$

where

$$\begin{cases} E_{i,j} = E(t_j, x_i) \\ t_j = t - (j-1)\Delta t \\ x_i = x_1 - (i-1)\Delta x \end{cases} \tag{2.32}$$

For 2nd order Liao's ABC, i.e., $N = 2$, we obtain

$$E(t + \Delta t, x_1) \approx 2\mathbf{T_1}\mathbf{E_1} - \mathbf{T_2}\mathbf{E_2} \tag{2.33}$$

The interpolation vector, $\mathbf{T}_1$ and $\mathbf{T}_2$ are defined as follows:

$$\mathbf{T}_2 = \mathbf{T}_1 \cdot \begin{bmatrix} \mathbf{T}_1 & 0 & 0 \\ 0 & \mathbf{T}_1 & 0 \\ 0 & 0 & \mathbf{T}_1 \end{bmatrix} \tag{2.34}$$

and

$$\mathbf{T}_1 = \begin{pmatrix} T_{11} & T_{12} & T_{13} \end{pmatrix} \tag{2.35}$$

where

$$\begin{cases} T_{11} = (2-s)(1-s)/2 \\ T_{12} = s(2-s) \\ T_{13} = s(s-1)/2 \\ s = v\Delta t/\Delta x \end{cases} \tag{2.36}$$

where v is the propagatation speed of the wave. Eqn.(2.33) indicates that if the 2^{nd} order Liao's ABC is applied, we need to record the data of the current-step electric field and the previous-step electric field for the next step computation. $\mathbf{T}_1$ and $\mathbf{T}_2$ are parameters of current-step electric field and previous-step electric field, respectively for the computation, and can be obtained through Eqn. (2.34) − Eqn. (2.36).

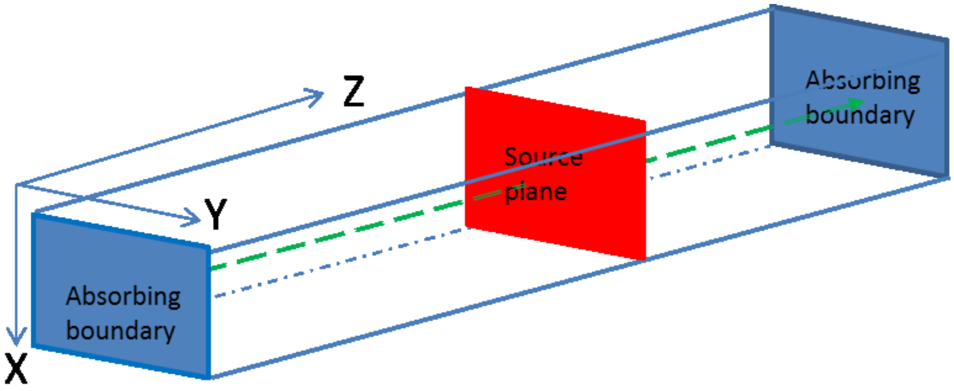

Figure 2.2: A waveguider-like model to test the absorbing boundary.

To evaluate the result of Liao's 2^{nd} order ABC, we set up a long-retangular box that has a length of 500 Yee cells in the z direction and 20×20 cells in the x-y plane, as shown in Fig. 2.2. This box is bounded with perfect electric conductor (PEC) on the upper and lower surfaces, and perfect magnetic conductor (PMC) on the front and back. A plane wave signal, sent from the source plane in the middle of the box, and absorbed by the absorbing boundary at the terminals, is a simple Gaussian pulse. Assuming that the upper limit of the frequency is 10 GHz, this translates to $3cm$-long wavelength in free space, and $1cm$ wavelength in typical breast tissue (relative permitivity =9). Thus, a grid spacing of the Yee cell of $1mm \times 1mm \times 1mm$ is sufficient to provide accuracy. Consider the stability condition [54] [67], the time step is required to satisfy the equation:

$$\Delta t \leq \frac{\delta}{c\sqrt{3}} \approx 1.9 \times 10^{-12} second \tag{2.37}$$

Hence, we select $\Delta t = \frac{5}{3} ps$, i.e., $\frac{5}{3} \times 10^{-12} s$. If this box is filled with air (or vacuum), according to Eqn. (2.36), then we have $s = 0.5$. Fig. 2.3 despicts several instants of propagation in the model, terminated by Liao's 2nd order ABC, using the FDTD method. In Fig. 2.3(a), the Gaussian pulse is generated in the center position of the model; (b) shows the generated pulse starts to move in the +z and -z direction, respectively; (c) shows the pulses continuing to propagate in the model; (d) shows the pulses impinging upon the boundary; (e) indicates that there is a reflection from the boundary, meanwhile, most of the pulse energy has "gone out" of the model through the boundary; (f) shows the reflected wave propagating back, and its amplitude drops to approximately 2×10^{-5} (-94 dB). It is interesting to note that the reflected pulse is distorted, instead of the simple Gaussian pulse originarily generated. Fig. 2.3 demonstrates that the absorption of Liao's 2nd order ABC from normal incidence in air is quite good.

As a second test, assume that the box shown in Fig. 2.2 is filled with a particular medium ($\epsilon_r = 9$, $\sigma = 0$), which has similar dielectric constant to that of typical breast tissue. Using the same δ and Δt as above, we can obtain $s = 0.167$, and corresponding $\mathbf{T}_1$, $\mathbf{T}_2$ through Eqn. (2.34) – Eqn. (2.36). Fig. 2.4 shows the signal propagating in the medium-filled model, using FDTD and Liao's 2^{nd} order ABC. Fig.2.4(a) shows the Gaussian pulse forming; (b) indicates that the pulse has been completely generated and starts propagating toward both two terminals; (c) shows the signal propagating in the medium-filled box; (d) shows the microwave signal is impinging upon the absorbing boundary; in Fig. 2.4(e), the signal vibrates dramatically because of the combination of the Gausian-pulse's tail and the reflected wave; (f) shows the reflected wave heading back. Again, the shape of reflected wave is no longer the original Gaussian pulse but distorted. We do not know why this happens, but its maximum value is reduced to about 2.5×10^{-5} (-92 dB), which is what we expected to see.

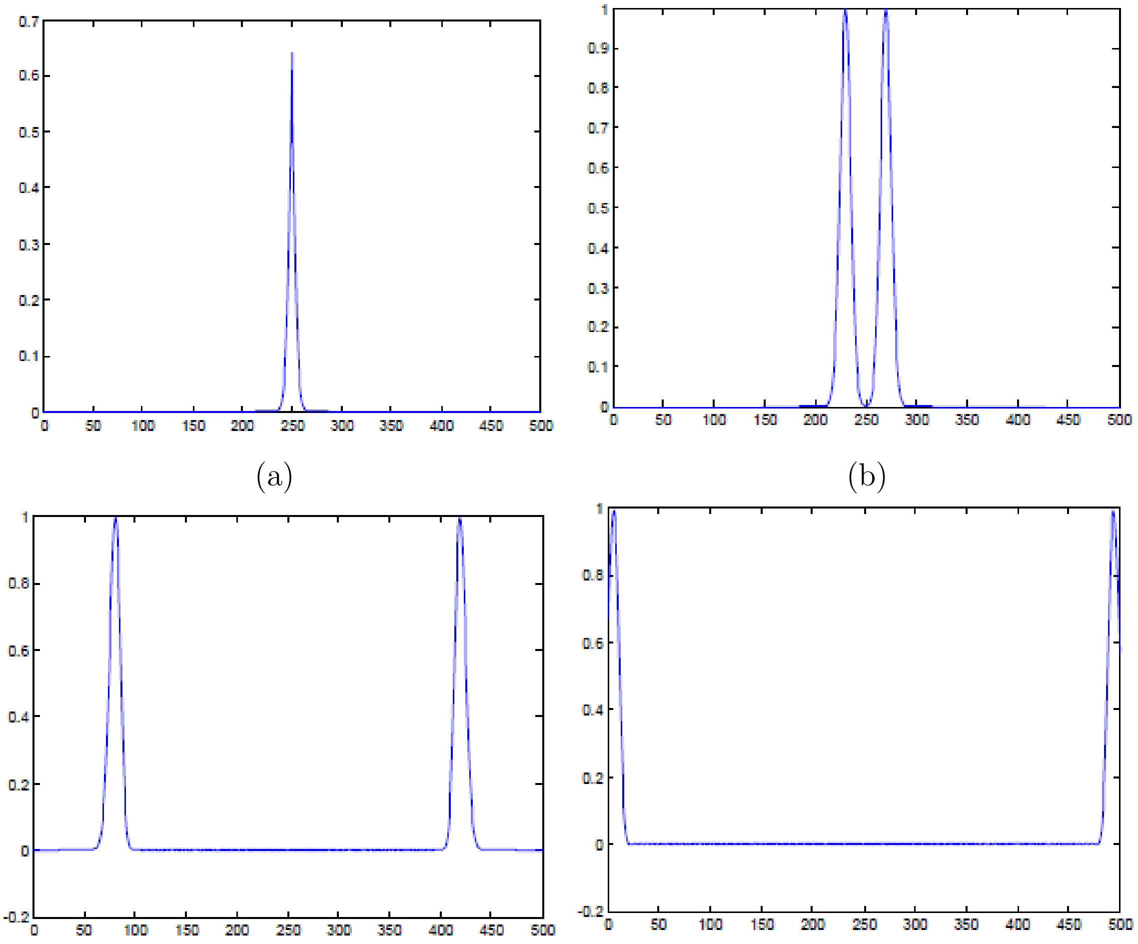

(a) (b)

(c) (d)

Figure 2.3: Wave propagates in the model shown in Fig.2.2. (a) 100th step, (b) 150th step, (c) 400th step, (d) 560th step.

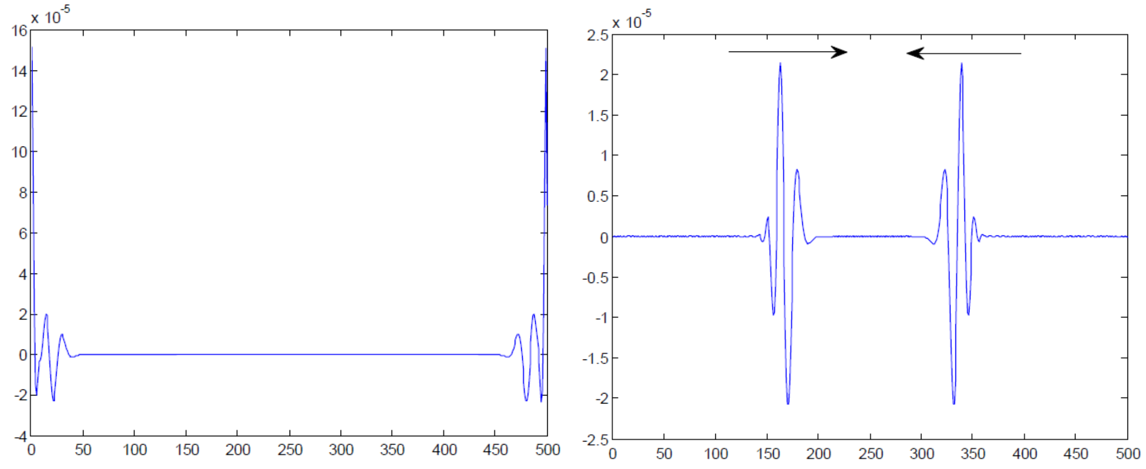

(e) (f)

Figure 2.3: Wave propagates in the model shown in Fig.2.2: (e) 600th, (f) 700th step.

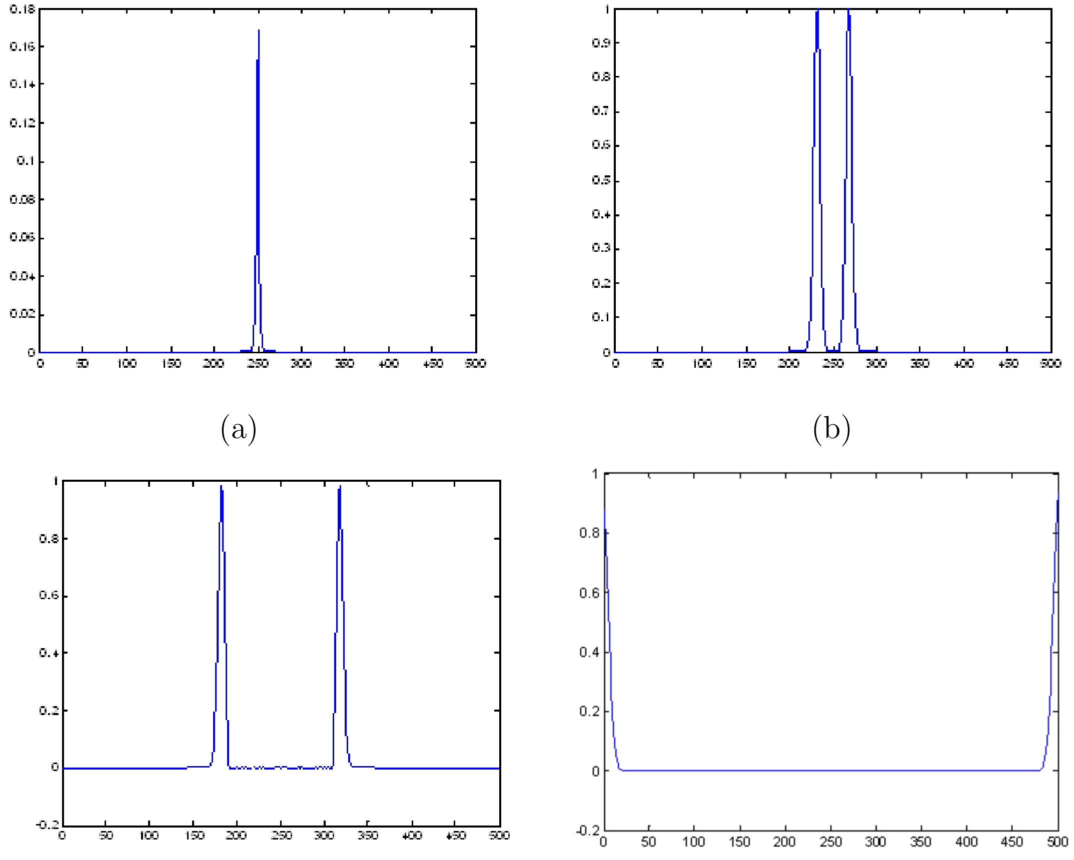

(a) (b)

(c) (d)

Figure 2.4: Wave propagates in the model shown in Fig.2.2 filled with medium. (a) 80th step, (b) 210th step, (c) 480th step, (d) 1400th step.

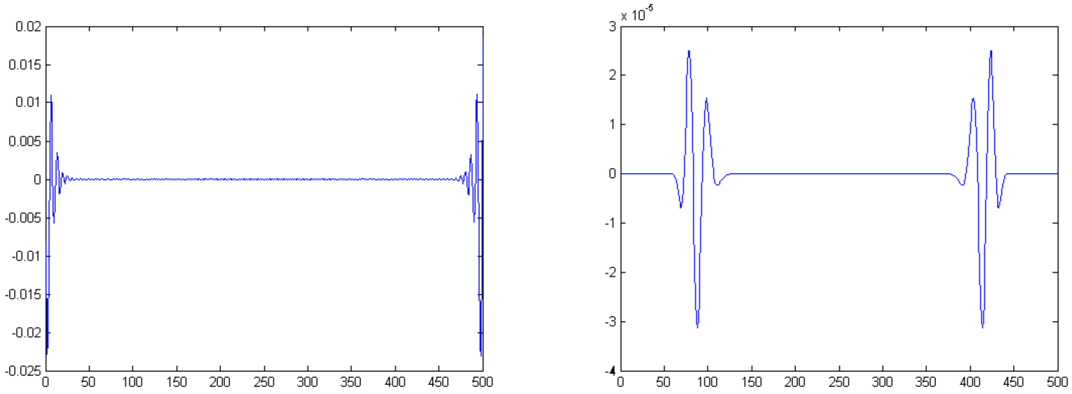

(e) (f)

Figure 2.4: Wave propagates in the model shown in Fig.2.2 filled with medium. (e) 1460th step, (f) 1970th step.

To summrize, we have demonstrated that the 2nd order Liao's ABC is able to absorb most of the energy of the incident wave. Meanwhile, it yields a $-94dB$ reflection in air, and a $-92dB$ reflected wave if in a specific medium with $\epsilon_r = 9$, $\sigma = 0$. This slight reflection is negligible in our FDTD simulation for the breast caner detection investigation.

2.3 2-D FDTD simulation

Our purpose is to simulate microwave signal propagation and scattering in the breast. Before we extend it to 3-D, a 2-D model is introduced in order to easily explain our scheme. In Fig. 2.5, the 2-D space is split into several parts. The skin layer is located from $Y = 75mm$ to $Y = 77mm$, below which is the breast region and above that is the air. The black spot buried in the breast region represents a tumor. The excitation source and the receivers are located in the air, on the surface of the skin. The dielectric parameters for each part is displayed in Table 2.1. Since the dielectric difference of the air and skin is very large, we assume that our excitation and receivers are positioned on the surface of the skin tightly to prevent most of the signal energy from reflecting on the surface of the skin but not enter the breast region.

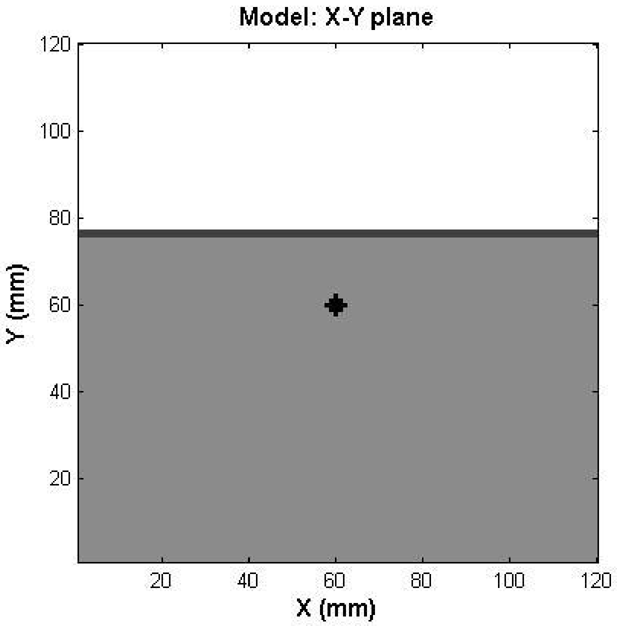

Figure 2.5: 2-D FDTD simulation for a simplified breast model.

The absorbing boundaries have been designed for each region (air, skin, and breast region) that contacts the boundary.

Table 2.1: Dielectric properties for each part in Fig. 2.5

Tissues	Relative Permittivity (F/m)	Conductivity (S/m)
air	1	0
Skin	36	4
Breast Tissue	9	0.4
Tumor	50	4

The TM mode is applied in our 2-D FDTD simulation. Therefore, only H_x, H_y, and E_z are used in the FDTD equations and only 3 difference equations (Eqn. (2.38) – (2.40) are employed in the computation. Note that the absorbing boundaries are H-field boundaries. The excitation signal is a modulated Gaussian pulse, which is shown in the time-domain and frequency domain, respectively, in Fig. 2.6(a) and (b).

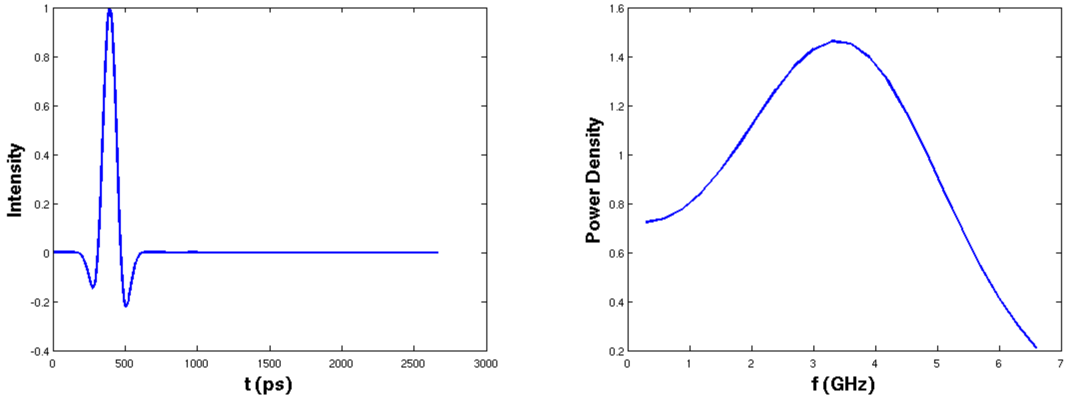

(a) (b)

Figure 2.6: The detecting UWB signal in (a) time domain, and (b) in frequency domain.

$$\begin{aligned}
E_z^{n+1/2}\left(i-\frac{1}{2},j+\frac{1}{2}\right) =&CA(m)\cdot E_z^{n-1/2}\left(i-\frac{1}{2},j+\frac{1}{2}\right)\\
&+CB'(m)\left[H_y^n\left(i,j+\frac{1}{2}\right)-H_y^n\left(i-1,j+\frac{1}{2}\right)\right.\\
&\left.-H_x^n\left(i-\frac{1}{2},j+1\right)+H_x^n\left(i-\frac{1}{2},j\right)\right] \qquad (2.38)\\
H_x^{n+1}\left(i-\frac{1}{2},j+1\right) =&H_x^n\left(i-\frac{1}{2},j+1\right)\\
&+CQ'(m)\cdot\left[E_z^{n+\frac{1}{2}}\left(i-\frac{1}{2},j+\frac{1}{2}\right)-E_z^{n+\frac{1}{2}}\left(i-\frac{1}{2},j+\frac{3}{2}\right)\right]\\
&\qquad (2.39)\\
H_y^{n+1}\left(i,j+\frac{1}{2}\right) =&H_y^n\left(i,j+\frac{1}{2}\right)+CQ'(m)\cdot\left[E_z^{n+\frac{1}{2}}\left(i+\frac{1}{2},j+\frac{1}{2}\right)\right.\\
&\left.-E_z^{n+\frac{1}{2}}\left(i-\frac{1}{2},j+\frac{1}{2}\right)\right] \qquad (2.40)
\end{aligned}$$

The 3dB bandwidth of the signal is approximately 5 GHz, while the peak of the spectrum appears near 3.2 GHz. Assuming that the excitation is positioned at $x = 60mm, y = 77mm$ in Fig. 2.5, and 4 receivers are positioned at $(x = 20mm, y = 77mm), (x = 40mm, y = 77mm), (x = 80mm, y = 77mm)$, and $(x = 100mm, y = 77mm)$ respectively. Fig. 2.7 records the electric field E_z at several time steps.

Fig. 2.7(a) shows the source starts to radiate at step $t = 100\Delta t$. (b) represents the excitation is strengthening. In (c), the excitation has reached its maximum, which is corresponding to the time instant $t = 400ps$ in Fig.2.6(a). (d) and (e) denote that the radiated pulse penetrates through the skin layer and goes deeper into the breast tissue area. Note that the wave speed in air is much faster than in the skin and the breast, therefore, a wavefront in the air has already met the top boundary, when the wavefront in the breast is still propagating toward the tumor. (f) and (g) show that the wave is passing through the tumor. It can be seen that the field in the area close to $x = 60mm$, $y = 60mm$, which is the center of the tumor, is much stronger than elsewhere, resulting from the field response of the tumor. Fig. 2.7(h)-(k) denote that the wave propagates deeper into the breast, and has arrived the left and right boundary in (k). At this point, it is worth noting that the scattered field of the tumor is combined with the incident field, and cannot be discerned in these figures, since the scattered field is much weaker than the incident field. In Fig. 2.7(l)-(n), the process of wave absorption by the bottom absorbing boundary is depicted.

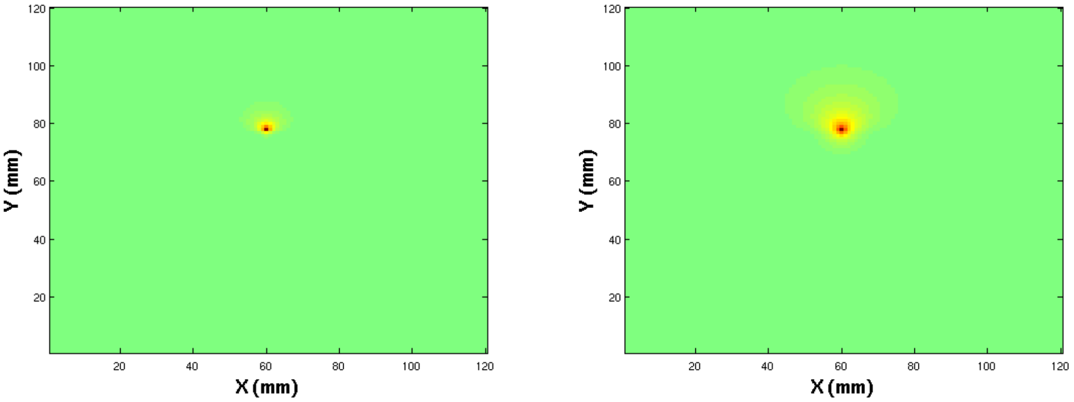

(a) 100th step

(b) 180th step

Figure 2.7: Electric Field evolves within the computation region over time.

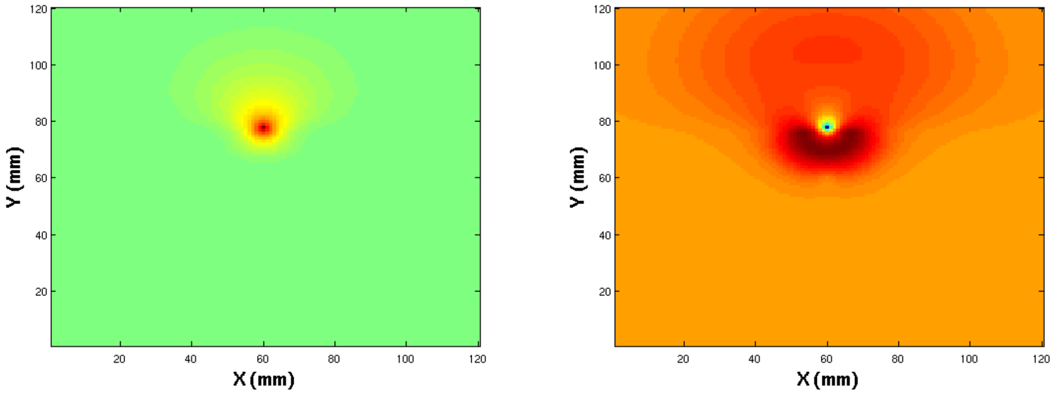

(c) 240th step (d) 280th step

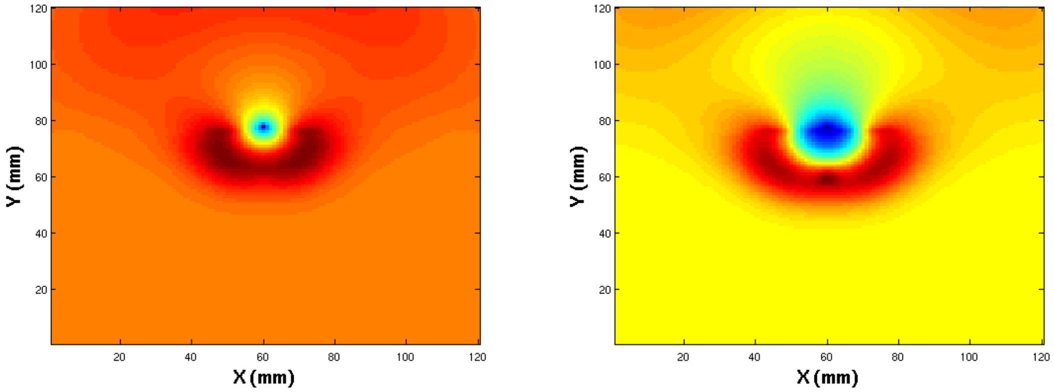

(e) 310th step (f) 340th step

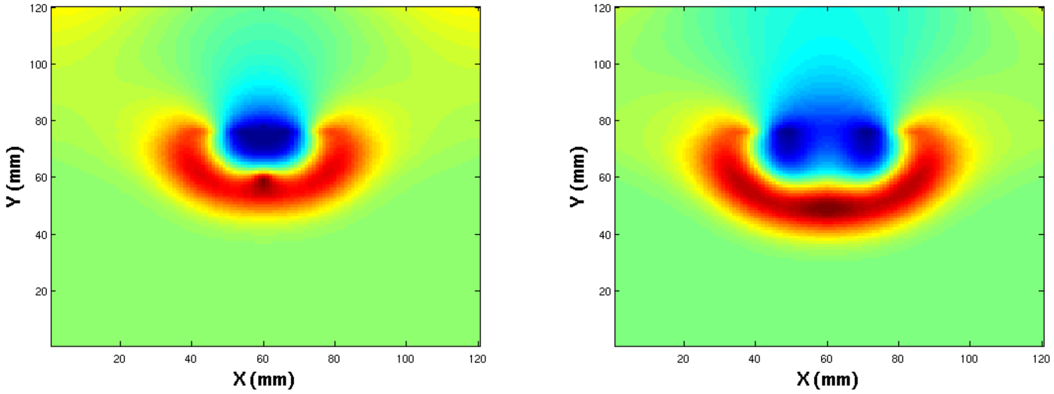

(g) 360th step (h) 400th step

Figure 2.7: continued figure, electric Field evolves within the computation region over time.

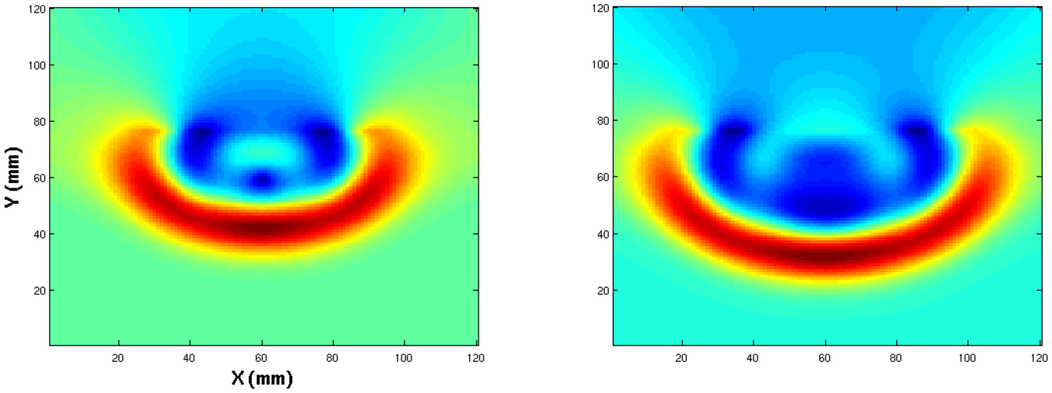

(i) 440th step (j) 500th step

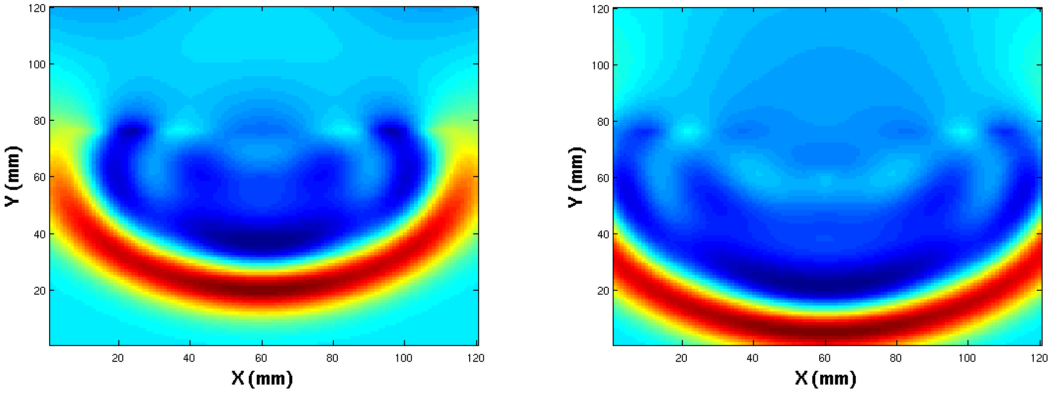

(k) 570th step (l) 650th step

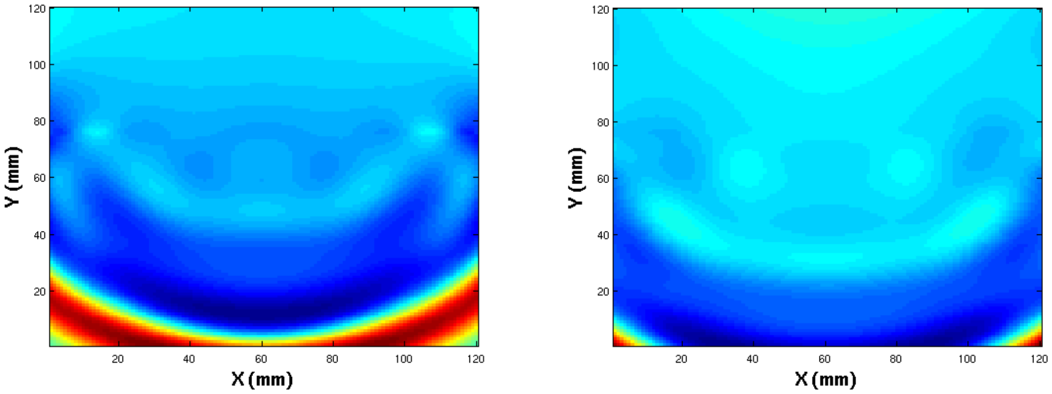

(m) 710th step (n) 810th step

Figure 2.7: continued figure, electric Field evolves within the computation region over time.

The entire process of simulation contains 1000 time steps and this takes less than 2 minutes. The signals recorded at 4 watching points (on the surface of skin layer) in the time domain converges very well. The success of 2-D simulation indicates that FDTD is able to imitate the process of transmission and receiving of microwave signals, and to provide effective data for breast cancer detection. In the next section, we will extend this simulation to 3D, with the same scheme described in this section.

2.4 3-D FDTD simulation

3-D FDTD is much more complicated, memory-consuming, and time-consuming than 2-D simulation. In this section, we develop a simple 3-D model for our FDTD simulation. Assumming that the grid size is still $\Delta x = \Delta y = \Delta z = 1mm$, and the time step remains $\Delta t = \frac{5}{3}ps$. The computation model, which approximates a compressed breast, is illustrated in Fig. 2.8.

A muscle layer has been added at the bottom of the model, which is 25 mm thick in the z direction. It has similar dielectric properties ($\epsilon_r = 50, \sigma = 4.0$) to that of the tumor. A spherical tumor, shown in red in Fig. 2.8, is $25mm$ beneath the skin layer. A transmitter, prepared to send out a UWB microwave pulse, is highlighted in green on the surface of the skin; Twenty-five receivers to collect the response from the tumor are placed on the surface of the skin. Above the skin is an air layer which is $30mm$ thick.

Since the rectangular model has six faces, the absorbing boundaries are designed to fit each part of the breast model. For the left, right, front, and rear faces, the absorbing boundaries are split into several layers to fit each layer in the breast model (muscle layer, breast tissue layer, skin layer and air layer).

The total computation volume is $120mm \times 120mm \times 107mm$. One simulation, containing 2000 time steps to allow the detecting signal transmission and the backscattered signals received at the antenna array, takes approximately 30 minutes on our linux computation server. Fig. 2.9 illustrates 4 selected signals obtained by 4 re-

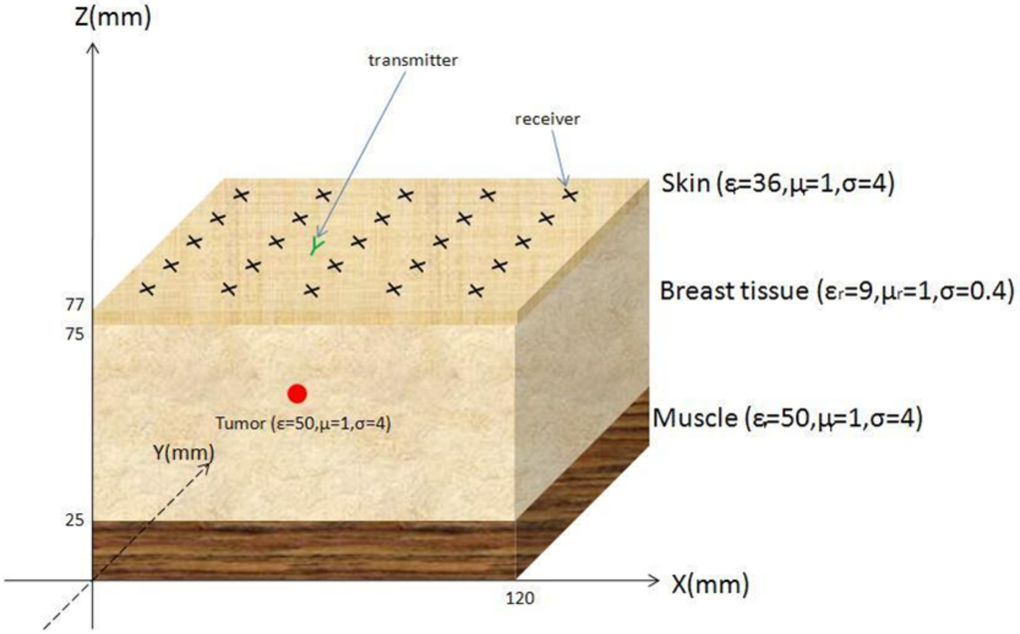

Figure 2.8: A rectangular breast model for microwave breast cancer imaging.

ceivers, respectively, of the collecting-antenna-array. Note that the signals collected by the receivers on the surface of the skin, are composed of the incident wave from the excitation source, the reflections from the interface between the skin and breast tissue, and the tumor response. Thus, a calibration step is required to extract the tumor response and will be discussed in the next chapter.

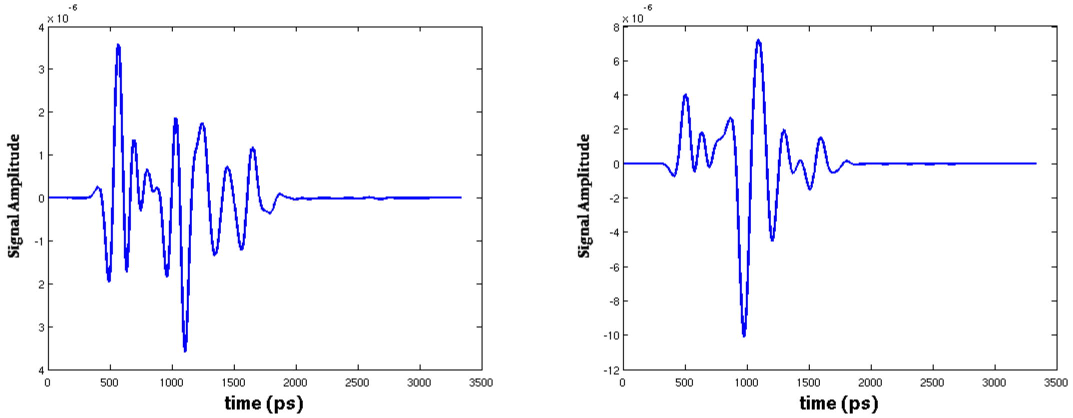

(a) Antenna No.1 (b) Antenna No.2

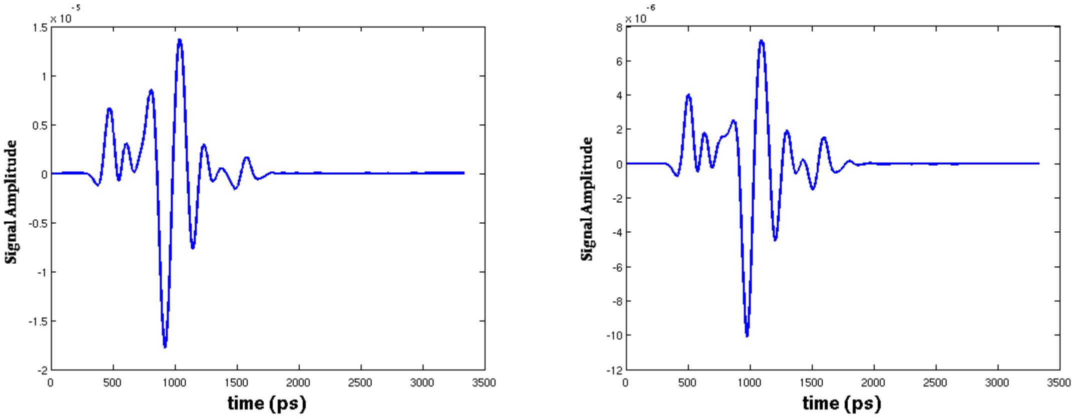

(c) Antenna No.3 (d) Antenna No.4

Figure 2.9: Signals obtained from 4 receivers.

CHAPTER 3: MICROWAVE IMAGING VIA SIMPLIFIED BREAST MODELS

In this chapter, two simplied breast models are employed to attempt detection of a malignant tumor, using the delay-and-sum(DAS) algorithm. The idea of multi-polarization detection will also be introduced in this chapter.

3.1 Antenna array and signal calibration

To detect a tumor growth in the breast, the simplified rectangular breast model shown in Fig. 2.8 described in section 2.4, is used in this section, as well as the UWB probing pulse introduced in Fig. 2.6. The antenna array utilized in our investigation, consisting of 25 elements, is shown in Fig. 3.1. The separation between the elements is $20mm$ in the x direction as well as in the y direction, and is less than the Nyquist sampling space for the pulse employed. Each element in the array is an electrically small dipole antenna (an advanced fabricated UWB antenna will be discussed in Chapter 6). Our 5×5 array creates an $80mm \times 80mm$ synthetic aperture in the horizontal plane at $z = 77mm$. Theoretically, the cross-resolution is proportional to the size of the synthetic aperture, i.e. the bigger the synthetic aperture the higher the cross resolution. However, the equation for calculating far-field resolution for synthetic aperture radar may not be suitable for near-field imaging. Therefore, we will use a numerical method to investigate the resolution problem. This will be discussed later in this chapter.

A simulated scan involves 25 independent signals recorded by the antenna array. These stored waveforms include the incident signal, skin reflection, and the tumor response. To isolate tumor reponse, a calibration process is required to remove the artifacts.

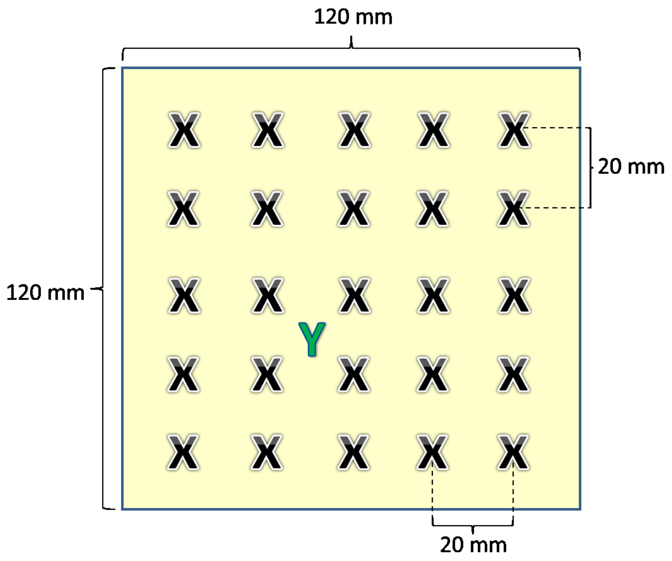

Figure 3.1: The antenna array for detecting tumor in the rectangular breast model.

There are two basic types of calibration methods: experimental method, and signal-processing method. A typical example of the experimental method is reported in [38], in which Klemm et al. proposed a symmetical antenna array to remove the undesired signal. Fig. 3.2 illustrates the symmetrical curved antenna array for microwave breast cancer detection applied in Klemm's experiment. By physically rotating the antenna array around its center, two or more radar measurements are performed. In these sets of measured data, undesired signals (skin reflection and mechanical-part reflection) are supposed to be identical and appear at the same time position, so that they can be eliminated. However, this method faces many limitations: (i) distance between antennas and skin must remain unchanged, (ii) skin properties and thickness must remain the same, and (iii) healthy breast tissue properties must be homogenous. The signal-processing method to remove unwanted artifacts can be quite complicated, such as in [68], where an algorithm based on multiplication of adjacent wavelet subbands is applied to enhance the tumor response while reducing the skin reflection. The skin responses are finally distinguished and eliminated in the

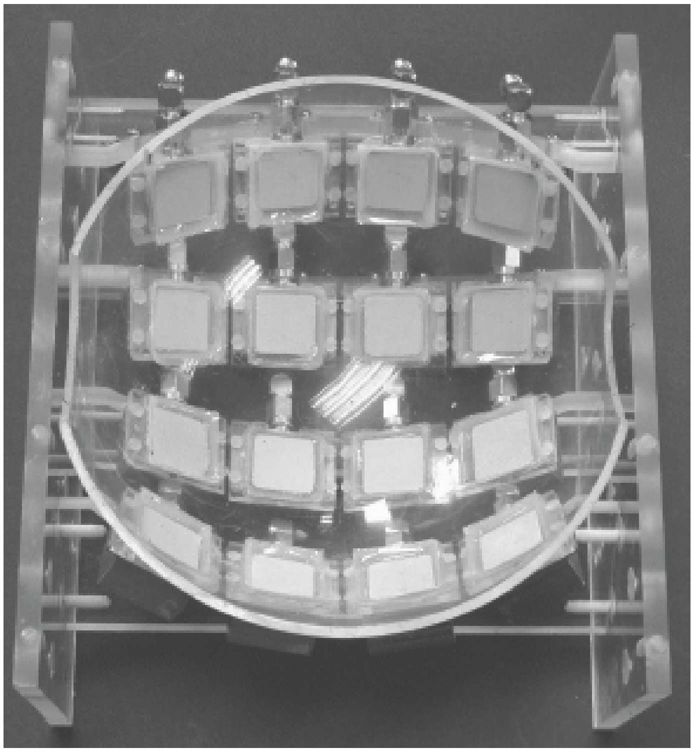

Figure 3.2: A self-symmetrical antenna array for microwave radar breast cancer detection in Klemm's experiment [38].

wavelet domain using an artificial threshold. Some relatively simple signal-processing methods, such as subtraction from the averaged skin reflection (see in [37]), are not necessarily able to yield the result in real world scenarios as desired. Therefore, to date, artifact removal is still a problem that needs to be overcome in the microwave breast-cancer-detection community.

In our investigation, the tumor response is extracted by subtracting a reference model, which is an indentical but tumor-free model from the tumor-included model. Since a regular tomography examination is recommended at least once each year [69], the previous exmamination data can be reasonably used as reference data. Since tissue properties may vary over time, in our investigation the breast model containing a tumor has ±10% random variation (in dielectric constant as well as conductivity for each cell) from the tumor-free model. In Fig. 3.3(a), the blue dashed curve represents

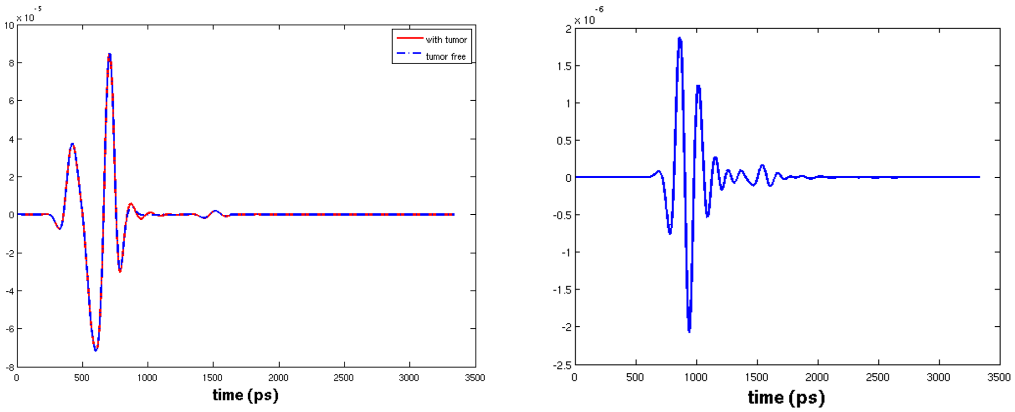

(a) (b)

Figure 3.3: Signal calibration. (a) signal obtianed by an antenna in a tumor-free/tumor-bearing model. (b) Tumor response, after the subtraction.

a signal obtained from a single receiver in a tumor-free model, while the red solid curve represents a signal obtained from the same receiver in a tumor-bearing model. In this figure, a notable difference appears only over a specific short time window, which is assumed to be the echo of the tumor. The calibrated signal, after subtraction, is illustrated in Fig. 3.3(b), which represents the tumor response. This result suggests that the tumor response is much weaker than the undesired signals, compared to the waveforms shown in 3.3(a). This method, using a *priori* information, though not perfect, helps us to easily obtain reliable tumor-response data for performance analysis of the imaging approach.

3.2 Delay and Sum

The DAS method, first proposed for breast cancer detection [10] [37], was designed for a monostatic detecting system. In this system, a UWB antenna is used as a transmitter as well as the receiver and is moved across the breast to form a virtual synthetic aperture. The tumor-backscatter signals received by all antennas, are time-shifted (phase-shifted) before they are summed to form a synthetic focal point. The

m^{th} time-delay, needed to compensate (shift) the m^{th} antenna for a given focal point, is given by

$$T_m(\overrightarrow{r}) = \frac{2d_m(\overrightarrow{r})}{v} \tag{3.1}$$

where $d_m(\overrightarrow{r})$ represents the distance between the focal point and the m^{th} transmitter/receiver element located at position $\overrightarrow{r}$, and v represents the average velocity of propagation in the breast at the center frequency of the pulse. In our multistatic detecting system, time delays from the transmitter to the target point are identical for any received signal, since only one transmitter is employed. Therefore, the time-delay required for compensation only contains the propagation from the target point to the receiver. Thus, the time-delay compensation in our multistactic system should be rewritten as

$$T_m(\overrightarrow{r}) = \frac{d_m(\overrightarrow{r})}{v} \tag{3.2}$$

where $(1 \leqslant m \leqslant 25)$. A multistatic system avoids the issue that the transmitting channel and the receiving channel must be highly isolated as in a monostatic system, since the echo of the tumor is extremely weak when compared with the transmitted microwave signal.

Finally, the summation of all time-shifted signals form the intensity of a pixel in the reconstructed image. This process can be expressed by

$$I(\overrightarrow{r}) = \left[\sum_{m=1}^{25} S(T_m(\overrightarrow{r})) \right]^2 \tag{3.3}$$

Note that in some applicaitons of the DAS algorithm, there is a weight term used to compensate the attenuation for each signal propagating in the breast. This compensation term was not used in our investigation since this artificial adjustment may cause additional undesired effects. Additionally, previous investigations have shown that an attenuation-compensated summation does not convincingly provide a better image over non-attenuation-compensated summation.

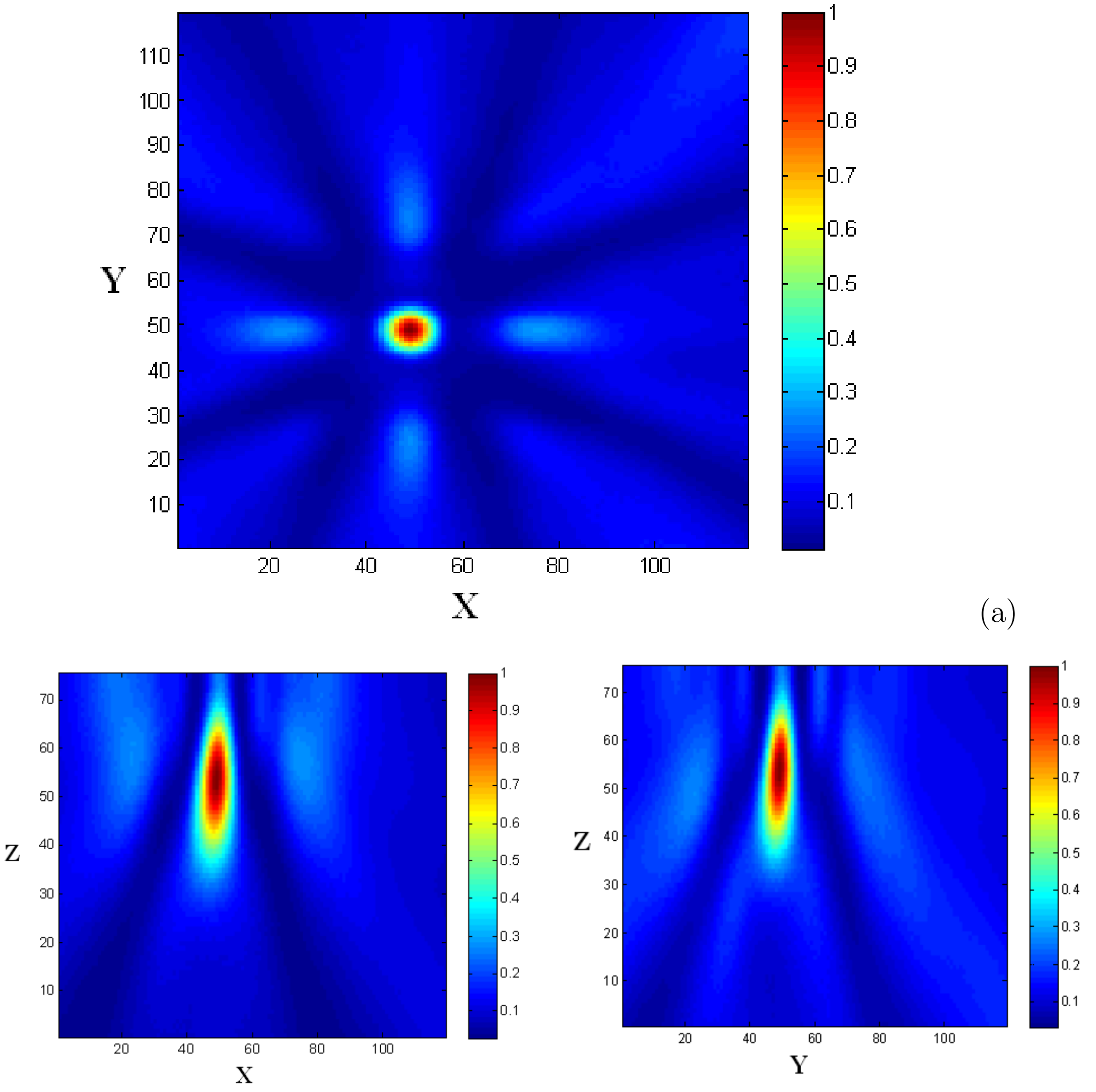

(a)

(b)

(c)

Figure 3.4: The reconstructed image (a) in the $x - y$ plane, (b) in the $z - x$ plane, and (c) in the $z - y$ plane. (unit: mm).

Since the signals add coherently at the target point and incoherently everywhere else, intensity at the target area is much stronger than any other location in the breast region. A focal-point scan throughout the breast was carried out in increments of 1 mm in x, y, as well as z directions in 3-D space. The reconstructed images are shown in Fig. 3.4. The red spot located at (50, 50) in Fig. 3.4(a) is the precise location of a 6-mm-diameter tumor in the FDTD model. Note that the suppression of clutter signals in the surrounding regions is quite good. This result demonstrates that the simulation data generated from our FDTD code are correct and effective. Some visible bright spots around the tumor represent leakages and can be reduced by increasing the number of antennas used in the array, or by image post-processing. The profile of the tumor in the coronal plane ($z - x$ plane) and in the sagittal plane ($z - y$ plane) is distorted, due to poor resolution in the z direction, resulting from no synthetic aperture in the z direction. In the next section, we will use a hemispherical breast model so a synthetic aperture can be formed in the z direction as well.

3.3 Hemispherical breast model

A hemispherical breast model is clearly more practical than a retangular model. In this section, a hemispherical model, shown in Fig. 3.5, is developed for the microwave breast cancer imaging.

In Fig. 3.5, a hemisphere with $100mm$ diameter, centered at (70,70,25), filled with breast tissues, and covered with a layer of $2mm$-thick skin, is positioned above a $25mm$ thick muscle layer (the muscle layer is shown in Fig. 3.6(a)). The black point in Fig. 3.6(a) and (b), embedded in the normal tissue represents a $6mm$ diameter malignant tumor. The dielectric properties of the fatty breast tissues are assumed to be Gaussian random variables with variations of $\pm 10\%$ around their nominal values. The nominal values are chosen to be typical of the reported data $[7] - [9]$ $[11] - [15]$, as summarized in Table 3.1. The glandular tissue is the main source of clutters because their dielectric properties have an upper bound very close to those of malignant tumors [11] [14]. The size of the glandular tissue ranges from 1 to 5 mm in diameter randomly and their locations are also random in the generated breast model. The randomly

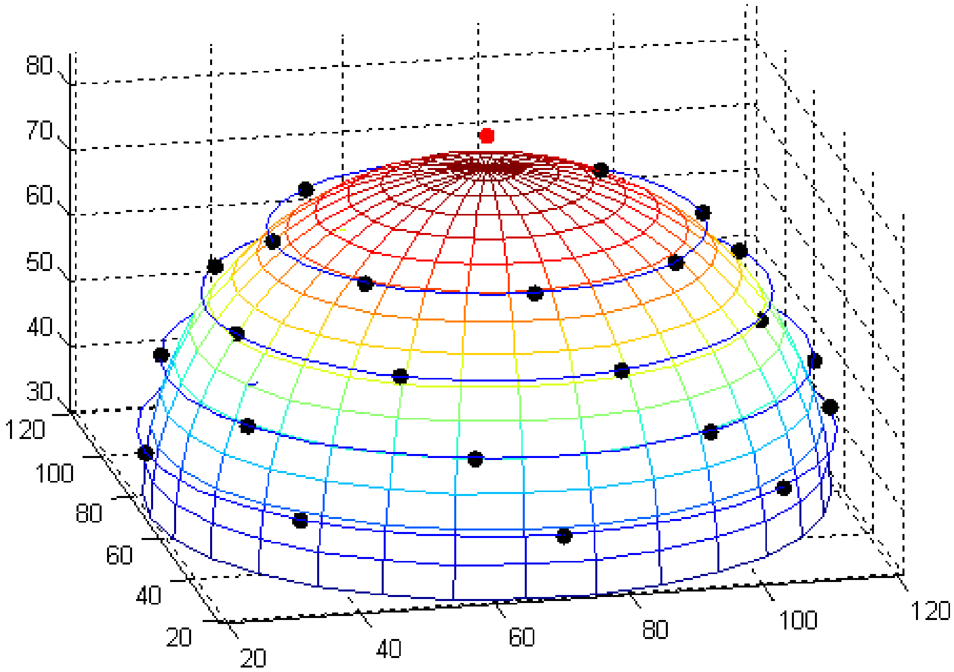

Figure 3.5: The simplified inhomogeneous hemispherical breast model viewed in 3D.

distributed breast tissues with variable dielectric properties are representative of the inhomogeneity of the breast of an actual patient.

Table 3.1: Nominal dielectric properties of breast tissues

Tissues	Permittivity (F/m)	Conductivity (S/m)
Immersion liquid	9	0
Muscle	50	4
Skin	36	4
Fatty Breast Tissue	9	0.4
Glandular Tissue	10-45	0.4-3.6
Tumor	50	4

A synthetic aperture antenna array, consisting of 32 elements (black points around the model), is positioned around the breast model in four layers as shown in Fig. 3.5, and each layer has 8 elements. Each element is assumed to be a dipole antenna and

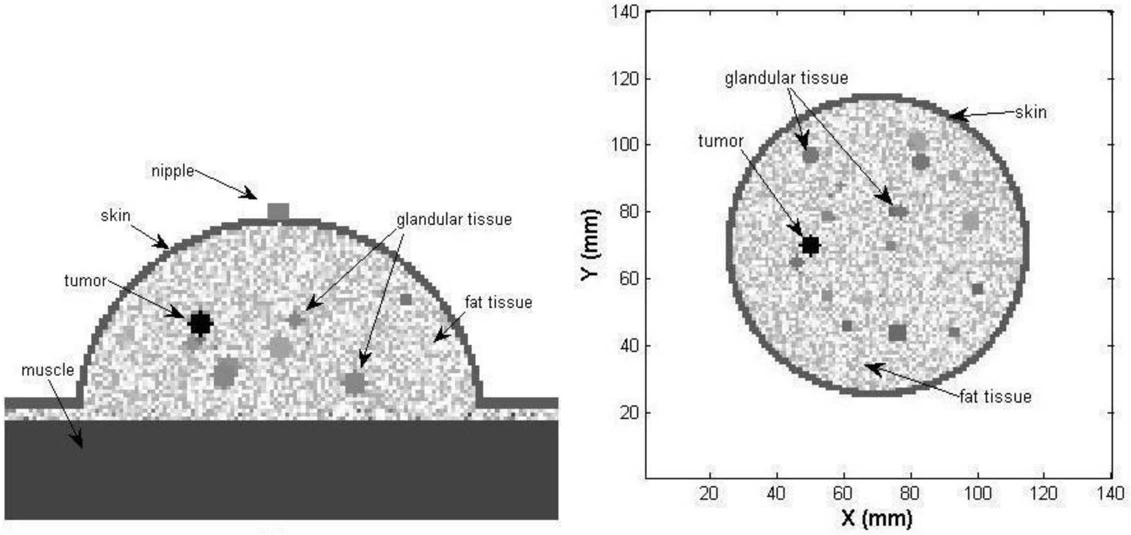

(a) (b)

Figure 3.6: Slice of the breast model. (a) coronal slice at $y = 70mm$; b) transverse slice at $z = 50mm$.

is positionad $2mm$ away from the surface of the skin. The dot on the top of the breast model shown in Fig. 3.5 represents the transmitter. To reduce the microwave reflection on the surface of the skin, allowing more signal energy to enter the breast, the breast model as well as the antenna array are assumed to be immersed in a coupling medium [70] [71], which has a similar dielectric constant to the breast fatty tissue. This design helps to reduce the impedance mismatch on the surface of the skin, and simplify the calculation of time delay in the DAS algorithm.

To obtain good resolution, a UWB pulse signal having wider bandwidth than the one previously described is employed in this program. Its time domain expression is a modulated Gaussian pulse:

$$V(t) = sin(2\pi ft)exp\left[-\left(\frac{t-t_0}{\tau}\right)^2\right] \tag{3.4}$$

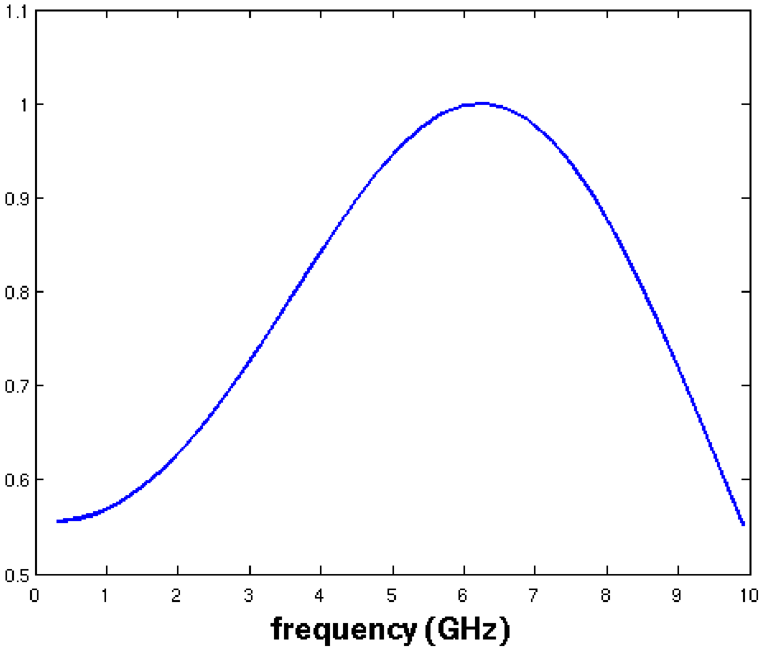

Figure 3.7: Spectrum of the UWB signal for the hemispherical model detection.

where $f = 6.25GHz$, $\tau = 50ps$, and $t_0 = 4\tau$. This pulse is centered around 6.25 GHz and has a full-width at half-maximum (FWHM) bandwidth of approximately 10 GHz, which is shown in Fig. 3.7.

The whole computation region, including the breast model, the antenna array, and the coupling medium, is $140mm \times 140mm \times 107mm$. The grid size $\Delta x = \Delta y = \Delta z = 1mm$, and time step $\Delta t = \frac{5}{3}ps$ are used in this 3-D FDTD simulation. The computaion time for one transmission and the backscattered signals to be received at the antenna array is approximately 40 minutes (2000 steps) on our linux server.

The DAS algorithm is used here to obtain a reconstructed image. Fig. 3.8 shows the 3-D images obtained via DAS method. The shaded hemisphere represents the contour of the breast, and the dotted shades inside correspond to the intensity of the backscattered energy estimates. The image is displayed on a logarithmic scale with a 3 dB dynamic range (focal points with backscattered energy lower than -3 dB

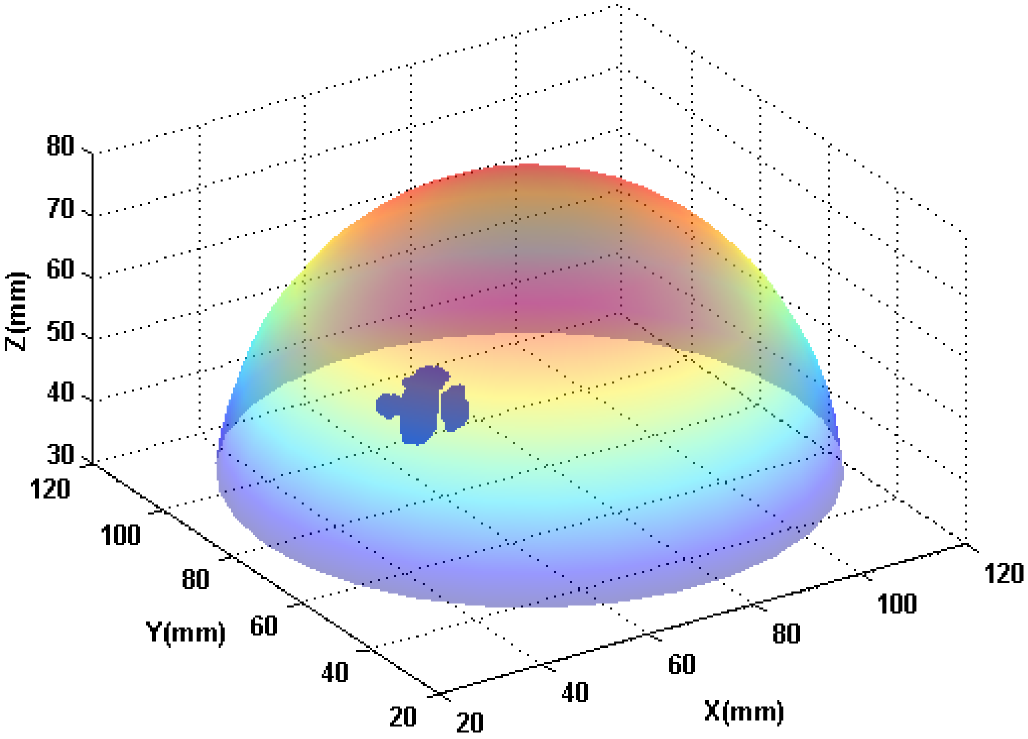

Figure 3.8: 3-D image of a 6 mm in diameter tumor obtained via DAS method. The dotted shades inside the breast are the intensity of the backscattered energy estimates.

are removed). The tumor is conspicuously shown in the correct location defined in FDTD with visible clutters around it. Fig. 3.9 shows the reconstructed image in x-y (transverse), x-z (coronal), and y-z (sagittal) cross section images with all the focal points on display. The tumor is clearly located at (50,70,50), in the cartesian coordinate from these sliced images. The resolution in the vertical direction (z-direction) is much better than in the retangular model due to the geometry of the array. There is a strong clutter near the tumor, which may make it difficult to distinguish the profile and stage of the tumor in real diagnosis.

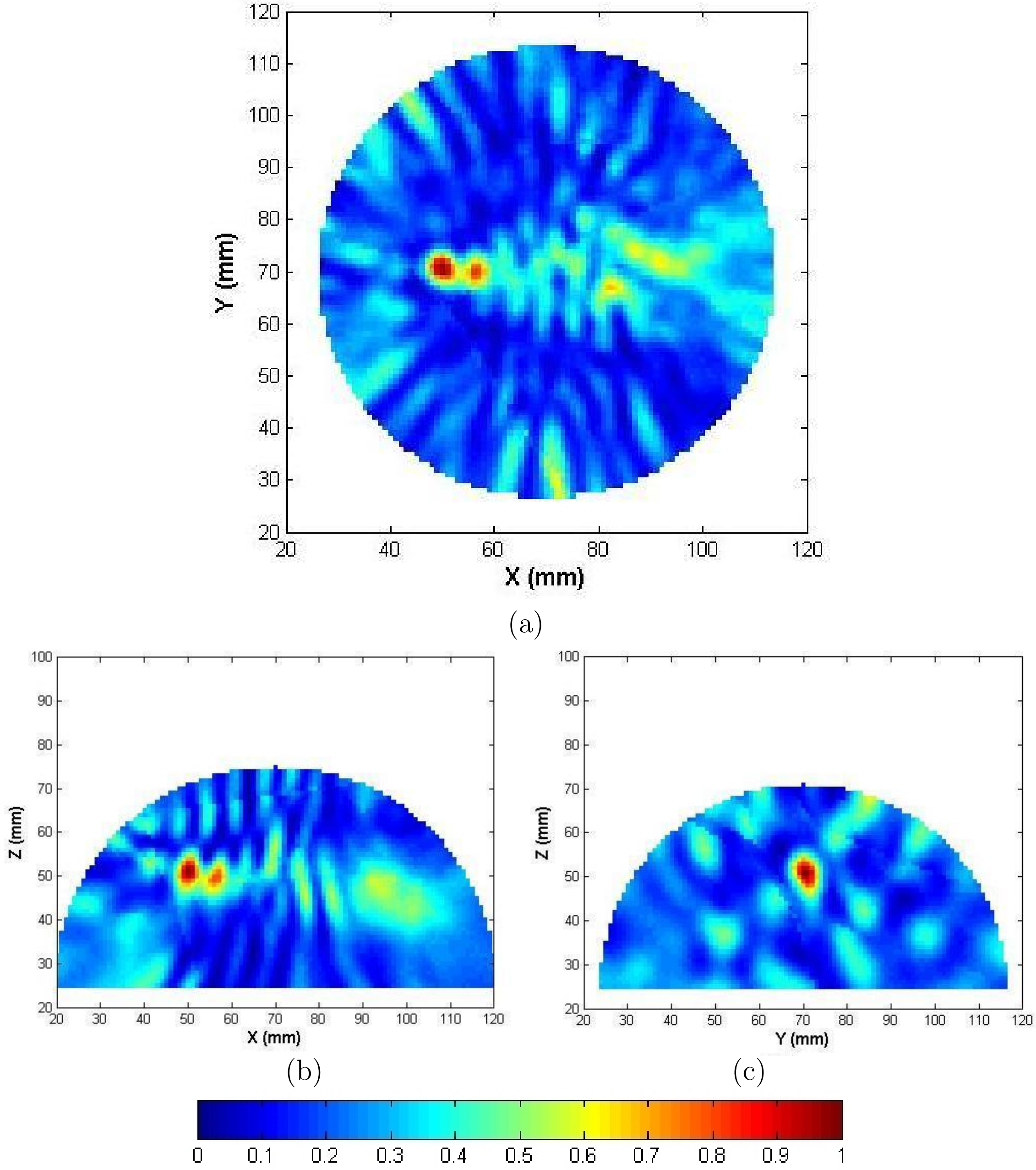

(a)

(b)

(c)

Figure 3.9: The Cross sections of the reconstructed image. (a) in transverse plane, (b) in coronal plane, and (c) in sagittal plane.

Note that our multistatic scheme is different from the multistatic method introduced in some articles, such as in [39] [49] [50], where each antenna in the array takes turn to transmit a probing pulse and all antennas in the array are used to receive the backscattered signals. That approach is equivalent to our simulation repeated N times, where N is the number of antennas in the array. For instance, in reference [50], 64 antennas were used which implies 64×64 series of signal are summed in the beamforming image reconstruction. Therefore, the final reconstructed images are naturally different than those presented here. Since the approach in [50] may take a long time to complete the simulation, we developed a multi-polarized method, in which several transmitters, instead of all antennas in the array, are used and each takes its turn to transmit a probing pulse. Relatively speaking, our enhanced method is able to improve the quality of the reconstructed image and save simulation (or microwave scan) time.

3.4 Image reconstruction with multi-polarized signals

In this section, we develop an enhanced method to image the backscattered-energy distribution within the hemispherical breast model. This method is able to improve the image quality over the results obtained in the previous section.

3.4.1 Single target detection

Naturally, a specific polarized signal brings specific information, and dictates the resolution in a certain direction. Thus, we attempt to use two kinds of linearly-polarized electric signals as a probing signal to illuminate the breast model. In Fig. 3.10, four dipole antennas positioned around the breast model shown in red arrows, are polarized in the $+y$, $+x$, $-y$, and $-x$ direction respectively. Each transmitter is $4mm$ away from the surface of the skin and sends out a probing pulse, after a previous transmission by another excitation and collection by the array. The locations of the excitation antennas have been moved from the top to the sides of the model, to allow better imaging of tumors growing near the skin. The array used to collect the backscattered signals remains unchanged. The probing pulse in each transmission is the 10 GHz bandwidth signal, shown in Fig. 3.7, which was employed in the previous investigation. Since each excitation and collection is an independent event, multi-

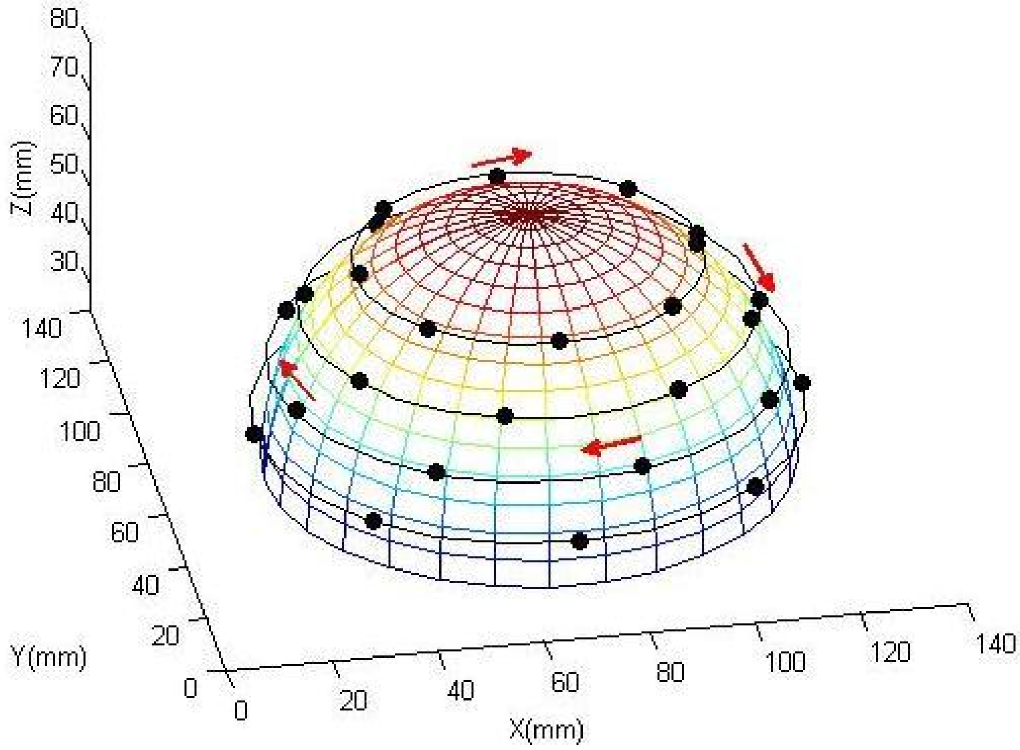

Figure 3.10: The multi-polarization scheme for the multistatic imaging.

core simultaneous computation, with each core dealing with an independent FDTD simulation, is applied in our scheme. Therefore, the computaional time for the entire scheme to complete, is approximately equivalent to a single-excitation simulation.

The signal calibration step and time-delay compensation are processed similar to the previous section. Consequently, the intensity of each focal point is summed by a group of four backscattered signals and each has 32 series, i.e.

$$\begin{aligned} I(\overrightarrow{r}) = & \left[\sum_{m=1}^{32} S_{+y}(T_m(\overrightarrow{r}))\right]^2 + \left[\sum_{m=1}^{32} S_{+x}(T_m(\overrightarrow{r}))\right]^2 \\ & + \left[\sum_{m=1}^{32} S_{-y}(T_m(\overrightarrow{r}))\right]^2 + \left[\sum_{m=1}^{32} S_{-x}(T_m(\overrightarrow{r}))\right]^2 \end{aligned} \tag{3.5}$$

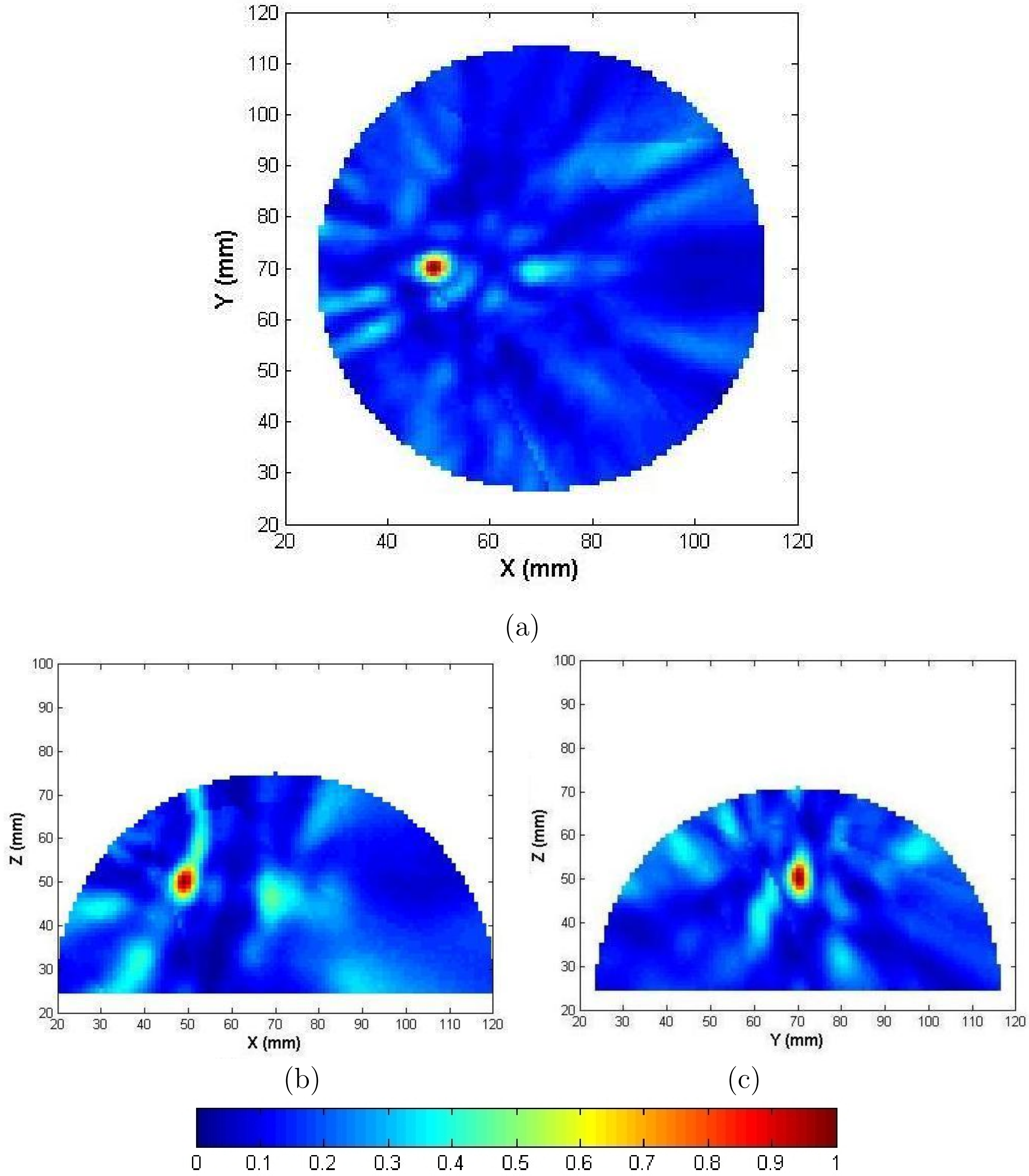

(a)

(b)

(c)

Figure 3.11: The reconstructed images using multi-polarized scheme shown in Fig. 3.10. a) in transverse plane, (b) in coronal plane, and (c) in sagittal plane.

The reconstructed images are shown in Fig. 3.11. Compared to Fig. 3.9, the clutters in each counterpart of Fig. 3.11 have experienced significantly improved suppression. The highlighted dot in the figure which stands for the mapped energy of a tumor, is easily distinguished from the background [72].

This scheme provides better resolution in the horizontal plane (x-y-plane image such as Fig. 3.11(a)) than any single-polarized detection with probing signal polarized in the x-y plane. The polarization of the probing signal in our investigation does not take z direction into account due to the radiation of a dipole antenna. In the remainder of this section, we will investigate the resolution problem of the proposed approach.

3.4.2 Dual target and resolution

Resolution is an important reference index to evaluate an imaging system. Since microwave medical imaging is a type of near-field imaging, the equation proposed for radar-imaging resolution may not be appropriate for near-field medical imaging. However, the resolution of near-field imaging does follow some basic criteria.

Generally, range-resolution is determined by the equation [73]

$$\delta = \frac{v}{2B} \tag{3.6}$$

where, v is the speed of wave propagation, and B is the bandwidth of the detecting signal. Therefore, high range-resolution is obtained when a wide-band detecting signal is applied. This is the reason UWB signals are employed for breast cancer detection.

The cross-resolution is assummed to be proportional to the elevation angle θ, depicted in Fig. 3.12(a), i.e., the bigger the elevation angle, the higher the cross-resolution. Therefore, cross-resolution is limited in the rectangular breast model due to its geometry and the structure of the antenna array, shown in Fig. 3.12(a) (or 3-D model in Fig. 2.8). On the other hand, the array used for the hemispherical model forms a large elevation angle, shown in Fig. 3.12(b), which is able to yield a high

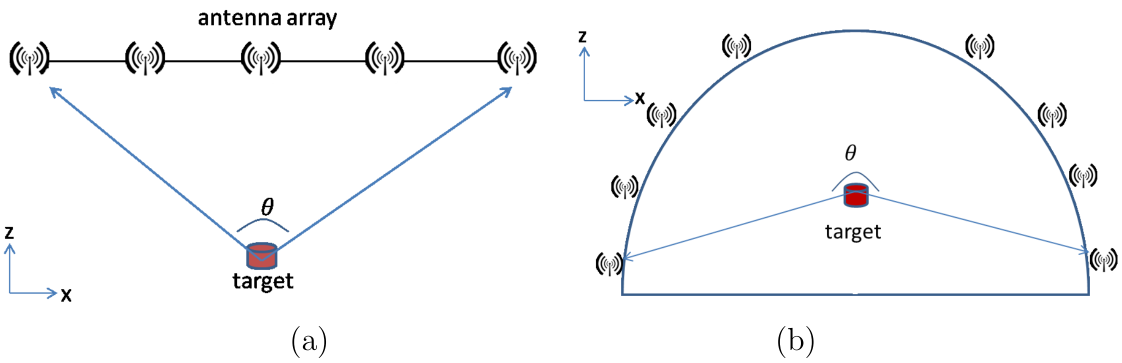

(a) (b)

Figure 3.12: The elevation angle affects the resolution. The elevation angle in (a) is smaller than in (b), which implies a relatively poor image resoltution.

cross-resolution. Meanwhile, the resolution in z-direction can be improved since a synthetic aperture is also formed in the z-direction.

In this subsection, a dual-tumor case [74] is used to investigate resolution of the imaging method proposed within this chapter. In general, imaging resolution is defined by the minimal distance between two targets at which two targets can still be distinguished in the reconstructed image. Typically, it can be characterized by a -3 dB drop of the power level in the reconstructed image. Since resolution of the hemispherical system is superior to the rectangular system, in this section, the horizontal (x-y plane) resolution is investigated only through the hemispherical breast model. Moreover, due to the symmetry of the sphere, it is difficult to distinguish the definition of range-resolution and cross-resolution in the hemispherical model, therefore a discussion of z-direction resolution is ommited.

A pair of spherical targets with identical diameter of 6 mm, were positioned in the center of the breast model. The hemispherical breast models with and without tumors differ with ±10% random variation. Using the antenna scheme depicted in Fig. 3.10, we try to distinguish both of the targets with minimal distance between them. Fig. 3.13 shows the reconstructed image with multi-polarized DAS method when two targets are placed 13 mm apart in the FDTD simulation. Two targets

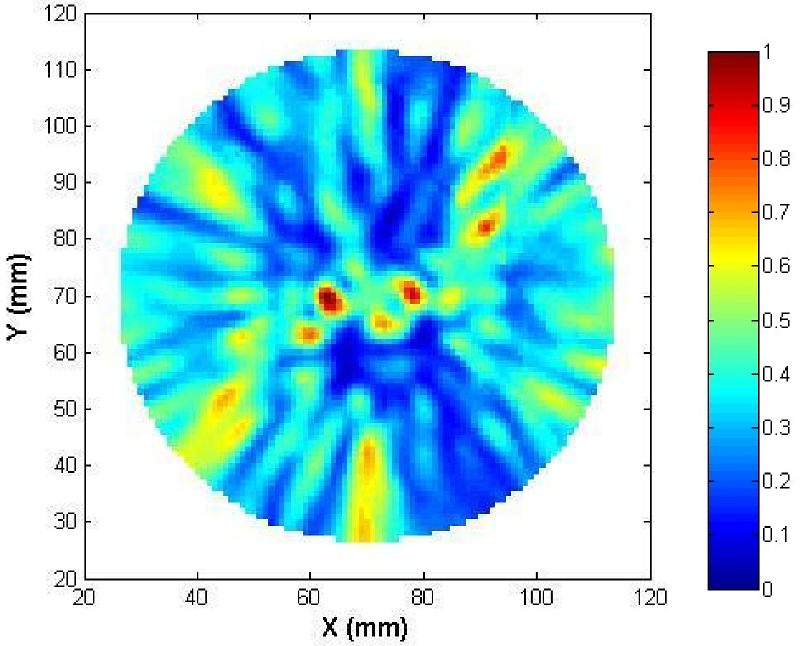

Figure 3.13: Reconstructed image for a pair of targets with 13 *mm* apart using multi-polarized DAS method.

can be distinguished well in this case but with slight distortion of the location and poor contrast. As the center distance moves to 11 *mm*, a very poor-contrast image is obtained, shown in Fig. 3.14. Two targets cannot be distinguished clearly for this case, and some focal points between two tumors have scattered energy that exceed -3 dB of the peak tumor response. Additionally, many strong clutters are present in this image and some of their scatterd energy have reached the level of the tumor. It turns out that to distinguish the tumor from the clutters is difficult with this image. To summarize, the resolution of the proposed imaging system, accompanied with the DAS image reconstruction algorithm, is approximately 13 *mm*. Meanwhile, this conclusion demonstrates that microwave breast cancer imaging is a type of centimeter-resolution detection.

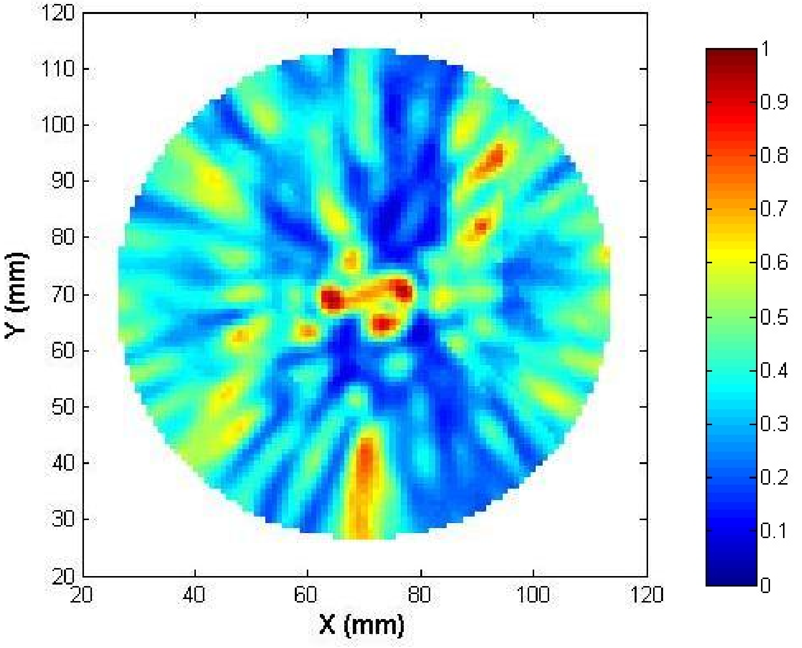

Figure 3.14: Reconstructed image for a pair of targets with 11 *mm* apart using multi-polarized DAS method.

To compare with the multi-polarized method, we also investigated using a single-excitation strategy with the antenna array shown in Fig. 3.5 to detect dual targets. However, nothing can be concluded from these figures, whether the distance between two targets is 13 *mm* or 11 *mm*. The reconstructed images are shown in Fig. 3.15 and Fig. 3.16. The actual tumor locations merely exbihit extremely weak-bright dots, and clutters are even stronger than the targets.

In this chapter, we have demonstrated the advantage of the multi-polarized antenna strategy. The DAS algorithm is a simple, effective approach and has certain robustness, for detecting an early-stage breast tumor. However, a real human-breast can be highly heterogeneous, which means its dielectric properties may be more inhomogeneous than the models we developed in this chapter. In the next chapter, we will propose a more advanced algorithm to treat an MRI-derived breast phantom, which exhibits the dielectric properties of the human breast tissues more realistically.

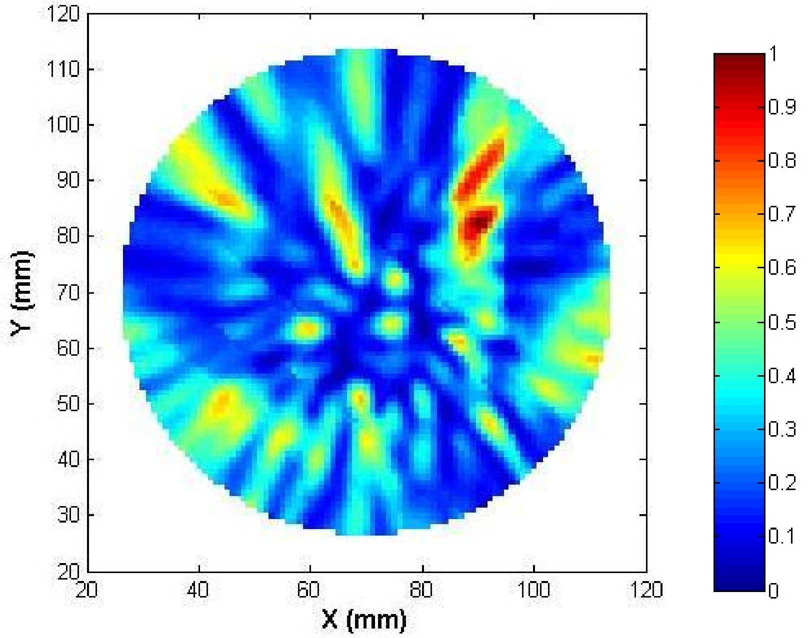

Figure 3.15: Reconstructed image for a pair of targets with 13 *mm* apart using single-excitation strategy.

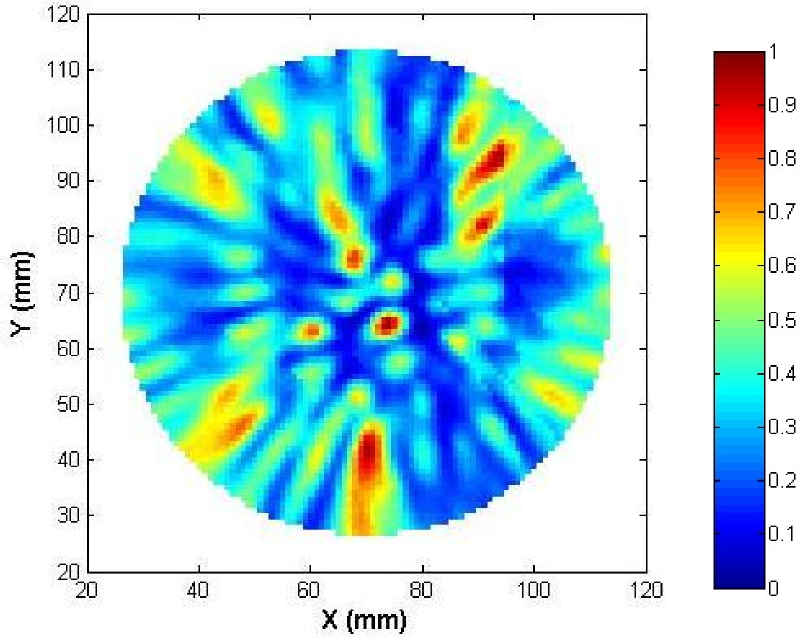

Figure 3.16: Reconstructed image for a pair of targets with 11 *mm* apart using single-excitation strategy.

CHAPTER 4: ADVANCED MICROWAVE IMAGING VIA MICROWAVE POWER IMAGING (MPI)

The inhomogeneity of the dielectric constant of breast tissues cause variation in wave velocities propagating in them. For near-field imaging such as a breast survey, propagation of the wave is restricted to a short distance, therefore, small variations of the time delay (typically $\leqslant 10\%$) will not cause significant impact on the image reconstruction (a review of this result can be found in [75]). However, for highly heterogeneous breasts, the complexity of wave propagation in the breast increases, and the simple DAS method faces difficulties in distinguishing the cancerous part within a breast over the clutters, principally induced from fibroconnective tissue or glandular tissue. In this chapter, a new type of confocal microwave imaging method - microwave power imaging algorithm, is proposed to image a spherical tumor within an MRI-derived breast phantom, which is more complicated, but more realistic than models discussed in previous chapters.

4.1 Fields generated by a linearly-polarized dipole

To clearly describe the algorithm, it is necessary to understand each component of the field (in Cartesian coordinates) generated by a linearly-polarized dipole source.

We position an electric dipole, linearly polarized in the y-direction, in the center of the computation region (140 $mm\times$ 140 $mm\times$ 107 mm, in the air) and use the 3-D FDTD method to observe the generated electric field and magnetic field in three cross-section planes, shown in Fig. 4.1. Note that what we care about is the wavefront, i.e., the propagation of the phase, rather than field amplitude.

Figs. 4.2 $-$4.7 show the E_y, E_x, E_z, H_y, H_x, and H_z field in three section-plane, respectively, after a modulated-Gaussian pulse is fully generated. From these figures,

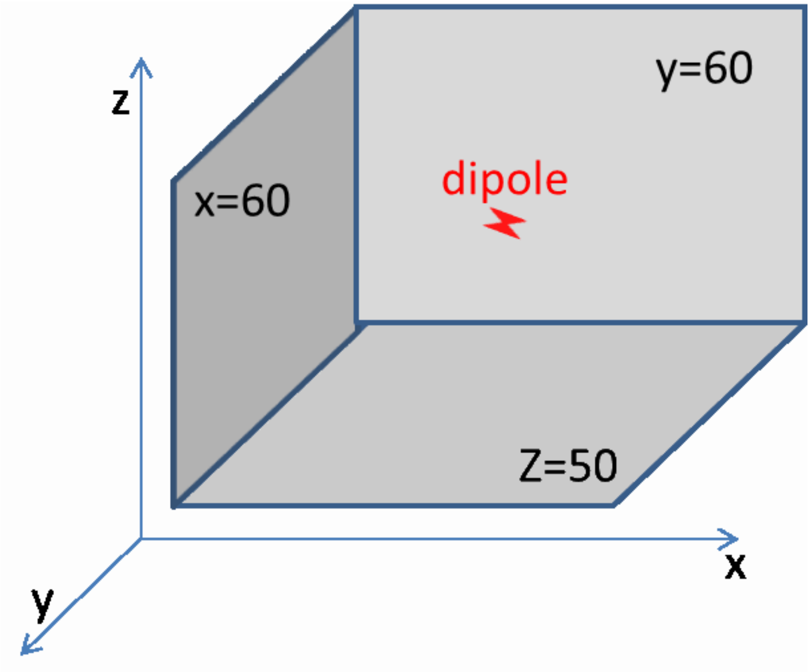

Figure 4.1: Observe the field generated by a electric dipole in three cross-section plane: horizontal plane (x-y plane with z=50), coronal plane (z-x plane with y=60), and sagittal plane (z-y plane with x=60). The center position of the dipole is (70,70,55), in the cartesian coordinate.

it can be concluded that the wavefront (i.e. phase) of the E_y field, generated by the y-direction-linearly-polarized dipole, is spherically symmetric in space; the wavefront of E_x and E_z is spherically anti-symmetric about a 45°-tilted plane, respectively. The wavefront of H_x is spherically anti-symmetric about a horizontal plane in which the dipole is located; the wavefront of H_z is spherically anti-symmetric about a vertical plane in which the dipole is located. And nothing can be concluded about H_y from the figure.

Similarly, the scattered field generated by a scatter that is illuminated by a transmit field should have the same response since the scatter is the source of a scattered field. The DAS algorithm similar to the one employed in Chapter 3 is described as follows: if the excitation antenna is linearly-polarized in the y-direction, the collected E_y-backscattered signals can be summed coherently at each target location

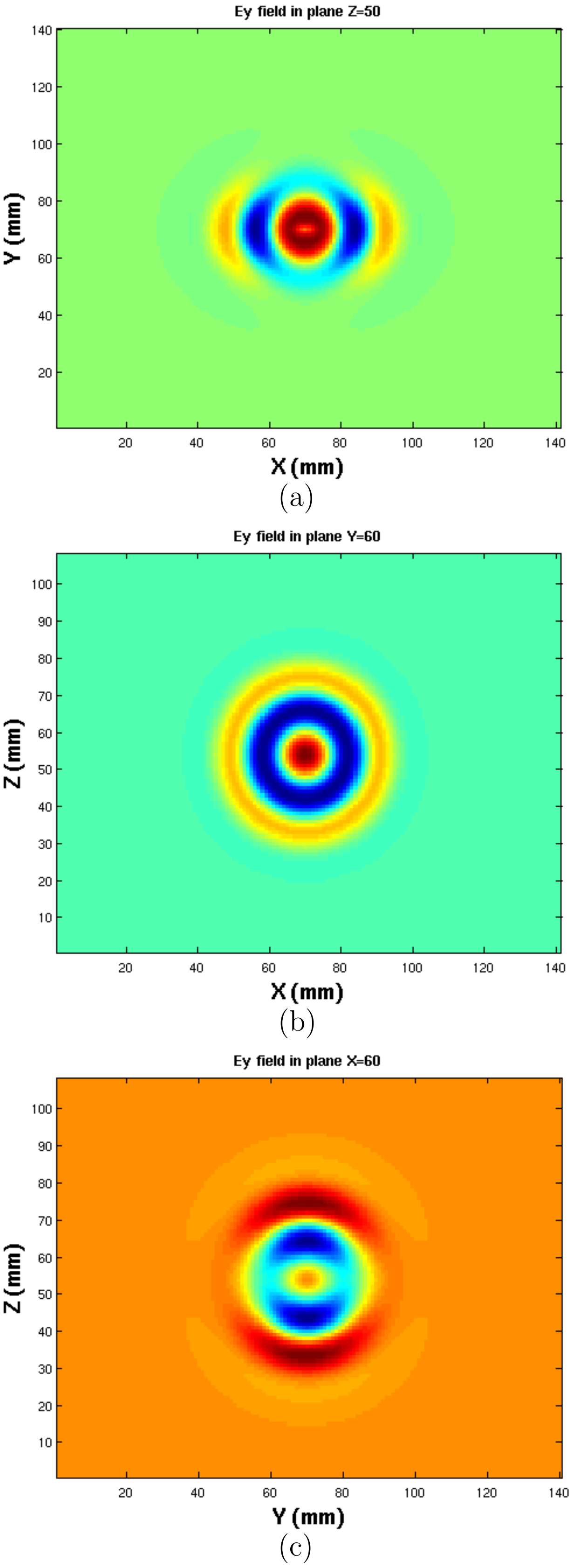

Ey field in plane Z=50

(a)

Ey field in plane Y=60

(b)

Ey field in plane X=60

(c)

Figure 4.2: The E_y field generated by the dipole source, observed in (a) horizontal plane, (b) coronal plane, and (c) sagittal plane, respectively shown in Fig 4.1.

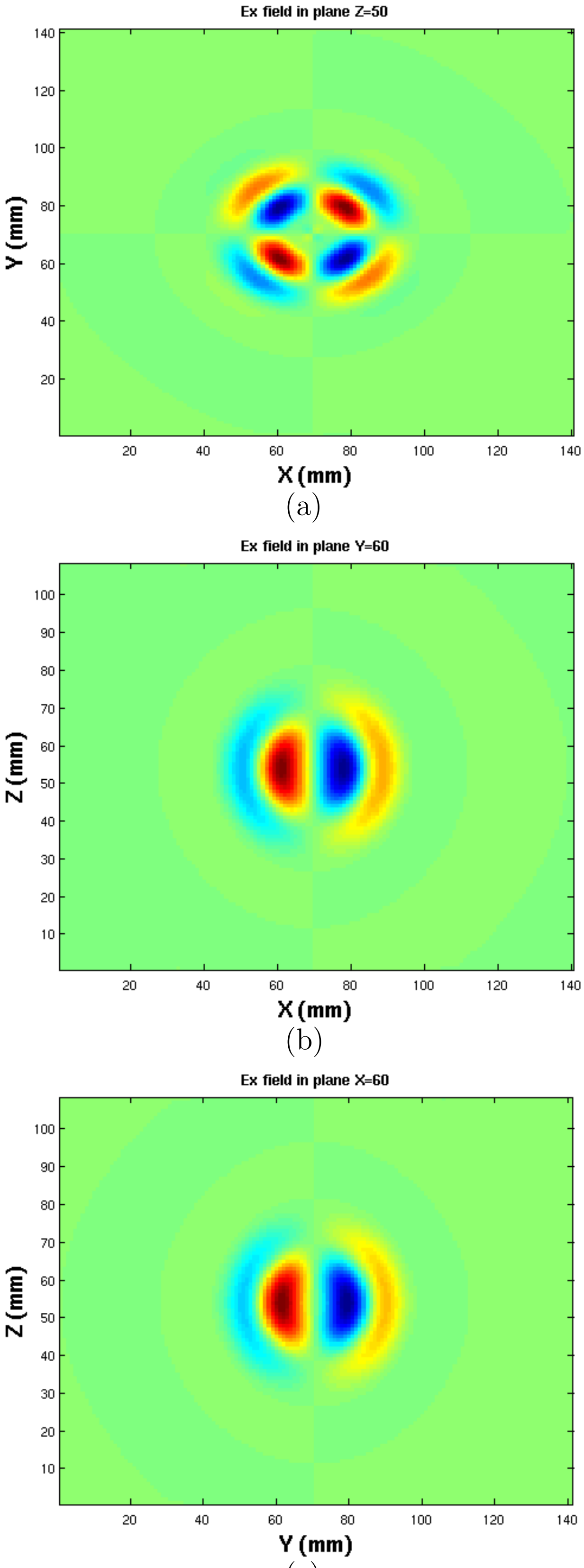

(a)

(b)

(c)

Figure 4.3: The E_x field generated by the dipole source, observed in (a) horizontal plane, (b) coronal plane, and (c) sagittal plane, respectively, shown in Fig. 4.1.

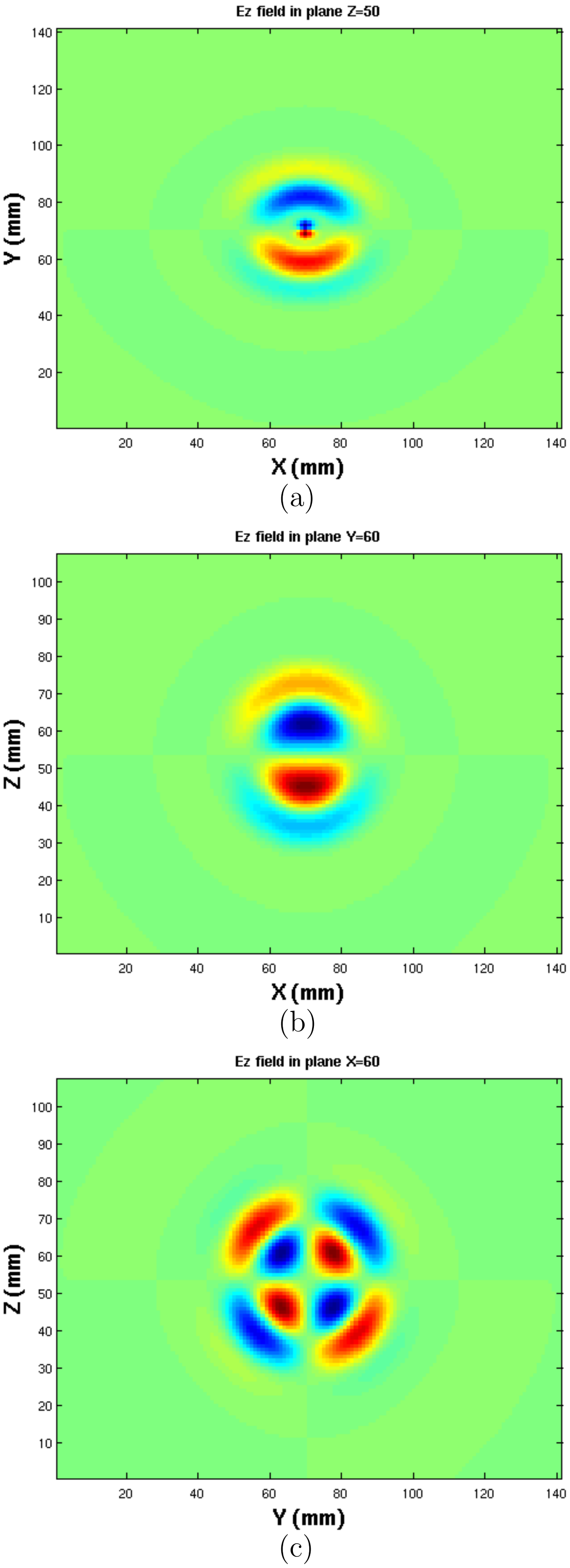
Ez field in plane Z=50

(a)

Ez field in plane Y=60

(b)

Ez field in plane X=60

(c)

Figure 4.4: The E_z field generated by the dipole source, observed in (a) horizontal plane, (b) coronal plane, and (c) sagittal plane, respectively, shown in Fig .4.1.

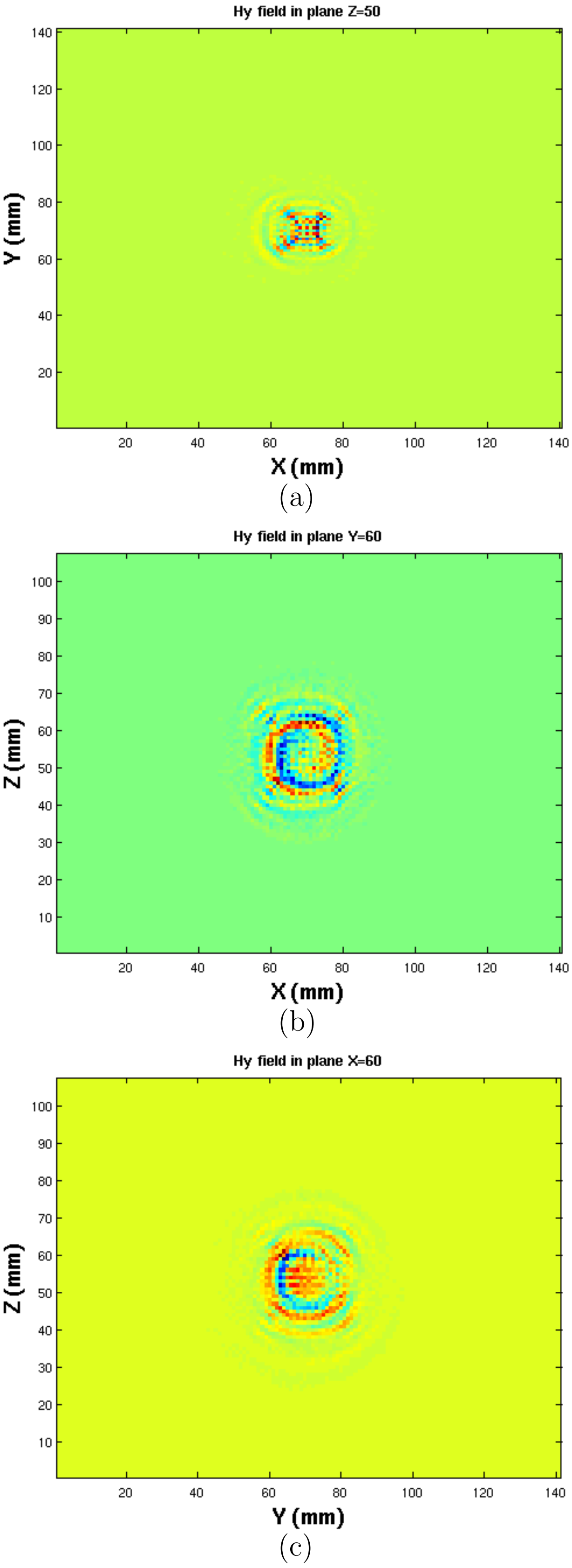

Figure 4.5: The H_y field generated by the dipole source, observed in (a) horizontal plane, (b) coronal plane, and (c) sagittal plane, respectively, shown in Fig. 4.1.

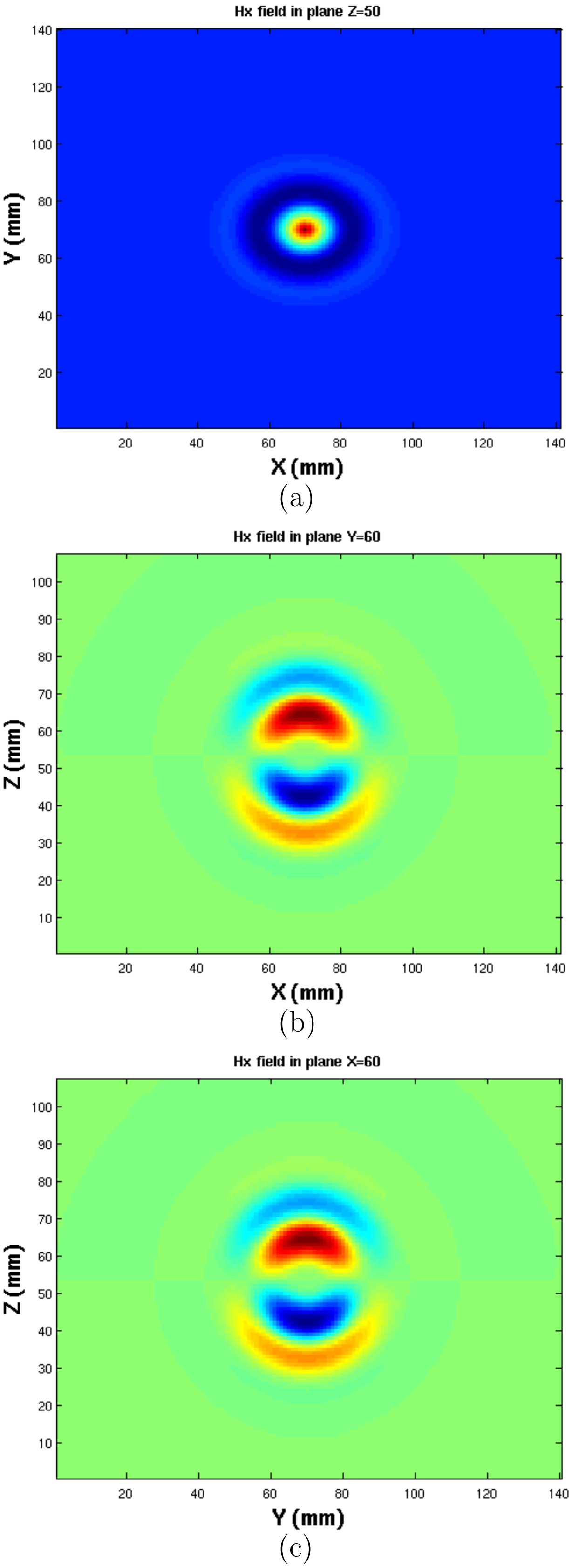

(a)

(b)

(c)

Figure 4.6: The H_x field generated by the dipole source, observed in (a) horizontal plane, (b) coronal plane, and (c) sagittal plane, respectively, shown in 4.1.

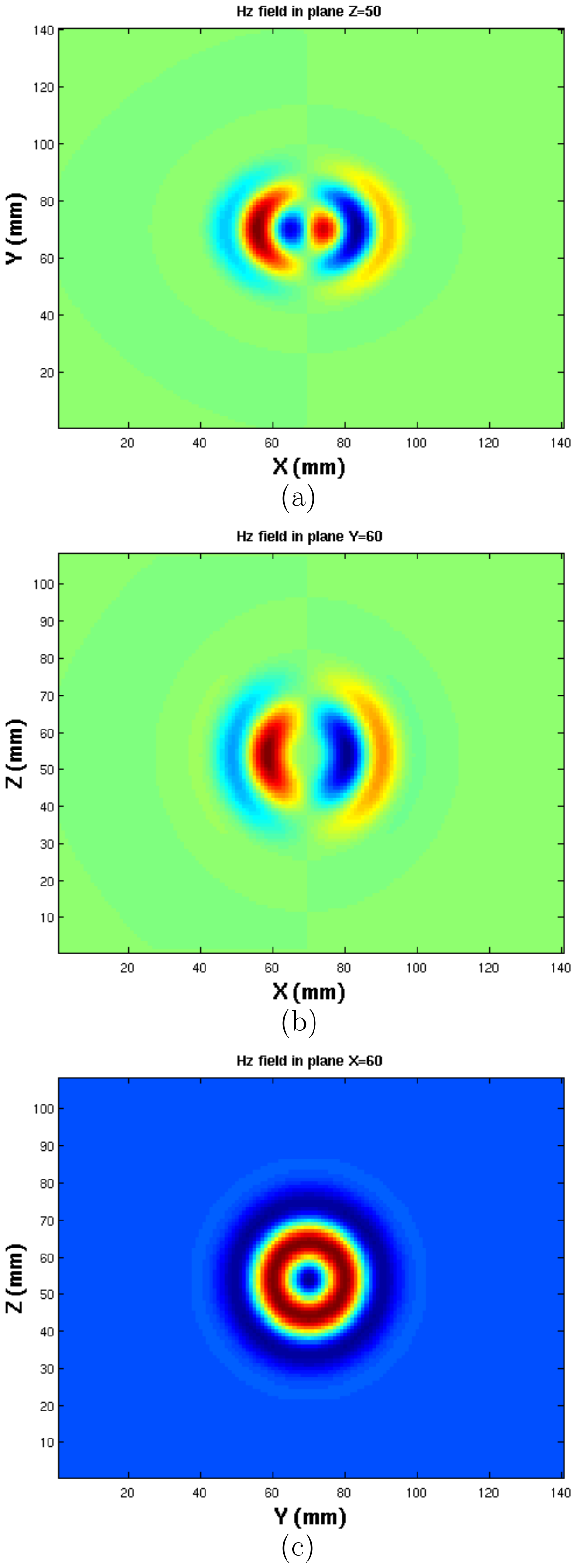

(a)

(b)

(c)

Figure 4.7: The H_z field generated by the dipole source, observed in (a) horizontal plane, (b) coronal plane, and (c) sagittal plane, respectively, shown in Fig. 4.1.

after time-delay compensation, through Eqn. 3.3, because of the spherical symmetry of E_y. However, other electric and magnetic components are not able to reconstruct an image merely using Eq. 3.3, due to their spatial asymmetry.

Our improved algorithm aims at applying both the electric-field signal and the magnetic-field signal, and combining them to achieve more information from the target, in order to reconstruct a high-contrast image. Dipole antennas are employed throughout our investigation. However, advanced UWB antenna design and fabrication will be discussed in Chapter 6. In the next section, the proposed algorithm will be described in detail.

4.2 MPI and multi-polarized MPI

It is desired to improve the efficacy of the multistatic confocal microwave imaging algorithm by including the magnetic field with the electric field in the formulation [76]. The combination includes more backscatter information and is assumed to provide a better-quality image. To do so, we have chosen to combine the two fields into a Poynting like vector that represents the magnitude and direction of power flow within the system. At any point in Cartesian space, the Poynting vector is given by

$$\begin{aligned}
\mathbf{P} = \mathbf{E} \times \mathbf{H} = &\begin{vmatrix} \hat{x} & \hat{y} & \hat{z} \\ E_x & E_y & E_z \\ H_x & H_y & H_z \end{vmatrix} \\
=&(E_yH_z - E_zH_y)\hat{x} + (E_zH_x - E_xH_z)\hat{y} + (E_xH_y - E_yH_x)\hat{z} \\
=&P_x \cdot \hat{x} + P_y \cdot \hat{y} + P_z \cdot \hat{z} \qquad (4.1)
\end{aligned}$$

where $P_x = E_yH_z - E_zH_y$, $P_y = E_zH_x - E_xH_z$, and $P_z = E_xH_y - E_yH_x$. All the electric and magnetic field signals are assumed have been time shifted within this section, except where otherwise noted.

At any instant in time, a single antenna operates in transmit mode and many other antennas receive the response to that transmitted signal. Suppose that the transmitted electric field is polarized along the y-direction, then P_x and P_z at the receivers are likely to provide meaningful results. If the z-direction is assumed to point away from the body, then P_z contains reflections from the tumor as well as significant reflections from the muscle layer beneath the breast (see the breast model used in Chapters 2 and 3). So for the proposed algorithm, P_x is the only term that can be reasonably used to detect the tumor with y-polarized excitation. Further, the first term of P_x dominates over the second term, again because of the polarization of excitation. Thus the x-component of the received Poynting vector is well-approximated with

$$P_x \approx E_y H_z \tag{4.2}$$

From a similar line of reasoning, an x-polarized excitation signal gives rise to P_y that is well approximated with

$$P_y \approx -E_x H_z \tag{4.3}$$

It has been shown that the phase front of H_z is spherically antisymmetric about the vertical (Y−Z) plane, in which the tumor is located. Therefore, Eqn (4.2) at receiver locations in the positive x direction from the tumor is positive for all time; Eqn (4.2) at receiver locations in the negative x direction from the tumor is negative for all time. This problem is depicted in Figure 4.8 for a receiver in the positive and negative x-direction from a tumor. Since a negative result represents power flow in the negative direction, the total power reflected from a given focal point can be deduced if each receiver in the negative x-direction of the current focal point is multiplied by -1, or

$$P_{xij} = \begin{cases} E_{yi} H_{zj} & x_R > x_F \\ -E_{yi} H_{zj} & x_R < x_F \end{cases} \tag{4.4}$$

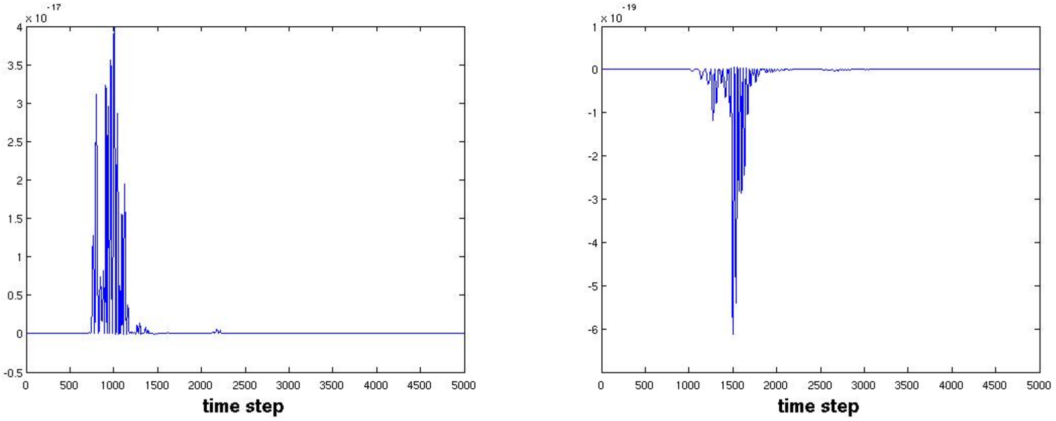

(a) (b)

Figure 4.8: The product of E_y field and H_z field at a given receiver may be either (a) exclusively positive, if the receiver is located in the positive x-direction from a tumor, or (b) exclusively negative if the receiver is located in the negative x-direction from a tumor.

where $i, j = 1 - N$ (N is the total number of receivers), x_R is the x coordinate of the j^{th} receiver and x_F is the x coordinate of the current focal point. At this stage, it is worth noting that the position of each detector has been taken into accout in the proposed algorithm and participates in the intensity computation of each focal point (for DAS, IDAS or DMAS, only the transit time of the signal from the focal point to the detector is considered). Hence, when the x coordinate of the detector lies between the tumor and the current focal-point, the x-directed power obtained from these detectors are entirely inverted. This will further suppress the background noise of the image and improve image quality. Finally, these time-shifted products are summed to yield the power intensity value of the focal point according to

$$
\begin{aligned}
I\left(\overrightarrow{r}\right) = \int_0^T & \left(E_{y1}H^r_{z1} + E_{y1}H^r_{z2} + \cdots + E_{y1}H^r_{zN}\right. \\
& + E_{y2}H^r_{z1} + E_{y2}H^r_{z2} + \cdots + E_{y2}H^r_{zN} \\
& + \vdots \\
& \left. + E_{zN}H^r_{z1} + E_{yN}H^r_{z2} + \cdots + E_{yN}H^r_{zN}\right) dt \\
= \int_0^T & \left[\sum_{i=1}^{N} E_{yi} \cdot \sum_{j=1}^{N} H^r_{zj}\right] dt \\
= \int_0^T & \left(\sum_{i,j=1}^{N} P_{xij}\right) dt \qquad (4.5)
\end{aligned}
$$

where $\overrightarrow{r}$ is the position of the synthetic focal point in 3D Cartesian space, $H^r_{zj} = H_{zj}$ when $x_R > x_F$, $H^r_{zj} = -H_{zj}$ when $x_R < x_F$, and T is the total measurement time. Note that P_{xii} is the actual Poynting vector associated with the i^{th} pixel location; $P_{xij}(i \neq j)$ is a fictitious cross term that contributes to the focal point intensity but has no physical meaning.

Eqn (4.5) clearly illustrates that the number of E field and H field detectors need not be identical, nor must they be collocated. If M is the number of E field detectors and N is the number of H field detectors, then the power intensity is given by

$$
I\left(\overrightarrow{r}\right) = \int_0^T \left[\sum_{i=1}^{M} E_{yi} \cdot \sum_{j=1}^{N} H^r_{zj}\right] dt \qquad (4.6)
$$

Thus E_y and H_z may be processed separately. This observation eases the burden of collecting these field components in a physical measurement since each detecting antenna may be optimized to detect either E_y or H_z, but not necessarily both.

To conclude the formulation, the power intensity of an x-polarized electric excitation signal from Eqn (4.3) is computed as

$$\begin{aligned} I(\overrightarrow{r}) &= \int_0^T \left(\sum_{i,j=1}^{N} P_{yij} \right) dt \\ &= \int_0^T \left[-\sum_{i=1}^{M} E_{xi} \cdot \sum_{j=1}^{N} H_{zj}^{r} \right] dt \end{aligned} \tag{4.7}$$

where, $H_{zj}^{r} = \begin{cases} H_{zj} & y_R > y_F \\ -H_{zj} & y_R < y_F \end{cases}$.

Next, consider a multi-polarized antenna strategy that is discussed in Chapter 3. Since an x-direction polarized transmitter yields an $-E_x H_z$ term, which is essentially the P_y that represents the microwave power flow in the y-direction, the power intensity value of the synthetic focal point should be the summation of values obtained by Eqns (4.5) and (4.7) from 4 illuminations [77],

$$\begin{aligned} I\left(\overrightarrow{r}\right) = \int_0^T \Bigg(& \sum_{i,j=1}^{N} P_{x1}^{ij} + \sum_{i,j=1}^{N} P_{y1}^{ij} \\ & + \sum_{i,j=1}^{N} P_{x2}^{ij} + \sum_{i,j=1}^{N} P_{y2}^{ij} \Bigg) dt \end{aligned} \tag{4.8}$$

Note that the value calculated by Eqn (4.8) is likely negative. When this happens all intensity values are normalized to lie between zero and one.

4.3 The MRI-derived breast phantom and FDTD simulation

An MRI-derived breast phantom is naturally more realistic, but more complex than a simplified breast model. To evaluate the MPI algorithm, three dimensional dielectric and conductivity datasets from MRI measurement are applied in this chapter; these datasets were obtained from the University of Wisconsin MRI numerical breast phantoms repository (UWCEM) [78].

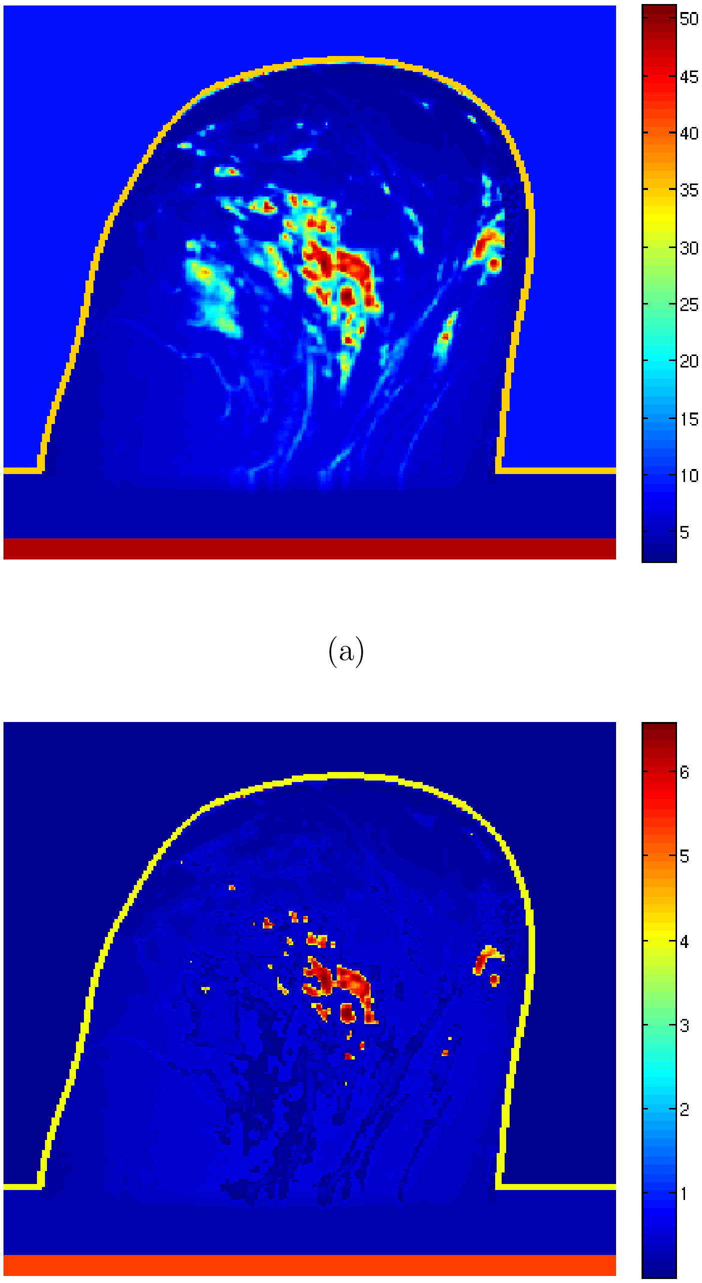

(a)

(b)

Figure 4.9: Distribution of the dielectric properties in a sagittal slice from a 3-D MRI-derived breast phantom. (a) Dielectric constant, (b) conductivity

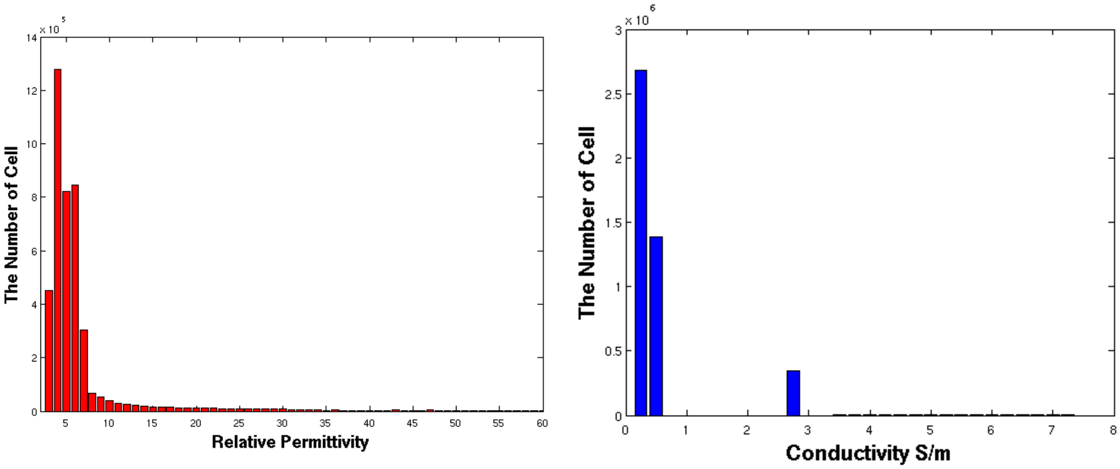

(a) (b)

Figure 4.10: The number of cells corresponding to (a) dielectric constant, and (b) conductivity, within the applied breast phantom.

The selected breast-phantom, including the coupling medium, contains $258 \times 253 \times 251$ grid cells and each cell is $0.5mm \times 0.5mm \times 0.5mm$. Fig. 4.9 shows the distribution of relative permittivity and the conductivity values within the breast phantom. The dielectric properties of the coupling liquid is selected to be $\epsilon_r = 9.2, \sigma = 0$.

Fig. 4.10 displays a statistic for the number of voxels (equivalent to Yee cell in FDTD) associated with the dielectric constant and the conductivity values within the breast shown in Fig. 4.9 (these figures exclude the muscle, skin, or the coupling medium). A voxel that contains more fatty tissue is assummed to have lower dielectric properties, while a voxel that contains more fibroconnective/glandular tissue is assumed to have relatively higher dielectric properties. Fig. 4.10 demonstrates that voxels having relatively low dielectric properties dominate in the breast phantom, which indicates that the content of fat is more than the content of fibroconnective/glandular tissues. As stated in the instruction manual of the UWCEM Repository, this breast phantom contains approximately $25-50\%$ glandular tissue. Therefore, the effective wave velocity in the breast is evaluated, and will be used in a variety of algorithms (DAS, MPI and so on) discussed in this chapter.

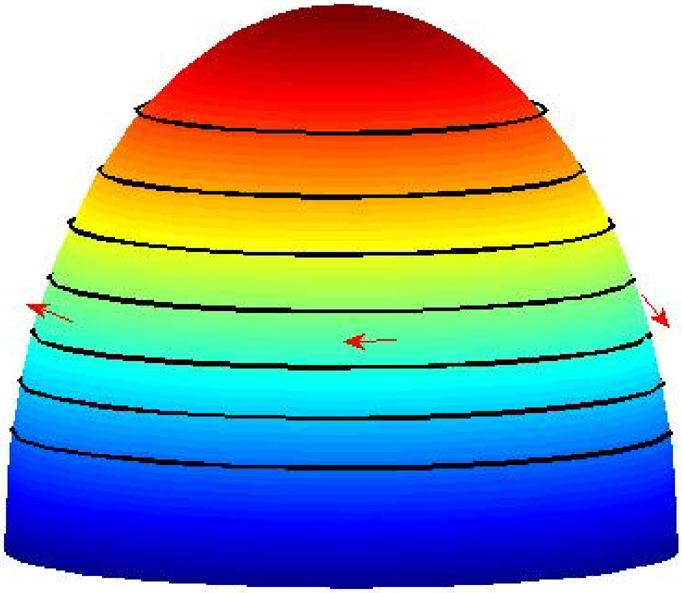

Figure 4.11: 56 receivers lie along 7 circles - each has 8 receivers (receivers not illustrated in this figure). Four transmitters (in red arrows) illuminate the breast successively from different positions, polarized along -x, +y, +x and -y respectively.

We assume that an effective wave speed can always be defined to work for a certain range of the density level (4 density levels are classified in UWCEM Repository according to the breast density), due to the robustness of the DAS-family algorithm in near-field microwave imaging [75]. However, the more dense the breast, the lower contrast is obtained in the reconstructed image.

A synthetic aperture array shown in Fig. 4.11, which has 7 layers and each layer has 8 elements (along the black circles, specific elements are not shown in this figure), is applied to detect a spherical breast tumor centered at (78,75,50) with 8mm diameter in the breast phantom. These receivers are assumed to be on the surface of the skin, which is about 1.5mm thick and clearly demarcates the breast tissue and the coupling medium in Fig. 4.9. Four transmitters (marked by arrows in Fig. 4.11, this figure only shows 3 of them) take turns sending out a UWB signal (a modulated Gaussian pulse described in Eqn. (3.4), the spectrum of this signal is displayed in Fig. 3.7) after a previous transmission and backscattered-signal collection.

To carry out the MPI algorithm, we need to calculate the Poynting vector at a specific point in the 3-D space. Assuming that these points are located in the center of each Yee cell (take Fig. 2.1 as reference), then, the electric field signal requires four point averaging and the H field signal requires two-point averaging:

$$\begin{aligned}
E_x =& \frac{1}{4}\left[E_x\left(i+\frac{1}{2},j,k\right)+E_x\left(i+\frac{1}{2},j+1,k\right)\right.\\
&\left.+E_x\left(i+\frac{1}{2},j,k+1\right)+E_x\left(i+\frac{1}{2},j+1,k+1\right)\right] \qquad (4.9)\\
E_y =& \frac{1}{4}\left[E_y\left(i,j+\frac{1}{2},k\right)+E_y\left(i+1,j+\frac{1}{2},k\right)\right.\\
&\left.+E_y\left(i,j+\frac{1}{2},k+1\right)+E_y\left(i+1,j+\frac{1}{2},k+1\right)\right] \qquad (4.10)\\
E_z =& \frac{1}{4}\left[E_z\left(i,j,k+\frac{1}{2}\right)+E_z\left(i+1,j,k+\frac{1}{2}\right)\right.\\
&\left.+E_z\left(i+1,j+1,k+\frac{1}{2}\right)+E_z\left(i,j+1,k+\frac{1}{2}\right)\right] \qquad (4.11)\\
H_x =& \frac{1}{2}\left[H_x\left(i,j+\frac{1}{2},k+\frac{1}{2}\right)+H_x\left(i+1,j+\frac{1}{2},k+\frac{1}{2}\right)\right] \qquad (4.12)\\
H_y =& \frac{1}{2}\left[H_y\left(i+\frac{1}{2},j,k+\frac{1}{2}\right)+H_y\left(i+\frac{1}{2},j+1,k+\frac{1}{2}\right)\right] \qquad (4.13)\\
H_z =& \frac{1}{2}\left[H_z\left(i+\frac{1}{2},j+\frac{1}{2},k\right)+H_z\left(i+\frac{1}{2},j+\frac{1}{2},k+1\right)\right] \qquad (4.14)
\end{aligned}$$

The computational space is again terminated with a second-order Liao absorbing boundary. Since the grid size is reduced in the MRI-derived breast phantom, to make the FDTD simulation stable, our computation time-step is readjusted to $\Delta t = 4/3ps$ and the total number of computation steps are adjusted to 5000 steps. Four transmissions, with respective polarization, as well as the backscattered signals collected by the antenna array, take approximately 6 hours by serial fortran code on state of the art linux servers. Thus, a total of 4 × 56 (N=56, the number of receivers) series of data are obtained from the 3-D FDTD simulation.

4.4 Imaging results using the MRI-derived breast phantom

4.4.1 Single tumor

The calibration step is conducted by subtracting a reference model which is ±10% random variation in dielectric properties from the tumor-bearing model. The calibrated sginals are imported into our matlab-based multi-polarized-MPI beamformer (parallel processing on multicore is involved) to yield a reconstructed image. A sliced image for horizontal, coronal, or sagittal reconstruction takes approximately 3 minutes, which again shows the efficiency of the MPI algorithm.

Fig. 4.12 illustrates the reconstructed image obtained through the multi-polarized MPI approach in (a) x-y plane, (b) z-y plane, and (c) z-x plane, in which the tumor is located. The dark dot, which represents the tumor location, can be easily recognized from these images. And its location is consistent with the actual location in the FDTD simulation. The reconstructed images show a good contrast against the clutters and the background. Fig. 4.13 and Fig. 4.14 illustrate the image obtained by multi-polarized DMAS and multi-polarized DAS respectively, with the same antenna strategy, to compare with the result obtained by MPI. In the DMAS algorithm, the backscattered signals received from the numerical breast phantom are time shifted, multiplied in pair, and the products are summed to form a synthetic focal point [39]. Fig. 4.13 has a large number of clutters, while Fig. 4.14 has very poor image contrast.

To quantify further the performance of the three approaches, quantitative assessments are carried out in terms of signal-to-clutter ratio (SCR) and signal-to-mean ratio (SMR). SCR compares the maximum tumor response with the maximum clutter response in the same image, whereas SMR compares the maximum tumor response with the mean response of the same image. The SCR and SMR for Fig.

4.12 − 4.14 are shown in Table 4.1. For all views, the SMR and SCR values for MPI is the highest among the three.

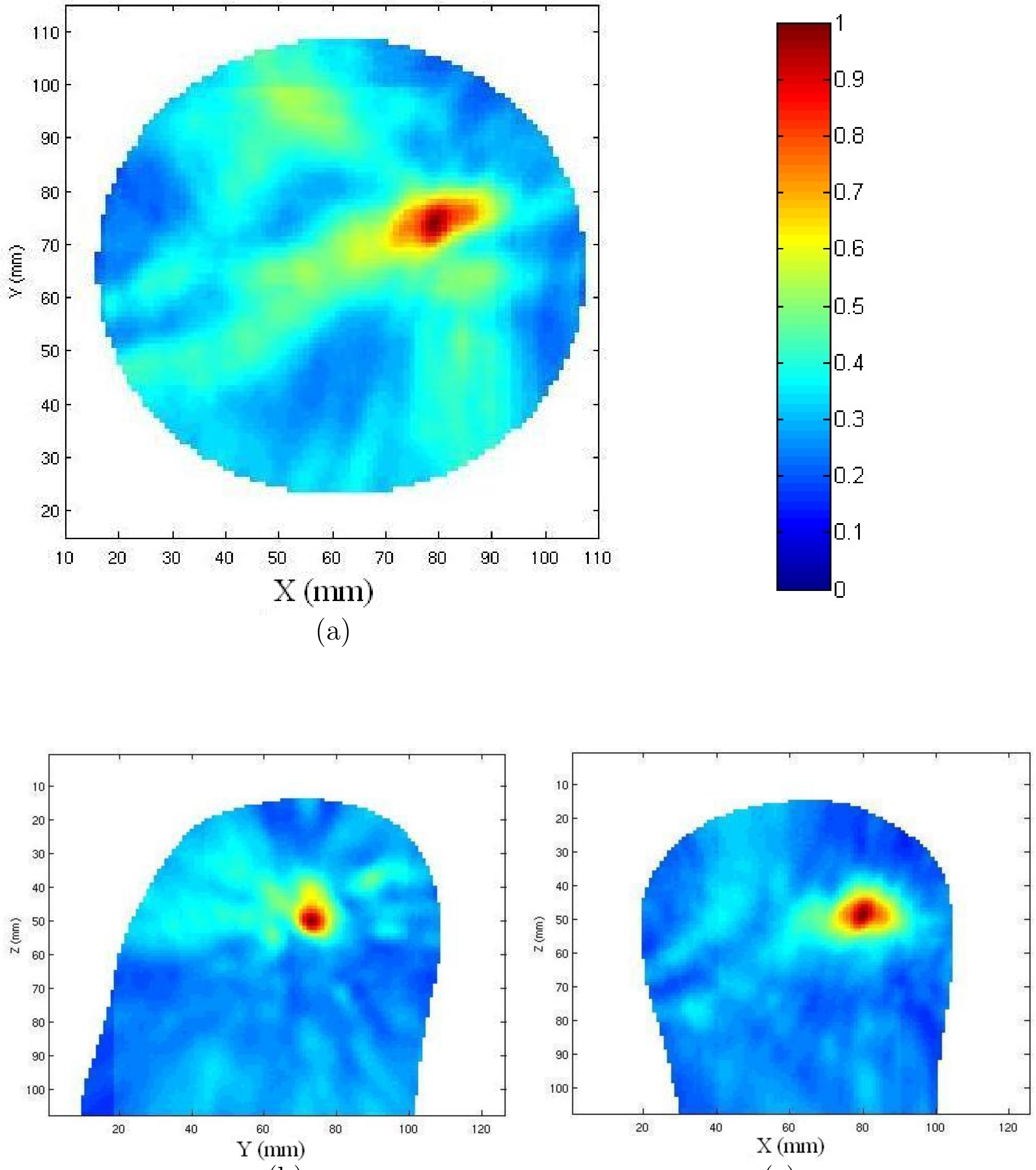

(a)

(b)

(c)

Figure 4.12: The reconstructed image through multi-polarized MPI method. (a) horizontal plane z=50; (b) coronal plane x=78; (c) sagittal plane y=75.

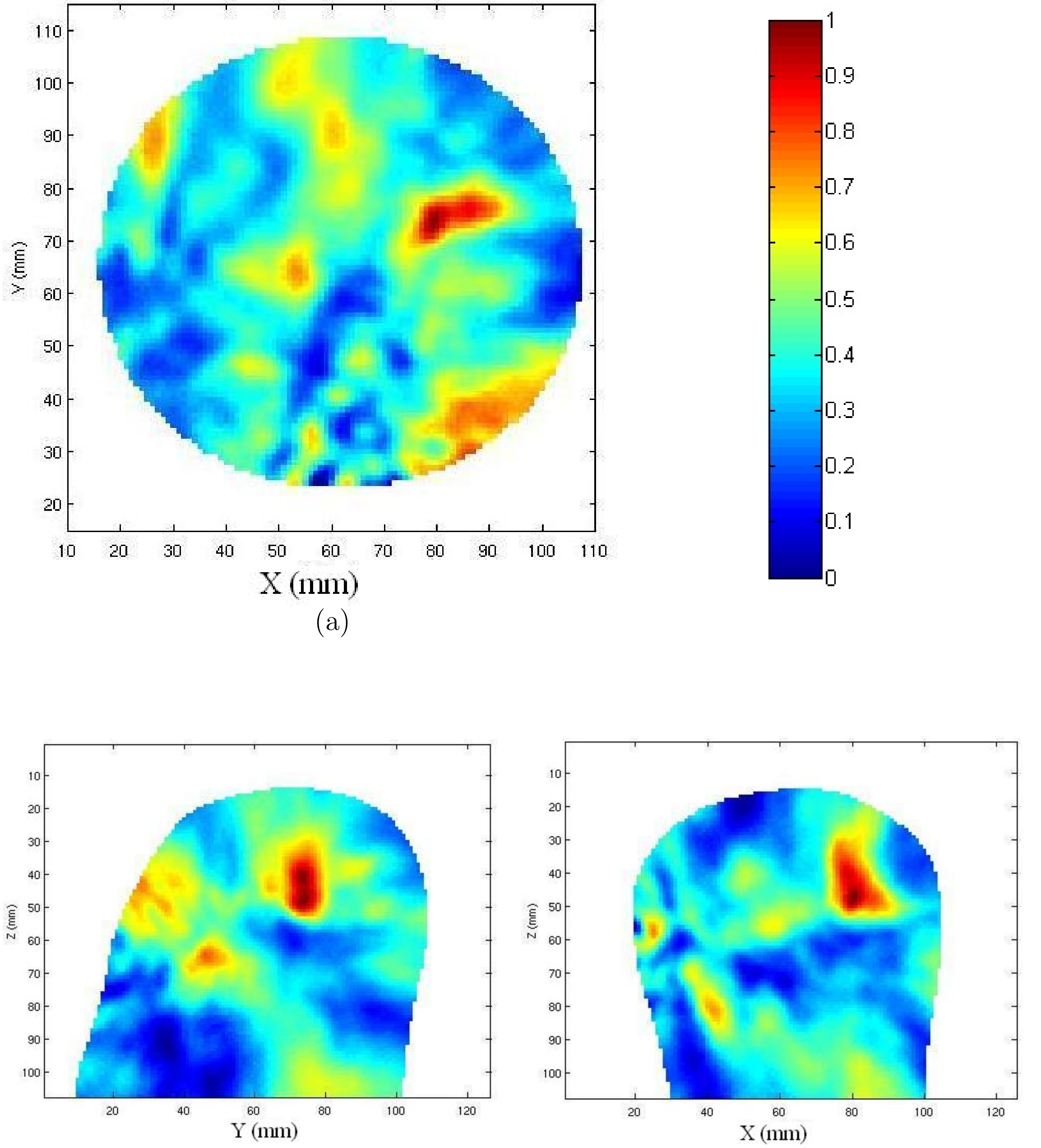

(a)

(b)

(c)

Figure 4.13: The reconstructed image through multi-polarized DMAS method. (a) horizontal plane z=50; (b) coronal plane x=78; (c) sagittal plane y=75.

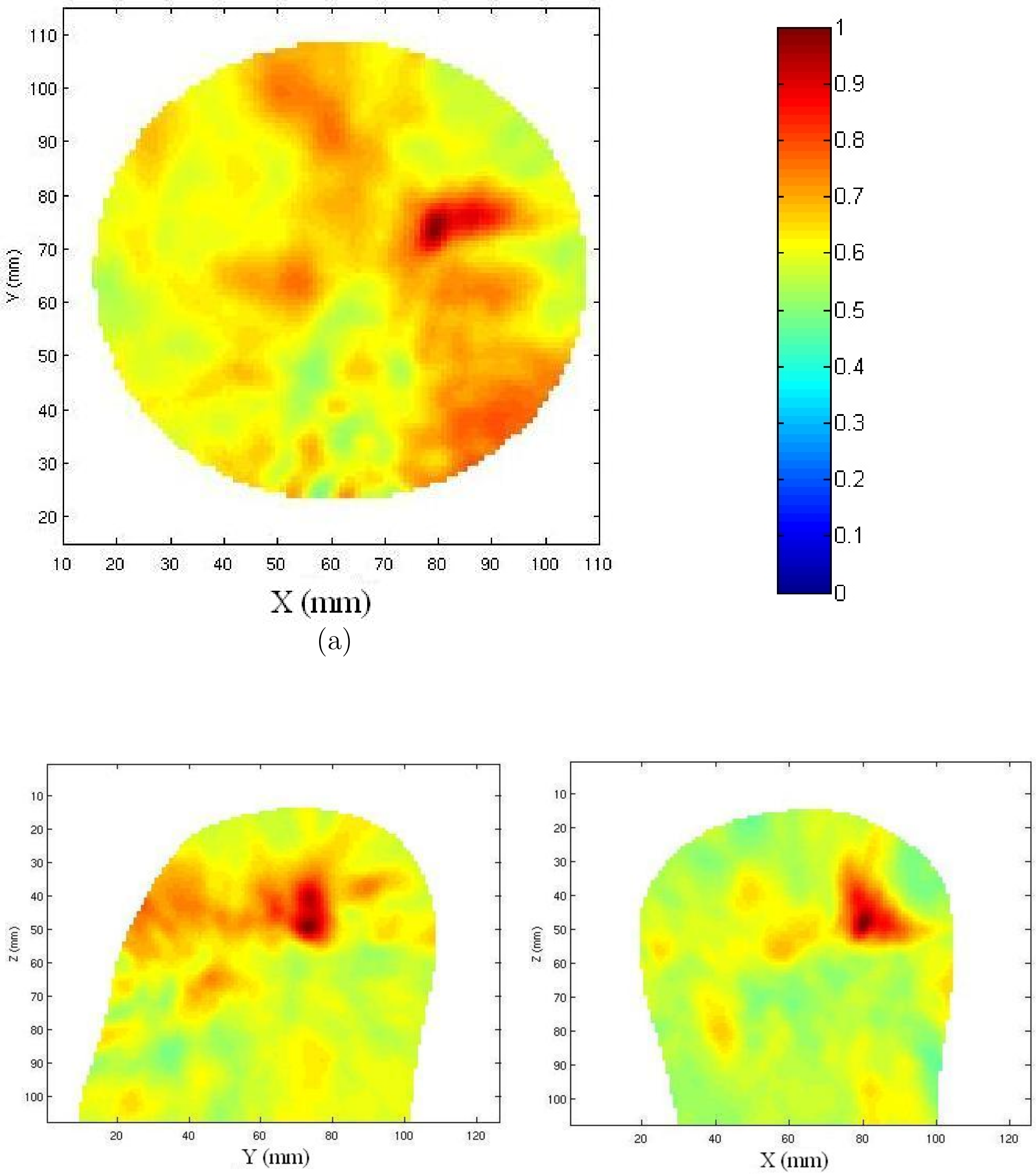

(a)

(b)

(c)

Figure 4.14: The reconstructed image through multi-polarized DAS method. (a) horizontal plane z=50; (b) coronal plane x=78; (c) sagittal plane y=75.

Table 4.1: Comparison of SMR and SCR value for Fig. 4.12, 4.13, and 4.14

Fig number	Method	SMR (dB)	SCR (dB)
Fig 4.12(a)	MPI	5.311	2.001
Fig 4.13(a)	DMAS	3.936	1.098
Fig 4.14(a)	DAS	1.919	0.999
Fig 4.12(b)	MPI	5.343	3.280
Fig 4.13(b)	DMAS	4.187	0.067
Fig 4.14(b)	DAS	2.375	1.650
Fig 4.12(c)	MPI	5.680	1.768
Fig 4.13(c)	DMAS	4.435	1.327
Fig 4.14(c)	DAS	2.099	0.285

Considering that a relatively long interval from previous tomography examination may occur, the reference breast phantom for the data calibration step may have considerable differences from the tumor-contained phantom. Fig. 4.15 shows the reconstructed image using multi-polarized MPI when the tumor-contained breast phantom and the tumor-free breast phantom have ±15% difference in dielectric parameters. The image quality is significantly degraded over the ±10% case though the tumor is still able to be recognized centered at (78,45,60). Neither DAS nor DMAS is able to locate the target in this scenario.

4.4.2 Dual tumor

Again, the dual tumor case is investigated to study the imaging resolution in this numerical breast phantom, via the MPI algorithm. In this section, we study both the horizontal and vertical imaging resolution of the multi-polarized MPI as an illustration of the detection and imaging of a spherical pair of tumors, each of $6mm$ diameter, using the MRI-derived breast phantom and the antenna scheme depicted in Fig. 4.11 . The breast phantoms with and without tumors differ with ±10% random variation.

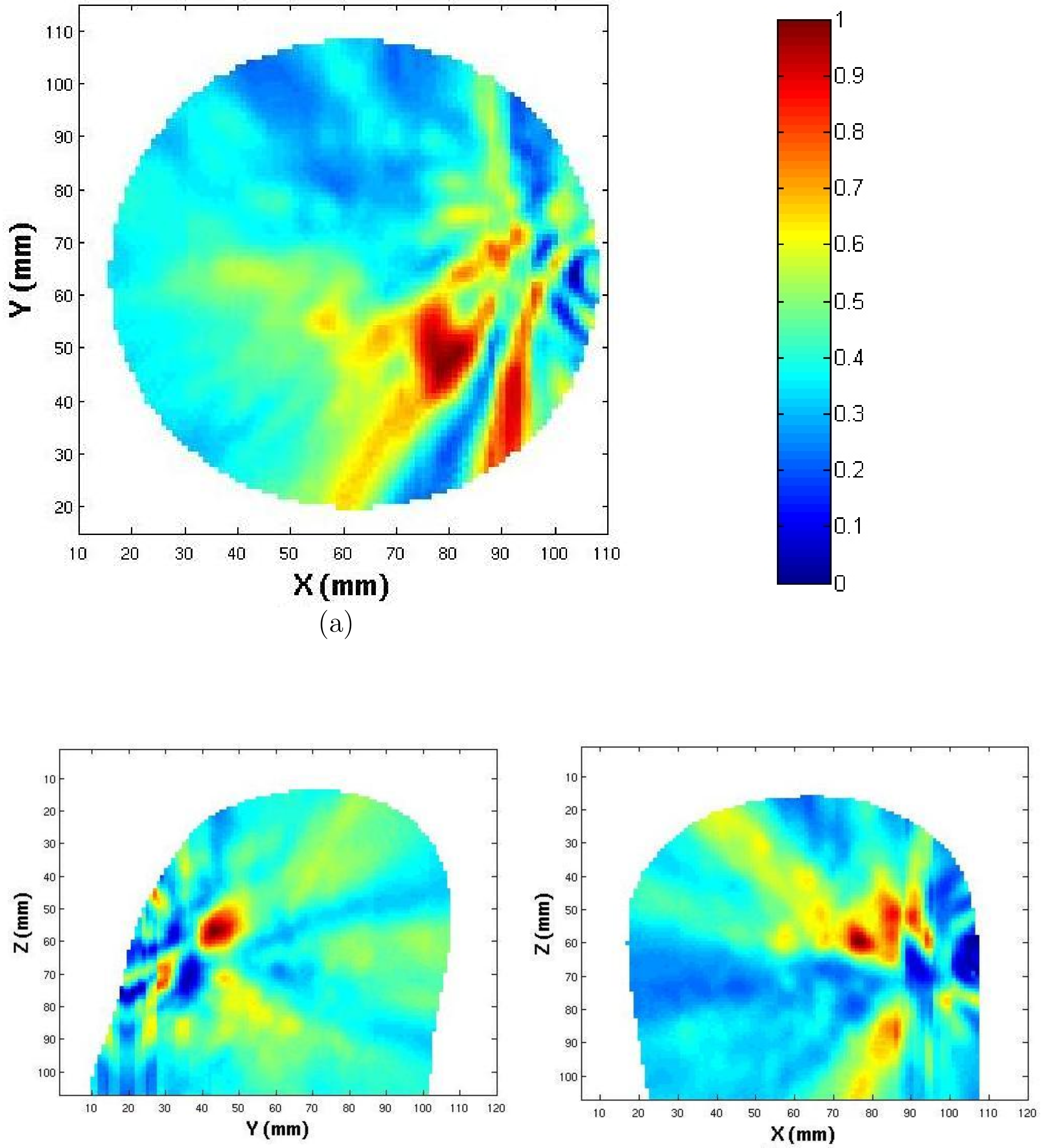

(a)

(b)

(c)

Figure 4.15: Reconstructed image for tumor centered at (78,45,60) with 8mm diameter using MPI. Tumor-contained breast phantom and the tumor-free breast phantom are ±15% randomly different in dielectric parameters. (a) in the x-y plane, (b) in the z-y plane, and (c) in the z-x plane.

The horizontal plane resolution is determined by analyzing the distance between two identical targets placed in the center of the x-y plane. Fig. 4.16(a) shows the

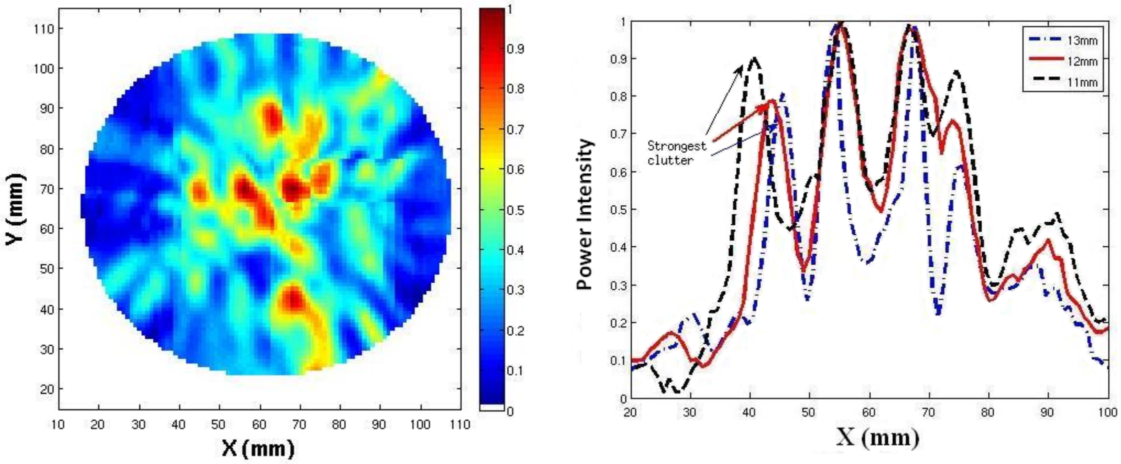

(a) (b)

Figure 4.16: Two-tumor prototype for study of horizontal resolution. (a) is the reconstructed image when two tumors are 12*mm* apart. Center positions are (56,70,50) and (68,70,50). (b) shows the intensity along the line y=70 in the plane of z=50 when two tumors are 11*mm*, 12*mm*, and 13*mm* apart.

reconstructed image when two targets are centered at (56,70,50) and (68,70,50), a 12*mm* offset. It is difficult to identify the tumors in this image since clutters are very strong. Fig.4.16(b) illustrates the intensity of the focal points along the line y=70 in the reconstructed plane when two tumors are 11*mm*, 12*mm*, or 13*mm* apart. This figure demonstrates that the resolution of the proposed reconstruction approach is near 12*mm* in the horizontal plane. This translates to approximately 0.7λ at the peak-spectrum frequency, and approximately 0.112λ at the lower edge frequency (1GHz) of the UWB signal in the coupling medium. Fig. 4.16 also implies that clutters in the 11*mm*-apart case (black dash line) would be even stronger than the 12*mm*-apart and 13*mm*-apart case.

Similarly, the vertical resolution is studied by varying the distance between two identical tumors, placed in the z-y plane. Fig. 4.17(a) shows the reconstructed image when two 6*mm*-diameter tumors centered at (75,75,59) and (75,75,63). Hence the center distance is 14*mm*. Clutters are observed to be strong in the image, however two tumors can be clearly identified and distinguished. Fig.4.17(b) illustrates the

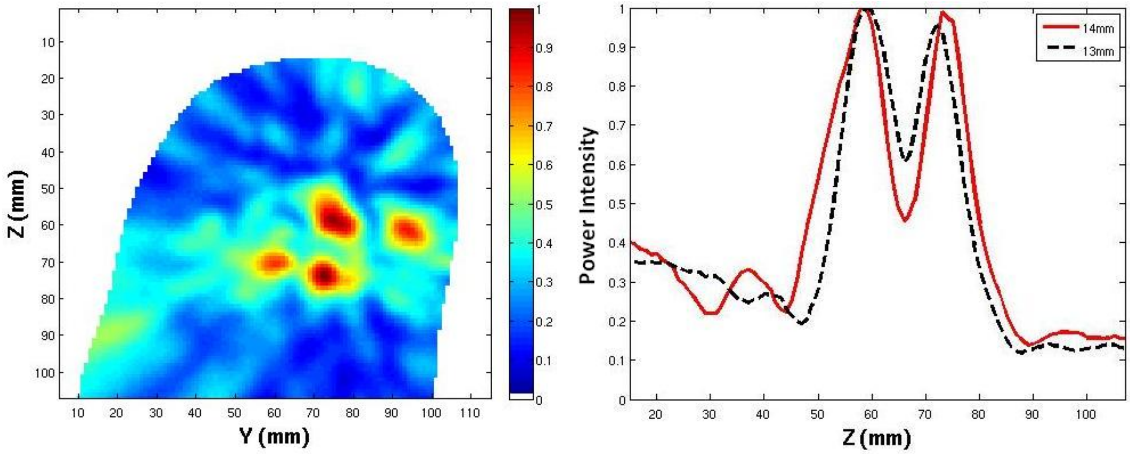

(a) (b)

Figure 4.17: Two-tumor prototype for study of vertical resolution. (a) is the reconstructed image when two tumors are 14*mm* apart. Center positions are (75,75,59) and (75,75,73). (b) shows the intensity along the line y=75 in the z-y plane of x=75 when two tumors are 13*mm*, and 14*mm* apart.

intensity of the focal points along the line y=75 in the reconstructed plane when two tumors are 13*mm* or 14*mm* apart. This figure demonstrates that at a distance of 14*mm*, two tumors are able to be distinguished. This is equivalent to approximately 0.82λ at the peak-spectrum frequency of the UWB detecting signal and 0.131λ at 1GHz in the coupling medium.

CHAPTER 5: UWB ANTENNA DESIGN AND FABRICATION

A UWB system must have UWB antennas, which plays an important role in broad band communication and imaging systems. The antenna desired for microwave medical imaging, especially breast cancer imaging, must satisfy strict requirements of bandwidth, pulse waveform, radiation pattern, and antenna size (small antennas are prefered). The reasons are: for real synthetic aperture arrays, there must be several antennas around the breast with reasonable spacings; For non-real aperture arrays, an antenna is moved accross the breast to collect signals at several location, while big antennas may have accuracy problem in moving, which subsequently affects the quality of beamforming. Therefore, a large number of investigations in small UWB antennas have been carried out to design medical-application-aimed antennas.

In 2003, Li et. al. proposed a pyramidal horn antenna for breast cancer detection, which works in the 1-11 GHz spectrum [79]. In Li's experiment, this antenna serves as a transmitter and a receiver. It is moved across the breast to create a synthetic aperture array. As compared to the antenna built by Li, microstrip antennas have a more compact "2-D" form, but ususally with narrow bandwidth. However, the Vivaldi antenna [80] has recently received considerable attention because of its "2-D" structure and broad band property. The antipodal Vivaldi antenna, having an even simpler structure than conventional Vivaldi which makes it easy to design and fabricate, has been employed in many communication applications [81]− [91].

However, only a few studies about medical-imaging-aimed microstrip antennas (Vivaldi or other types [92] [93]) have been reported. Among them, it is worth noting Bourqui et. al.'s work [94], in which a balanced antipodal Vivaldi was built for breast cancer detection, accompanied with a director ahead of the antenna. The structure of this antenna was coded in FDTD to simulate the whole process of transmitting and receiving signals from a breast phantom. Good imaging results were obtained using data collected by this antenna through FDTD simulation. The problem in this design, is that the antenna is still quite large ($80 \times 44 \times 9.2mm$, with the director included). It is impossible to use this antenna to build a real synthetic aperture array for microwave breast cancer imaging because of its size. Therefore, in this chapter, we propose two antipodal Vivaldi antennas - each quite small - and finally fabricate an antenna array using one of which, for the application of breast cancer detection [95].

5.1 Two antipolar Vivaldi antennas

The proposed Vivaldi antennas have exponential structures. Fig. 5.1 and Fig. 5.2 present the geometry and parameter values of the proposed Vivaldi antennas. The curvatures of the outer curve and the inner curve (inner curves form the gap) follow the equation

$$x_{in} = c_1 \left[e^{c_2 (y-L-C)} - 1 \right] - W \tag{5.1}$$

$$x_{out} = W \left(2e^{\frac{y-L-C}{6}} - 1 \right) \tag{5.2}$$

where W, L, and C are shown in Fig. 5.1(a) and Fig. 5.2(a). The coefficients c_1 and c_2 for our antennas are listed in Table 5.1.

Table 5.1: The coefficients used in Eqn 5.1.

Coeffficient	Antenna #1 in Fig. 5.1	Antenna #2 in Fig. 5.2
c1	0.25	0.06
c2	0.15	0.2

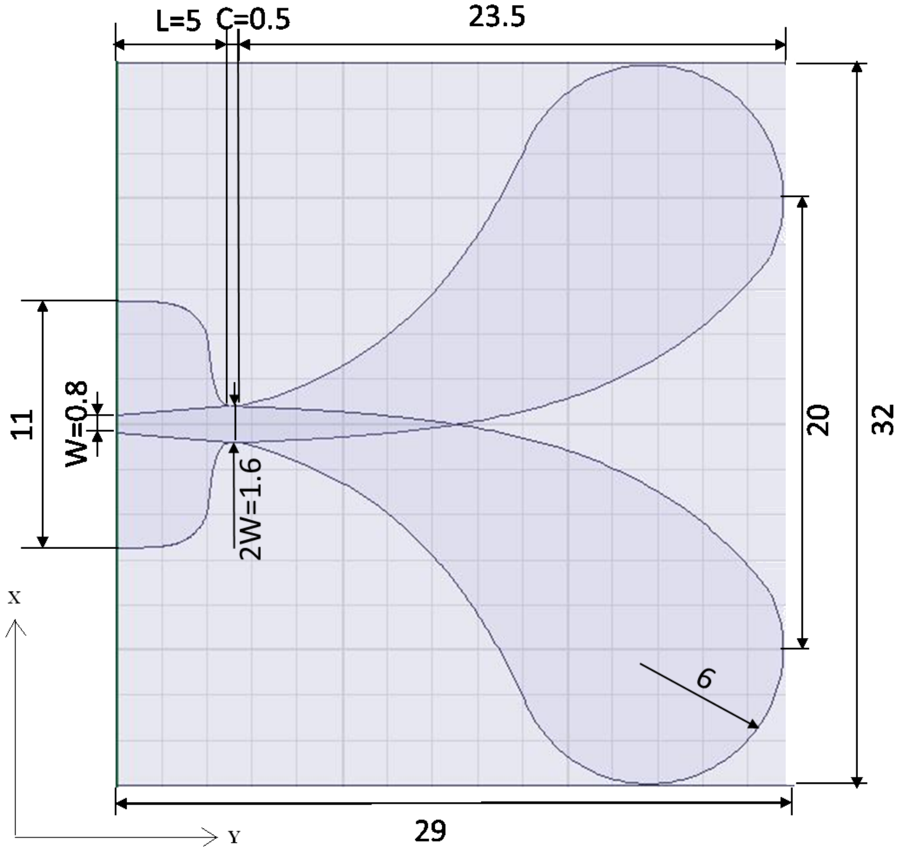

(a)

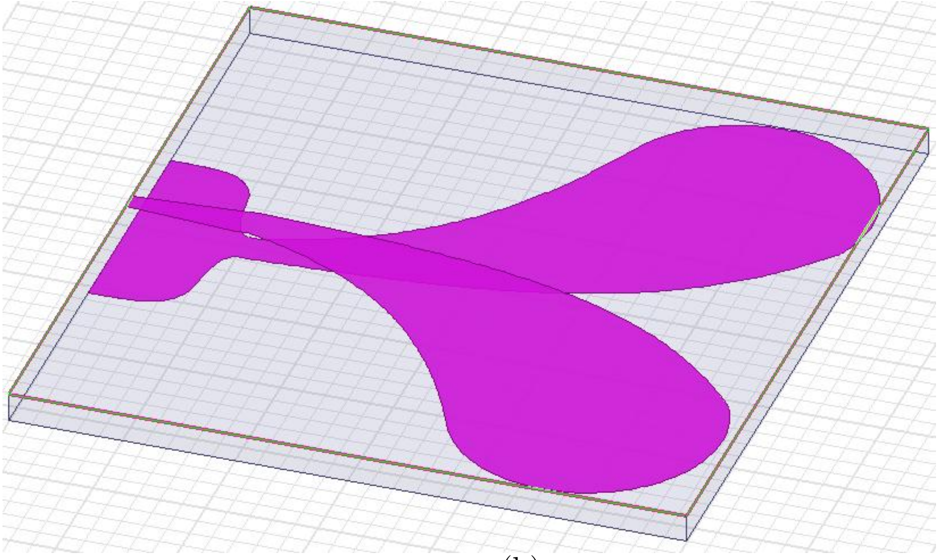

(b)

Figure 5.1: Geometry and parameters of a proposed Vivaldi antenna (Antenna #1) copper pattern. (a) top view, (b) 3-D view. Unit : mm.

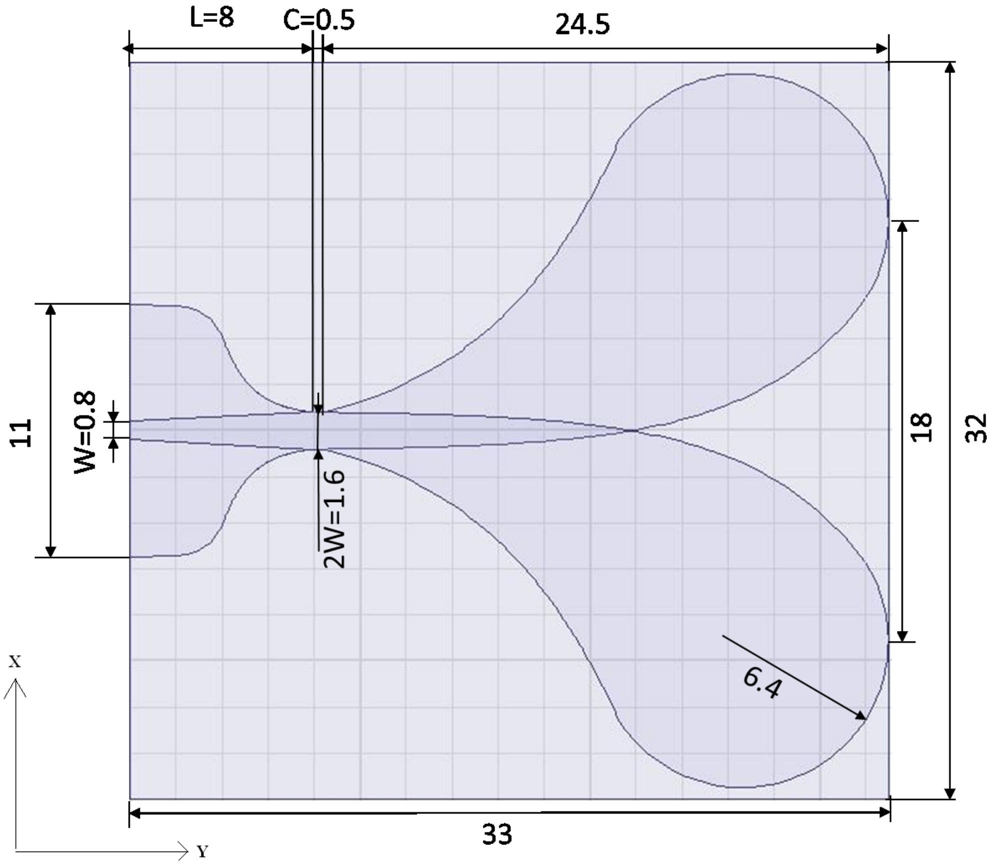

(a)

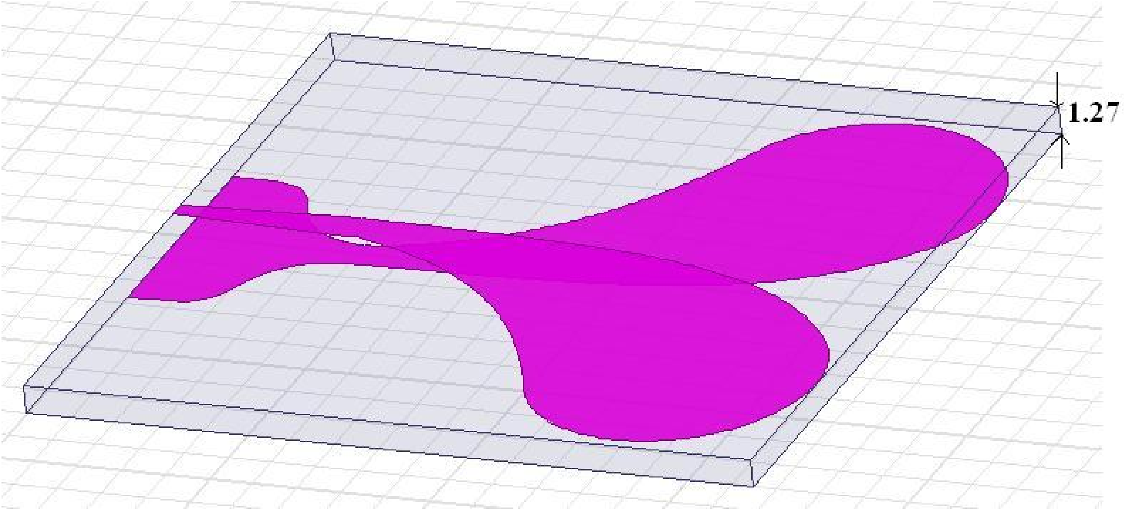

(b)

Figure 5.2: Geometry and parameters of a second Vivaldi antenna (Antenna #2) copper pattern. (a) top view, (b) 3-D view. Unit: mm.

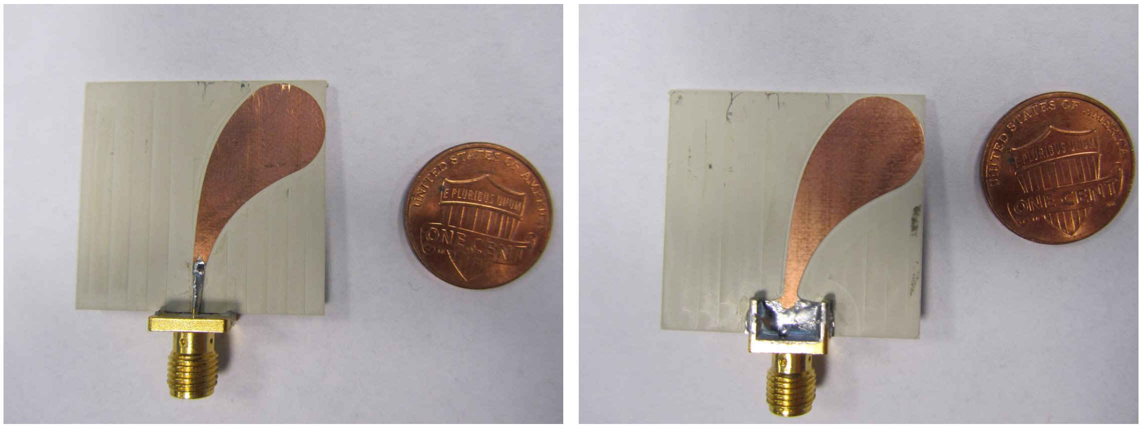

(a) (b)

Figure 5.3: The constructed Vivaldi antenna #1. (a) top view, (b) bottom view.

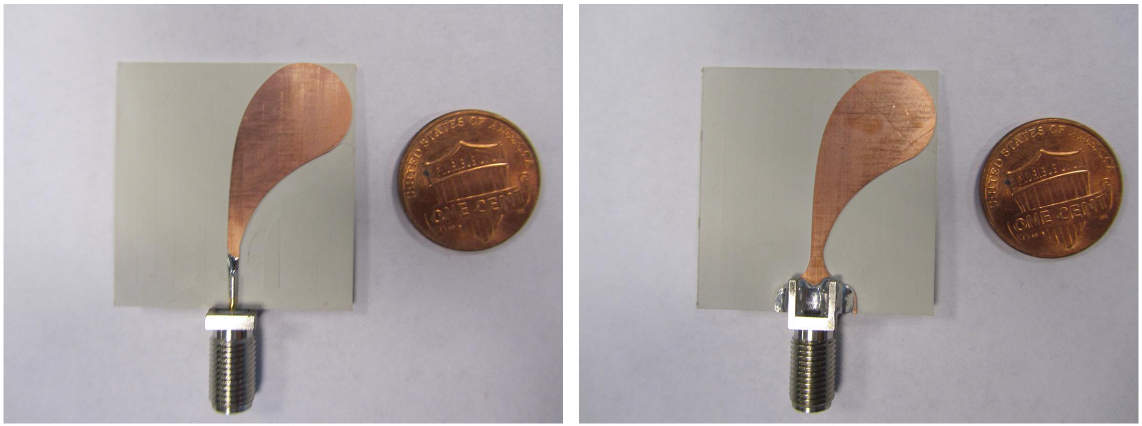

(a) (b)

Figure 5.4: The constructed Vivaldi antenna #2. (a) top view, (b) bottom view.

In both designs, the copper layer is terminated with a tilted half disc, to reduce the reflection from the end. The antenna is assumed to be fed through an SMA connector followed by a gradual transition from microstrip to parallel strips transmission line. Along the transition, the conductor width increases linearly while the ground width decreases exponentially to retain a constant impedance. The tri-strip-like transmission line extends for a short distance before the grounds and conductor start to flare in opposite directions with exponential curves to create the antenna aperture.

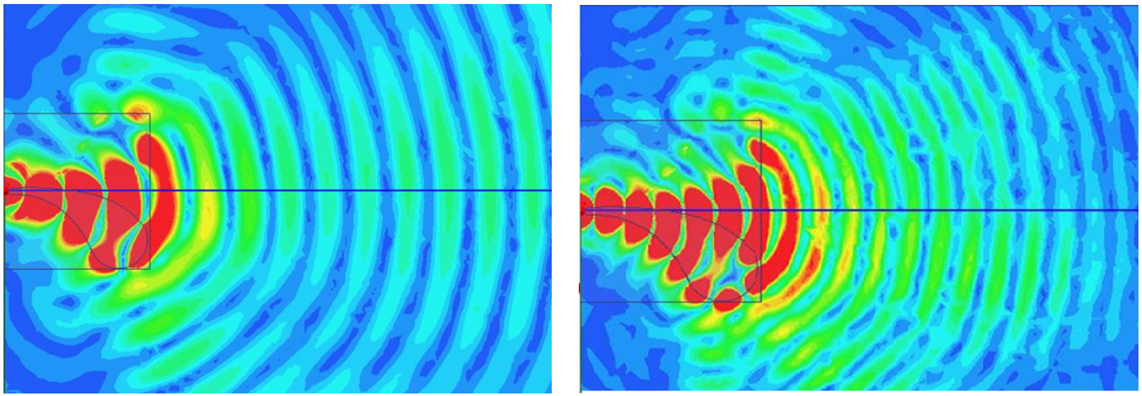
(a) (b)

Figure 5.5: The 2-D Electric field of Antenna #1 in the x-y plane when the frequency is (a) 6 GHz, (b) 10 GHz.

The substrate is constructed using TMM 10 (Rogers Corporation) that has a relative permittivity of 9.2, and thickness 1.27 mm. The second antenna (Fig. 5.2) has a longer feeding leg and a reduced gap, compared to Antenna #1 (Fig. 5.1). The overall sizes of Antenna #1 and Antenna #2 are $29 \times 32 \times 1.27mm$, and $33 \times 32 \times 1.27mm$, respectively. The constructed antennas are shown in Fig. 5.3 and 5.4.

The antennas used for breast cancer imaging, as disscussed in the previous chapter, are assumed to be immersed in a coupling medium when operating in both transmit and receive mode. Fig. 5.5 shows the HFSS-simulated Electric field on the x-y plane, generated by Antenna #1 when it is centered in the x-y plane, fed from the origin, and immersed in an ideal coupling liquid with relative permittivity of 9.2. The image indicates a good radiation in the near field by this antenna. In the antenna measurement, we used a commercial automotive fuel named E85 as the coupling liquid, which contains 85% ethonal, plus gasoline. Fig. 5.6 shows the HFSS-simulated and measured reflection coefficient S_{11} over the freuqency span 1 GHz − 10 GHz. The measurement matches the main features of the simulation especially in the low frequency range. The main source of error comes from the real dieletric properties of the coupling liquid do not quite match the parameters used in our simulation.

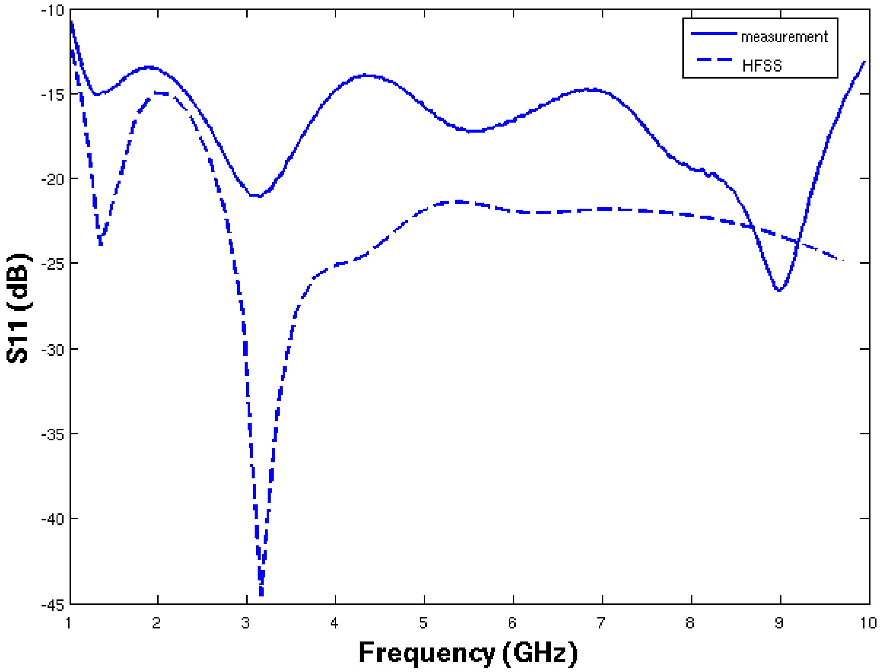

Figure 5.6: The measured (solid line) and HFSS-simulated (dashed line) S_{11} for antenna #1.

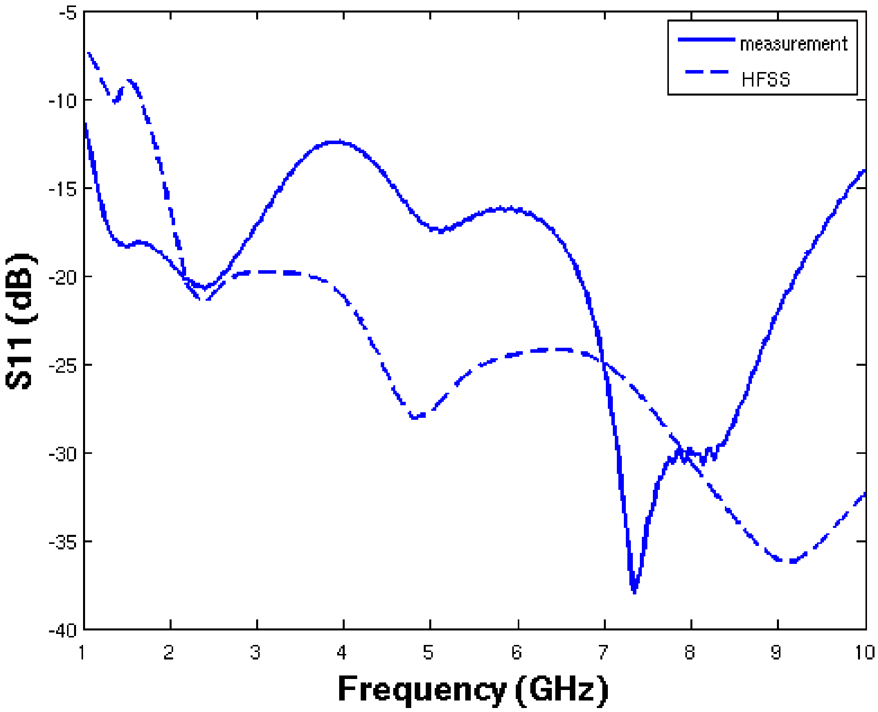

Figure 5.7: The measured (solid line) and HFSS-simulated (dashed line) S_{11} for antenna #2.

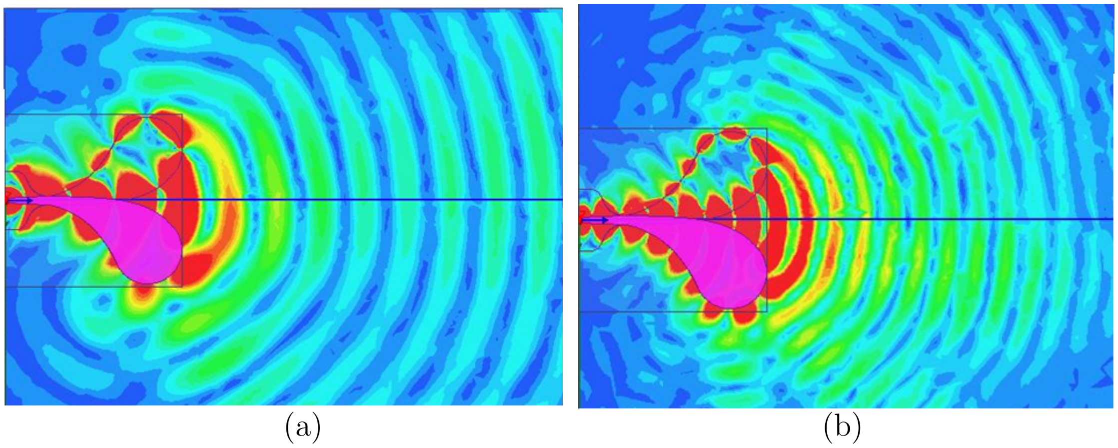
(a) (b)

Figure 5.8: The 2-D Electric field of Antenna #2 in the x-y plane when the frequency is (a) 6 GHz, (b) 10 GHz.

The same measurement is conducted for Antenna #2. We find that the field generated by Antenna #2 does not present significantly different fields than those generated by Antenna # 1, from HFSS simulation. Its measured and simulated S_{11} are illustrated in Fig. 5.7.

5.2 The antenna array

We selected Antenna #1 as the antenna element employed in the antenna array because it is relatively small. As shown in Fig. 5.9, eight antennas were built on one substrate and have the same polarization. This arrangement makes the antennas easy to feed. The hole in the middle allowing for measurement of a breast, is $100mm$ in diameter. By moving the array up and down in the z-direction, the array can collect the siganl from the breast at different heights, shown in Fig. 5.10 (7 levels are applied in the method discussed in Chapter 4), to conform to synthetic aperture imaging. Since the array aperture is fixed, the antennas are comparatively far from the surface of the breast as they move up, if the breast is still assumed to be hemispherical.

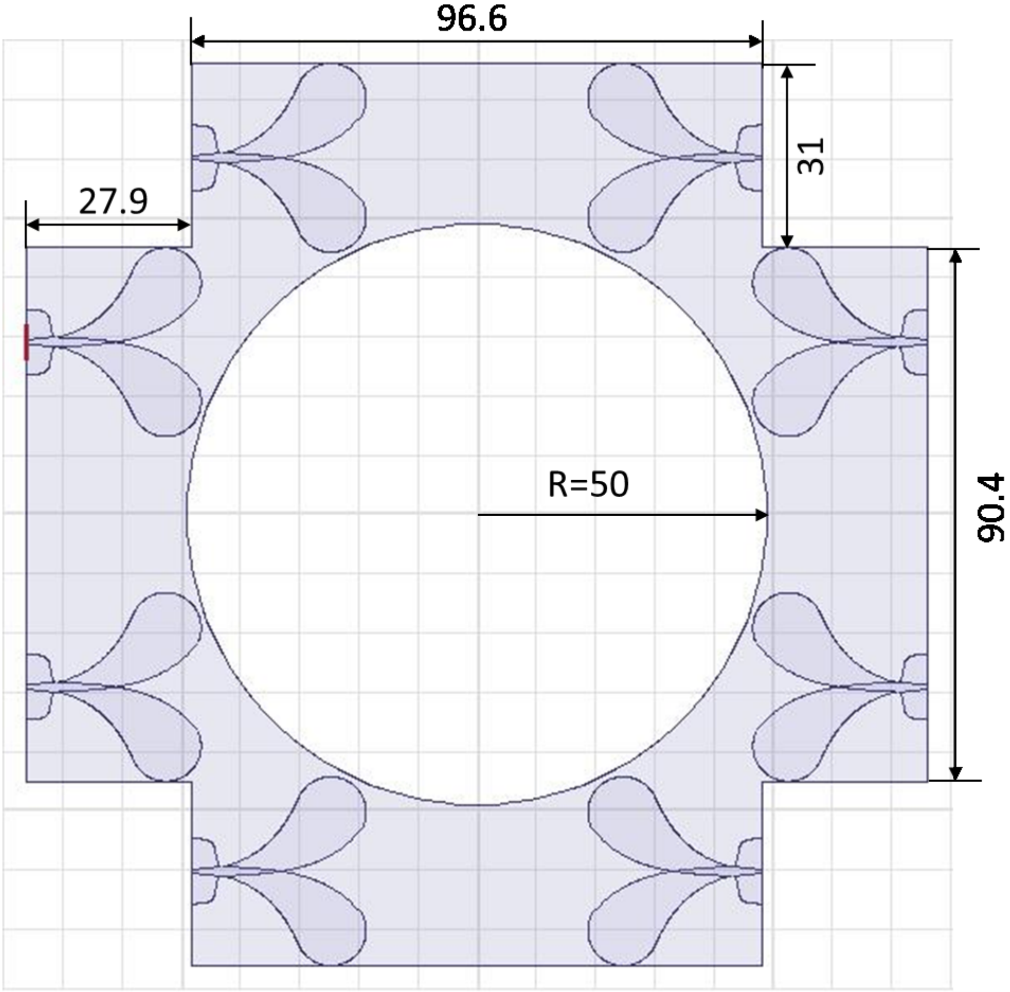

Figure 5.9: The designed antenna array in HFSS. Unit: mm.

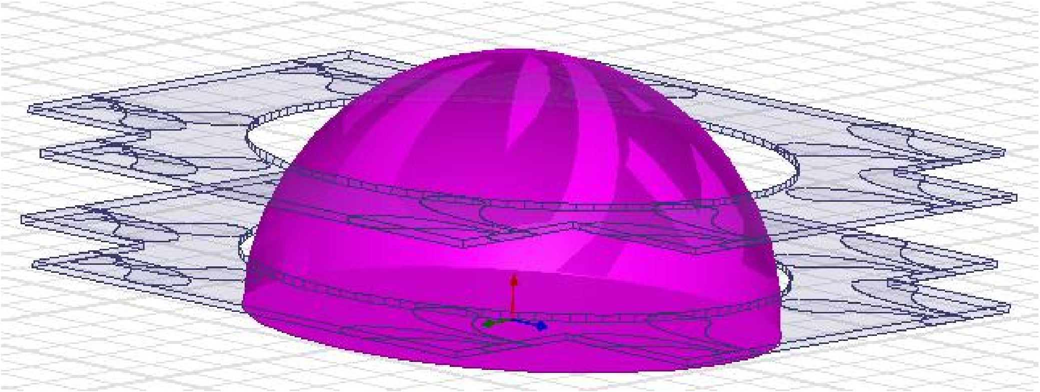

Figure 5.10: The designed antenna array for breast cancer imaging.

The constructed antenna array with the SMA connector is shown in Fig. 5.11. The multi-polarized approach, discussed in the previous chapter, can be conducted by turning the array 90 degrees - then all the antennas would have vertical polarization corresponding to their former polarization. The overall size of the array is $152.4 \times 152.4 \times 1.27 mm$. The material of the substrate still is Rogers TMM 10 (relatively permittivity 9.2).

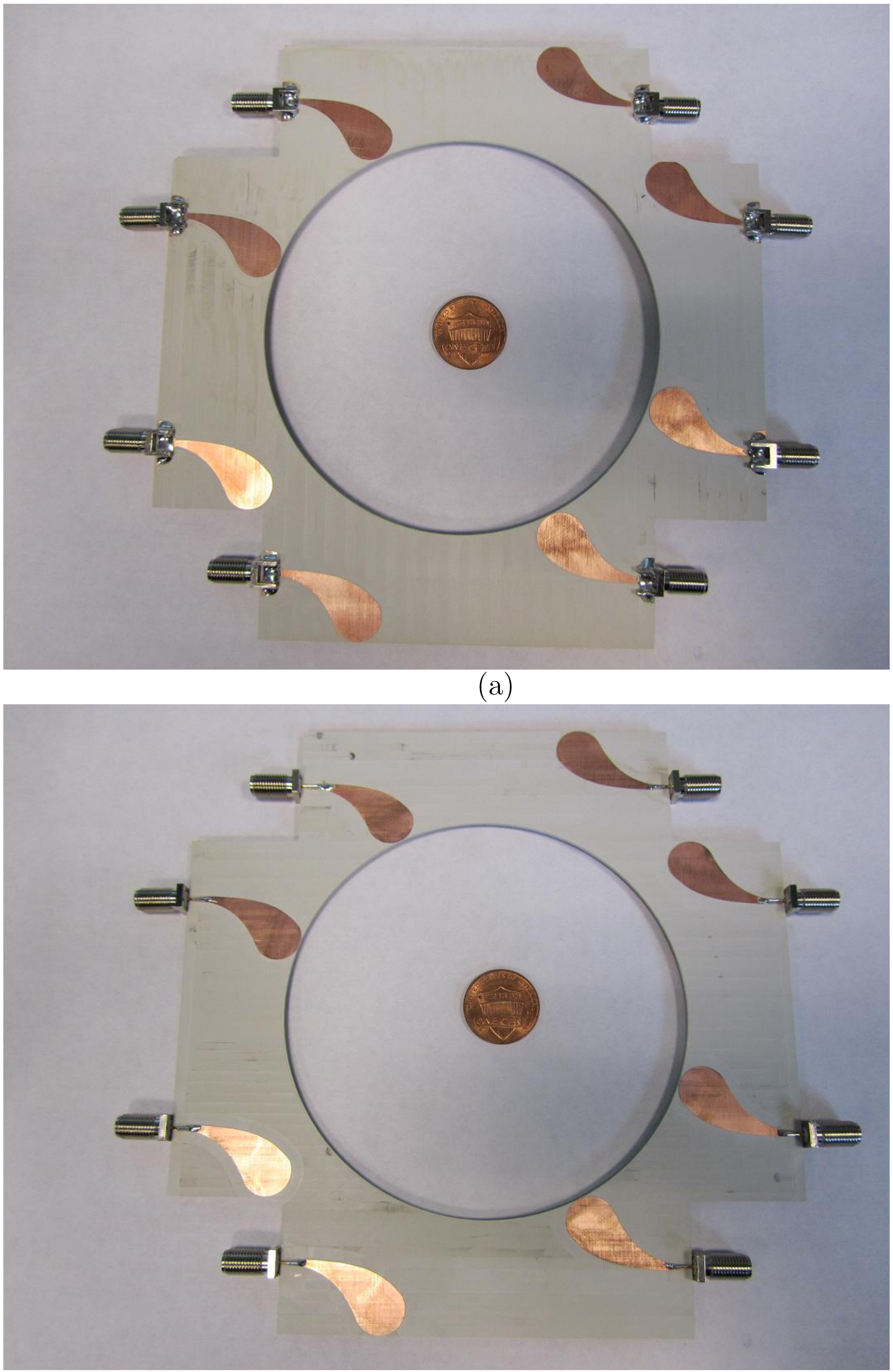

(a)

(b)

Figure 5.11: The constructed antenna array.(a) top view, (b) bottom view.

CHAPTER 6: CONCLUSIONS

This dissertation presents a study of an ultrawideband microwave imaging system for the detection of ealy-stage breast cancer. Our ongoing work in this research is motivated by the clinical need for a viable complement to, or replacement for X-ray mammography, which suffers from a number of disadvantages. The physical basis for breast cancer detection via microwave method is the contrast in dielectric properties of healthy and malignant breast tissues. In our investigated multi-polarized detection system, an ultrawideband signal is transmitted by vertically-polarized linear sources sequentially, and an array of antennas is located near the surface of the breast to collect backscattered signals from the breast. The received signals are processed using artifact removal and MPI beamforming algorithms to form an image of backscatter energy in the image due to their significant dielectric property contrast with normal breast tissue. Applying our detection system to an MRI-derived numerical breast phantom, we find that the proposed screening scheme and the algorithm are able to detect cancerous growth within the breast effectively and provide accurate location of the suspicious object.

As the first step to construct a real detection system to carry out our scheme for breast cancer microwave detection, we fabricated two small Vivaldi antennas and a real aperture antenna array composed of 8 Vivaldi antennas. The designed antipodal antennas are designed to work in the frequency range of 1 GHz to 10 GHz. Our simulation and measurement results show that this antenna is able to transmit and receive signals in the desired frequency range under the experimental enviroment. Our next work will be focused on the hardware construction of the system, including signal amplification and filtering, circuit connection, etc.

To summarize, the medical microwave imaging research continuing in our laboratory is encouraging. We believe that we are close to a real breast cancer detection system. We also believe that the microwave method will finally be a reliable approach for early-stage breast cancer examination, through the efforts of hundreds of researchers in the microwave imaging community.

BIBLIOGRAPHY

[1] A. Jemal, T. Murray, E. Ward, et al. "Cancer statistics, 2005," *CA Cancer J. Clin.*, Vol. 55, No. 1, pp. 10-30, Jan-Feb 2005.

[2] American Cancer Society, *Breast Cancer Facts Figures 2011-2012*, 2011. Available on www.cancer.org/Research/Cancer FactsFigures/BreastCacerFactsFigures.

[3] "U.S. Breast Cancer Statistics," Available on www.breascancer.org, Oct. 2011.

[4] P. T. Huynh, A. M. Jarolimek, and S. Daye, "The false-negative mammogram," *Radiograph.*, Vol.18, No. 5, pp.1137-1154, 1998.

[5] J.G. Elmore, M. B. Barton, V. M. Moceri, S. Polk, P. J. Arena, and S. W. Fletcher, "Ten-year risk of false positive screening mammagrams and clinical breast examinations," *New Eng. J. Med.*, Vol.338, No.16, pp.1089-1096, 1998.

[6] M. Kriege, Cecile T.M. Brekelmans, C. Boetes, P.E. Besnard, H.M. Zonderland, I.M. Obdeijn, R.A. Manoliu, T. Kok, H. Peterse, Madeleine M.A. Tilanus-Linthorst, S.H. Muller, S. Meijer, J.C. Oosterwijk, Louk V.A.M. Beex, Rob A.E.M. Tollenaar, H.J. de Koning, Emiel J.T. Rutgers, and Jan G.M. Klijn, "Efficacy of MRI and Mammography for Breast-Cancer Screening in Women with a Familial or Genetic Predisposition," *New Eng. J. Med.*, Vol.351, No.5, pp.427-437, 2004.

[7] S.S. Chaudhary, R.K. Mishra, A. Swarup, and J.M. Thomas, "Dielectric properties of normal and malignant human breast tissues at radiowave and microwave frequencies," *Indian J. Biochem. Biiophys.*, Vol. 21, pp. 76-79, 1984.

[8] A.J. Surowiec, S.S. Stuchly, J.R. Barr, and A. Swarup, "Dielectric properties of breast carcinoma and the surrounding tissues," *IEEE Trans. Biomed. Eng.*, Vol. 35, pp. 257-263, Apr. 1988.

[9] W.T. Joies, Y.Z. Dhenxing, and R.L. Jirtle. "The measured electrical properties of normal and malignant human tissues from 50 to 900 MHz," *Med. Phy.*, Vol. 21, pp. 547-550, 1994.

[10] X. Li and S.C. Hagness, "A confocal microwave imaging algorithm for breast cancer detection," *IEEE Microwave Wireless Components Lett*, Vol. 11, pp.130-132, Mar. 2001.

[11] M. Lazebnik, C. Zhu, G.M. Palmer, J. Harter, S. Sewall, N. Ramanujam, and S.C. Hagness, "Tissue specimens obtained from reduction surgeries: comparison of optical and microwave properties," *IEEE Trans. Biomed. Eng.*, Vol. 55, No.10, pp. 2444-2451, Oct. 2008.

[12] K.S. Cole, R.H. Cole, "Dispersion and Absorption in Dielectrics - I Alternating current characteristics," *J. Chem. Phys.*, Vol. 9, pp. 341352, 1941.

[13] K.S. Cole, R.H. Cole, "Dispersion and Absorption in Dielectrics - II Direct current characteristics". *J. Chem. Phys.*, Vol. 10, pp. 98105, 1942.

[14] M. Lazebnik, D. Popovic, L. McCartney, C. B. Watkins, M. J. Lindstrom, J.Harter, S. Sewall, T. Ogilvie, A. Magliocco, T. M. Breslin, W. Temple, D. Mew, J. H. Booske, M. Okoniewski, and S. C. Hagness, "A large-scale study of the ultrawideband microwave dielectric properties of normal, benign and malignant breast tissues obtained from cancer surgeries," *Phys. Med. Biol.*, Vol. 52, pp. 2637-2656, 2007.

[15] M. Lazebnik, E.L. Madsen, G.R. Frank, and S.C. Hagness, "Tissue-mimicking phantom materials for narrowband and ultrawideband microwave applications," *Phys. Med. Biol.*, Vol. 50, pp. 4245-4258, 2005.

[16] D. Byrne, M. O'Halloran, M. Glavin, and E. Jones, "Contrast enhanced beamforming for breast cancer detection," *Pier*, Vol. 28, pp. 219-234, 2011.

[17] A. Mashal, B. Sitharaman, L. Xu, P.K. Avti, A.V. Sahakian, J.H. Booske, S.C. Hagness, "Toward carbon-nanotube-based theranostic agents for microwave detection and treatment of breast cancer: enhanced dielectric and heating response of tissue-mimicking materials," *IEEE. Trans. Biomed. Eng.*, Vol. 57, No. 8, pp. 1831-1834.

[18] J. D. Shea, P. Kosmas, S. C. Hagness, and B. D. Van Veen, "Contrast-enhanced microwave imaging of breast tumors: A computational study using 3D realistic numerical phantoms," *Inverse Problems*, Vol. 26, 074009 (22 pages), 2010.

[19] R.A. Kruger, K.D. Miller, H.E. Reynolds,Jr WL Kiser, D.R. Reinecke, G.A. Kruger, "Contrast enhancement of breast cancer in vivo using thermoacoustic CT at 434 MHz," *Radiology*, Vol. 216, pp. 279-283, 2000.

[20] B. Guo, J. Li, H. Zmuda, M. Sheplak, "Multifrequency microwave-induced thermal acoustic imaging for breast cancer detection," *IEEE Trans. Biomed. Eng.*, Vol. 54, No. 11, Nov. 2007.

[21] Yao Xie, Bin Guo, Jian Li, Geng Ku, L.V. Wang, "Adaptive and Robust Methods of Reconstruction (ARMOR) for Thermoacoustic Tomography," *IEEE Trans. Biomed. Eng.*, Vol. 55, No. 12, pp. 2741-2752.

[22] L. Nie, D. Xing, Q. Zhou, D. Yang, H. Guo, "Microwave-induced thermoacoustic scanning CT for high-contrast and noninvasive breast cancer imaging," *Med. Phy.*, Vo. 35, No. 9, pp. 4026-4032, 2008.

[23] A. Mashal, J.H. Booske, and S.C. Hagness, "Toward contrast-enhanced microwave-induced thermoacoustic imaging of breast cancer: an experimental study of the effects of microbubbles on simple thermoacoustic targets," *Phys. Med. Biol.*, Vol. 54, pp. 641-650, 2009.

[24] X. Wang, H. Xin, D. Bauer, and R. Witte, "Microwave induced thermal acoustic imaging modeling for potential breast cancer detection," *IEEE APSURIS Symposium 2011*, pp. 722-725, 2011.

[25] G.K. Zhu, and M. Popovic, "Comparison of radar and thermoacoustic techniques in microwave breast imaging," *Pier*, Vol. 35, pp. 1-14, 2011.

[26] T. Cui and W. Chew, "Diffraction Tomographic Algorithm for the Detection of Three-Dimensional Objects Buried in a Lossy Half-Space," *IEEE Trans. Ant. Prop.*, vol.50, No. 1, pp. 42-49, Jan. 2002.

[27] M. Born and E. Wolf, *Principles of Optics*, 6th ed. New York: Pergamon Press, 1980.

[28] M. Moghaddam, W. C. Chew, and M. Oristaglio,"Comparison of the Born iterative method and Tarantolas method for an electromagnetic time-domain inverse problem," *Int. J. Imag. Sys. Tech.*, vol. 3, no. 4, pp. 318333, 1991.

[29] W. Chew and Y. Wang, "Reconstruction of two-dimensional permittivity distribution using the distorted Born iterative method," *IEEE Trans. Med. Imaging*, vol. 9, No. 2, pp. 218-225, Jun. 1990.

[30] D. W. Winters, J. D. Shea, P. Kosmas, B. D. Van Veen, and S. C. Hagness, "Three-dimensional microwave breast imaging: Dispersive dielectric properties estimation using patient-specific basis functions," IEEE Trans. Med. Imaging, vol. 28, No. 7, pp. 969-981, July 2009.

[31] H. Zhang, S.Y. Tan, and H.S. Tan, "A novel method for microwave breast cancer detection," *Pier*, Vol. 83, pp. 413-434, 2008.

[32] N. Irishina, M. Moscoso, and O. Dorn, "Microwave tomography for breast cancer detection using level sets," *Proceeding 23rd ACES*, pp. 1955-1960.

[33] D. W. Winters, E. J. Bond, B. D. Van Veen, and S. C. Hagness, "Estimation of the frequency-dependent average dielectric properties of breast tissue using a time-domain inverse scattering technique," *IEEE Trans. Ante. Prop.* Vol. 54, No. 11, pp. 3517-3528, Nov. 2006.

[34] D. W. Winters, B. D. Van Veen, and S. C. Hagness, “A sparsity regularization approach to the electromagnetic inverse scattering problem,” *IEEE Trans. Ante. Prop.*, Vol. 58, No. 1, pp. 145-154, January 2010.

[35] J. D. Shea, P. Kosmas, S. C. Hagness, and B. D. Van Veen, “Three-dimensional microwave imaging of realistic numerical breast phantoms via a multiple-frequency inverse scattering technique,” *Medical Physics*, Vol. 37, No. 8, pp. 4210-4226, August 2010.

[36] E.C. Fear, S.C. Hagness, P. M. Meaney, M. Okoniewski, M.A. Stuchly, “Enhancing Breast tumor detection with near-field imaging,” *IEEE. microwave Mag.*, pp.48-56, Mar. 2002.

[37] E.C. Fear, X. Li, S.C. Hagness, and M.A. Stuchly, “Confocal microwave imaging for breast cancer detection: localization of tumors in three dimensions,” *IEEE Trans. Biomed. Eng.*, Vol. 49, No. 8, pp. 812-822, Aug. 2002.

[38] M. Klemm, I. J. Craddock, J. A. Leendertz, A. Preece, and R. Benjamin, “Improved delay-and-sum beamforming algorithm for breast cancer detection,” *Int. Journal of Ant. and Prop.*, Vol. 2008, Article ID 761402, 9 pages, 2008. doi:10.1155/2008/761402

[39] H. B. Lim, N.T. T. Nhung, E. Li and N.D. Thang, “Confocal Microwave imaging for breast cancer detection: delay-multiply-and-sum image reconstruction algorithm,” *IEEE Trans. Biomed. Eng.*, Vol.55, No. 6, pp. 1697-1704, 2008.

[40] M. Converse, E.J. Bond, S.C. Hagness, B.D. Van Veen, “Ultrawide-band microwave space-time beamforming for hyperthermia treatment of breast cancer: a computational feasibility study,” *IEEE. Trans. Micr. Theo. Tech.*, Vol. 52, No. 8, pp. 1876-1889, 2004,

[41] X. Li, S.K. Davis, S.C. Hagness, D.W. Van der Weide, B.D. Van Veen, “Microwave imaging via space-time beamforming: experimental investigation of tumor detection in multilayer breast phantoms,” *IEEE Trans. Micro. Theo. Tech.*, Vo. 52, No. 8, pp. 1856-1865, 2004.

[42] E. J. Bond, X. Li, S.C. Hagness, B.D. Van Veen, “ Microwave imaging via space-time beamforming for early detection of breast cancer,” *IEEE Trans. Ant. Prop.*, Vol. 51, No. 8, pp. 1690-1705, 2003.

[43] B.Liu, X. Xiao, X. Liu, “Ultra-wideband microwave image reconstruction by robust capon beamforming algorithm for early breast cancer detection,” *Proc. control, automation and system engineering 2011*, pp. 1-4, July, 2011.

[44] P. Kosmas, C. Rappaport, “FDTD-Based time reversal for microwave breast cancer detection - localization in three dimensions,” *IEEE Trans. Microwave theory tech.*, Vol. 54, No. 4, pp. 1921-1927, 2006.

[45] Y. Jin, Y. Jiang, J.M.F. Moura, "Time reversal beamforming for microwave breast cancer detection," *Proc. IEEE Image Processing*, Vol. 5, pp. V13-V16, 2007.

[46] P. Kosmas, C. Rappaport, "A matched-filter FDTD-based time reversal approach for microwave breast cancer detection," *IEEE Trans. Ant. Prop.*, Vol. 54, No.4, pp. 1257-1264.

[47] S. K. Davis, H. Tandradinata, S. C. Hagness, and B. D. Van Veen, "Ultrawideband microwave breast cancer detection: A detection-theoretic approach using the generalized likelihood ratio test," *IEEE Trans. Biomed. Eng.*, Vol. 52, No. 7, pp. 1237-1250, July 2005.

[48] B. Guo, Y. Wang, J. Li, P. Stoica, and R. Wu, "Microwave imaging via adaptive beamforming methods for breast cancer detection," *J. Electromagnetic Waves and Applications*, Vol. 20, No. 1, pp. 53-63, 2006.

[49] Y. Xie, B. Guo, J. Li, and P. Stoica, "Novel Multi-static Adaptive Microwave Imaging Methods for Early Breast Cancer Detection," *EURASIP Journal on Applied Signal Processing*, no. 91961, pp. 1-13, Sep. 2006.

[50] Y. Xie, B. Guo, L. Xu, J. Li, "Multistatic adaptive microwave imaging for early breast cancer detection," *IEEE Trans. Biomed. Eng.*, Vol. 53, No. 8, pp.1647-1657, Aug. 2006.

[51] K. Yee, "Numerical solution of initial boundary value problems involving Maxwell's equations in isotropic media," *IEEE Trans. Ant. Prop.*, Vol.14, No. 3, pp. 302307, 1966.

[52] A. Taflove, "Application of the finite-difference time-domain method to sinusoidal steady state electromagnetic penetration problems," *IEEE Trans. Electromagnetic Compatibility*, Vol. 22, No. 3, pp. 191202, 1980.

[53] S. C. Hagness, A. Taflove, and J. E. Bridges, "Two-dimensional FDTD analysis of a pulsed microwave confocal system for breast cancer detection: Fixed-focus and antenna-array sensors," *IEEE Trans. Biomed. Eng.*, Vol. 45, Vol. 12, pp. 14701479, 1998.

[54] A. Taflove, and S. C. Hagness, *Computational Electrodynamics: The Finite-Difference Time-Domain Method, 3rd ed.*, Artech House Publishers, ISBN 1-58053-832-0, 2005.

[55] Matthew N. O. Sadiku, *Numerical techniques in electromagnetics, 2nd ed.*, CRC Press LLC, 2001.

[56] Mur G, "Absorbing boundary conditions for the finite-difference approximation of the time-domain electromagnetic field equations," *IEEE Trans. Electromagn. Compat.*, Vol. 23, No. 4, pp. 377-382, Nov. 1981.

[57] P. Liao, H. L. Wong, B. P. Yang, and Y. F. Yuan, “A transmitting boundary for transient wave analysis,” *Scientia Sinica*, Vol. 27, No. 10, pp. 1065, October 1984.

[58] M. Moghaddam, W. C. Chew, “Stabilizing Liao’s absorbing boundary conditions using single-precision arithmetic,” *Proceeding of APS1991*, Vol.1, pp. 430-433, 1991.

[59] J.C. Olivier, “On the synthesis of exact free space absorbing boundary conditions for the finite-difference time-domain method,” *IEEE Trans. Ant. Prog.*, Vol. 40, No. 4, pp. 456460, April 1992.

[60] J.P. Berenger, “A perfectly matched layer for the absorption of electromagnetic waves,” *Jour. Comp. Phys.*, Vol. 114, pp. 185200, Aug. 1994.

[61] J.P. Berenger, “Perfectly matched layer for the FDTD solution of wavestructure interaction problems,” *IEEE Trans. Ant. Prop.*, Vol. 44, No. 1, pp. 110117, Jan. 1996.

[62] Z. S. Sacks, D. M. Kingsland, D. M. Lee, J. F. Lee, “A perfectly matched anisotropic absorber for use as an absorbing boundary condition,” *IEEE Trans. Antennas Propagat.*, Vol. 43, No. 12, pp. 1460-1463, Dec. 1995.

[63] S. D. Gedney, “An anisotropic perfectly matched layer absorbing media for the trunction of FDTD lattices,” *IEEE Trans. Antennas Prop.*, Vol. 44, No. 12, pp. 1630-1639, Dec. 1996.

[64] S. D. Gedney, “An anisotropic PML absorbing media for the FDTD simulation for fields in lossy and dispersive media,” *Electromagnetics*, Vol. 16, No. 4, pp. 399-415, 1996.

[65] I. W. Sudiarta, “An absorbing boundary condition for FDTD trunction using multiple absorbing surfaces,” *IEEE Trans. Antennas Propagat.*, Vol. 51, No. 2, pp. 3268-3275, Dec. 2003.

[66] T. S. Yeo, P. S. Kooi, M. S. Leong, and R. H. Feng, “A performance assessment of Liaos absorbing boundary conditions for FDTD method,” *Microwave Optics tech. lett.*, Vol. 16, No. 3, pp. 186-197, Oct. 20, 1997.

[67] M.N.O. Sadiku, V. Bemmel, and S. Agbo, “Stability criteria for finitedifference time-domain algorithm,” *Proc. IEEE Southeastcon*, pp. 4850, April 1990.

[68] Daniel Flores-Tapia, G. Thomas and S. Pistorius, “Skin surface removal on breast microwave imagery usng wavelet multiscale products,” *Proceedings of the 5th medical imaging: physiology, function and structure from medical images*, 2006.

[69] University of Texas MD Anderson Cancer Center, “Breast Cancer Screening: Increased Risk”, available on http://www.mdanderson.org.

[70] B. Zhou, W. Shao, and G. Wang, "UWB microwave imaging for early breast cancer detection: Effect of the coupling medium on resolution," *Proc. Radio Sci. Conf.*, pp. 431434, 2004.

[71] J. M. Sill and E. C. Fear, "Tissue sensing adaptive radar for breast cancer detection: Study of immersion liquid," *Electron. Lett.*, Vol. 41, No. 3, pp. 113115, 2005.

[72] W. Shao, R. S. Adams. "UWB imaging with multi-polarized signals for early breast," *Proc. IEEE AP-S International Symposium 2010*, pp. 1-4, July 2010.

[73] G. Brooker, "Sensors and signals," Chapter 6, pp. 305, 2007.

[74] W. Shao, B. Zhou, G. Wang, "Early breast tumor imaging via UWB microwave method: study on multi-target detection," *Proc. IEEE AP-S International Symposium 2005*, Vol. 3A, pp. 835-838, 2005.

[75] G. Wang, X. Zeng, "Impact of dispersion in breast tissue on high-resolution microwave imaging for early breast tumor detection," *Proc. IEEE AP-S International Symposium 2004*, vol. 3, pp. 2452-2455, June 2004.

[76] W. Shao, R.S. Adams, "UWB microwave imaging for early breast cancer detection: A novel confocal imaging algorithm," *Proc. IEEE AP-S International Symposium 2011*, pp. 707-709, July 2011.

[77] W. Shao, R.S. Adams, "Multi-polarized microwave power imaging algorithm for early breast cancer detection," *Pier M*, Vol. 23, pp. 93-107, 2012.

[78] The UWCEM Numerical Breast Phantoms Repository. Available at http://uwcem.ece.wisc.edu/MRIdatabase/.

[79] X. Li, S.C. Hagness, M.K. Choi and D.W. van der Weide, "Numerical and experimental investigation of an ultrawideband ridged pyramidal horn antenna with curved launching plane for pulse radiation," *IEEE Ante. Wireless Propag. Lett.*, Vol. 2 , pp. 259-262,2003.

[80] P.J. Gibson, "The vivaldi aerial," *Proc. 9th Europe microwave conference*, pp. 101-105, 1979.

[81] A. Hood, T. Karacolak, E. Topsakal, "A small antipodal Vivaldi antenna for ultrawide-band applications," *IEEE Ante. Wireless Prop. Lett.*, Vol. 7, pp. 656-660, 2008.

[82] P. Fei, Y. Jiao, W. Hu, F. Zhang, "A miniaturized antipodal Vivaldi antenna with improved radiation characteristics," *IEEE Ante. Wireless Prop. Lett.*, Vol. 10, pp. 127-130, 2011.

[83] J. Bai, S. Shi, D.W. Prather, “Modified compact antipodal vivaldi antenna for 450-GHz UWB application,” *IEEE Trans. Micr. Theo. Tech*, Vol. 59, No. 4, pp. 1051-1057, 2011.

[84] Y. Che; K. Li; X. Hou; W. Tian, “Simulation of a small sized antipodal Vivaldi antenna for UWB applications,” *Proc. ICUWB 2010*, Vol. 1, pp. 1-3, 2010.

[85] S. Wang, X.D. Chen; C.G. Parini, “Analysis of ultra wideband antipodal vivaldi antenna design,” *Proc. Ante. Prop. 2007*, pp. 129-132, 2007.

[86] S. Chamaani, S.A. Mirtaheri, M.S. Abrishamian, “Improvement of time and frequency domain performance of antipodal vivaldi antenna using multi-objective particle swarm optimization,” *IEEE Trans. Ante. Prop.*, Vol. 59, No. 5, pp. 1738-1742, 2011.

[87] M. Chiappe, G.L. Gragnani, “Vivaldi antennas as detectors for microwave imaging: some theoretical results and design considerations,” *Proc. Imaging Syst. Tech 2004*, pp. 22-27, 2004.

[88] M. Chiappe, G.L. Gragnani, “Vivaldi antennas as detectors for microwave imaging: further steps in its radiation features analysis,” *Proc. Imaging Syst. Tech 2005*, pp. 8-13, 2005.

[89] M. Chiappe, G.L. Gragnani, “Vivaldi antennas for microwave imaging: theoretical analysis and design considerations,” *IEEE Trans. Inst. Meas.*, Vol. 55, No. 6, pp. 1885-1891, 2006.

[90] X. Zhuge, A. Yarovoy, “Design of low profile antipodal Vivaldi antenna for ultra-wideband near-field imaging,” *Proc. Ante. Prop. 4th European Conference*, pp. 1-5, 2010.

[91] X. Zhuge, A. Yarovoy , L.P. Ligthart, “Circularly tapered antipodal Vivaldi antenna for array-based ultra-wideband near-field imaging,” *Proc. 6th European Radar Conference*, pp. 250-253, 2009.

[92] S.M. Salvador and G. Vecchi, “Experimental tests of microwave breast cancer detection on phantoms,” *IEEE Trans Ante. Prop.*, Vol. 57, No. 6, pp. 1705-1712, 2009.

[93] Y. Wang, M.R. Mahfouz, “Novel compact tapered microstrip slot antenna for microwave breast imaging,” *Proc. IEEE AP-S International Symposium 2011*, pp. 2119-2122, 2011.

[94] J. Bourqui, M.Okoniewski, E.C. Fear, “Balanced antipodal vivaldi antenna with dielectric director for near-field microwave imaging,” *IEEE Trans Ante. Prop.*, Vol. 58, No. 7, 2010.

[95] W. Shao, R. S. Adams, "A microstrip antenna array using Vivaldi antennas for early breast cancer imaging," *IEEE Antennas Wireless Propag. Lett.*, to be submitted.

APPENDIX A: INTRODUCTION TO COLE-COLE EQUATION

The Cole−Cole equation is a relaxation model that is often used to describe dielectric relaxation in polymers [12] [13]. It is given by the equation

$$\epsilon^*(\omega) - \epsilon_\infty = \frac{\epsilon_s - \epsilon_\infty}{1 + (\imath\omega\tau)^{1-\alpha}} \tag{A.1}$$

where ϵ^* is the complex dielectric constant, ϵ_s and ϵ_∞ are the "static" and "infinite frequency" dielectric constants, ω is the angular frequency and τ is a time constant. The exponent parameter α, which takes a value between 0 and 1, allows description of different spectral shapes. When $\alpha = 0$, the Cole−Cole model reduces to the Debye model. When $\alpha > 0$, the relaxation is stretched, i.e. it extends over a wider range on a logarithmic ω scale than Debye relaxation.